Opto-Electro-Thermal VCSEL Device Simulation

Diss. ETH No. 15464

Opto-Electro-Thermal VCSEL Device Simulation

A dissertation submitted to the

SWISS FEDERAL INSTITUTE OF TECHNOLOGY ZURICH

for the degree of

Doctor of Technical Sciences

presented by

MATTHIAS STREIFF

Dipl. El.-Ing. ETH, MSc Imperial College London
born 19 December 1971
citizen of Diesbach and Luchsingen, Glarus
and London, United Kingdom

accepted on the recommendation of

Prof. Dr. Wolfgang Fichtner, examiner
Prof. Dr. Werner Bächtold, co-examiner

2004

Contents

Acknowledgements

I would like to thank Prof. W. Fichtner for giving me the opportunity to perform this work at his institute, his encouragement and support during my years at IIS. Moreover, many of the contacts to industry which proved to be an essential ingredient for the success of this work were enabled by him. I also wish to thank Prof. W. Bächtold for accepting to be the co-examiner of this thesis and for carefully reviewing the manuscript.

B. Witzigmann and A. Witzig started the optoelectronics activities at IIS. I wish to thank them for offering me the opportunity to become acquainted with optoelectronics modeling and simulation which was an entirely new field for me at the time.

Essential input to this work has been provided by Prof. P. Arbenz and O. Chinellato (Institute of Computational Science, ETH) with regards to eigensolvers and finite elements, and B. Schmithuesen regarding small signal analysis. I am grateful to D. Aemmer for coordinating the administrative side of the research project.

M. Pfeiffer and the amazing S. Kubrick deserve special thanks for their help and patience during endless late night code freeze sessions. Further thanks to the growing opto-family at IIS, L. Schneider, B. Jacob, V. Laino, M. Luisier, S. Odermatt, and F. Geelhaar for all their contributions. Furthermore, I am thankful to S. Roellin and O. Schenk for their help regarding linear solvers, and to M. Schild for proofreading the manuscript.

This work has had close links to activities in industry. I would like to thank W.-C. Ng, P. Regli, A. Wettstein, and O. Penzin of ISE Integrated Systems Engineering AG, P. Royo, S. Eitel, and M. Moser of Avalon Photonics AG for their continuing support and interest.

During my work at IIS I had the opportunity to advise several students performing undergraduate research in our group. I wish to thank T. Eberle, P. Lässer, A. Bregy, S. Müller, and S. Scheerlinck for their efforts and enthusiasm.

Abstract

A physics-based software for the self-consistent electro-thermo-optical simulation of vertical-cavity surface-emitting laser (VCSEL) devices is presented. The simulator model is based on semiclassical microscopic laser theory. The model self-consistently describes spatially resolved quantities, namely, electrical potential, electron and hole densities, local temperature, and mean optical intensity. The input parameters to the model equations are the topology and the local physical material parameters. Static, small signal modulation, and transient device characteristics can be computed. The model is suitable for the analysis of a wide range of VCSEL types with realistic device structures.

The semiclassical laser model employs the slowly varying amplitude approximation: the optical field is decomposed into a given number of modes at discrete frequencies, and the temporal evolution of the mean electromagnetic energy in each mode is described by a separate photon rate equation. The optical modes are determined by solving Maxwell's vectorial wave equation, subject to an open boundary, taking into account diffraction of electromagnetic waves. Perfectly matched layer absorbing boundaries are used to model the open microcavity. Bulk electro-thermal carrier transport is modeled by a thermodynamic model that accounts for self-heating. At abrupt heterointerfaces a thermionic emission model is used. Electro-thermal transport in the distributed Bragg resonators is rendered by transport through a homogeneous region with an effective conductivity for heat, electrons and holes, and an effective heat capacity. Quantum wells are treated as scattering centres where ballistic transport applies for electrons and holes.

The VCSEL simulator is based on the DESSIS device simulator.

The LUMI mode solver library was developed as an extension in order to handle the optical problem. The Finite Element Method is employed to formulate the physical equations: Box Method for the electro-thermal problem, and combined edge / node finite elements of different polynomial order for the optical problem. Expansions are in cylindrical coordinates assuming rotational symmetry of the device structure. The non-linear electro-thermal matrix equations augmented with a photon rate equation per optical mode are solved by Newton's Method. Solutions to the inhomogeneous form of Maxwell's wave equation are computed using a direct linear solver. The eigenpairs of the homogeneous form are obtained by the Jacobi-Davidson QZ algorithm with a suitable preconditioner. The electro-thermal together with the photon rate equations are coupled to Maxwell's wave equation employing a Gummel type iteration scheme.

The efficient computation of the optical modes based on a continuation scheme allows, for the first time, that Maxwell's vectorial wave equation – for VCSELs with realistic structures and optical sizes – subject to an open boundary, can be solved self-consistently with the electro-thermal device equations.

Simulation results are compared to measurements and show excellent agreement. In order to demonstrate the practical use of the simulator as a computer aided design tool a tutorial is given.

Zusammenfassung

Diese Arbeit beschäftigt sich mit der Entwicklung eines selbstkonsistenten elektro-thermo-optischen Simulators für Vertikalresonator-Laserdioden (VCSEL). Das Simulationsmodell basiert auf einer mikroskopischen, semiklassischen Lasertheorie. Es beschreibt das elektrische Potential, Elektronen- und Löcherdichten, lokale Temperatur und die mittlere optische Intensität räumlich aufgelöst und auf selbstkonsistente Weise. Die Eingabeparameter für die Modellgleichungen umfassen die Topologie und die lokalen physikalischen Materialparameter des Bauelements. Statische Charakteristiken, Kleinsignal- und Grossignalantworten können berechnet werden. Das Modell eignet sich für die Analyse eines breiten Spektrums von VCSEL Typen.

Im verwendeten semiklassischen Lasermodell wird das schnell variierende Lichtfeld lokal durch die sich langsam ändernden Amplitude der optischen Intensität angenähert. Des weiteren wird das optische Feld in eine Anzahl Moden mit diskreten Frequenzen zerlegt. Die zeitliche Änderung der mittleren elektromagnetischen Energie in jeder Mode wird dann mit einer separaten Ratengleichung beschrieben. Die optischen Moden werden durch Lösen der vektoriellen Maxwell Wellengleichung mit abstrahlender Randbedingung bestimmt. Elektrothermischer Ladungsträgertransport wird durch ein thermodynamisches Modell berücksichtigt, welches Selbsterwärmung des Bauteils einbezieht. An abrupten Heteroübergängen wird ein thermionisches Emissionsmodell eingesetzt. Die verteilten Braggresonatoren werden für den elektrothermischen Transport durch eine homogene Region mit effektiver Leitfähigkeit für Wärme, Elektronen, Löcher und einer effektiven Wärmekapazität angenähert. Quantentöpfe werden als Streuzentren mit ballistischem Ladungsträgertransport behandelt.

Das VCSEL Simulationsprogramm basiert auf dem DESSIS Bauelementesimulator. Die LUMI Bibliothek wurde als Erweiterung für die Behandlung des optischen Problems erstellt. Das physikalische Problem wird mittels der Finiten Elemente Methode formuliert. Für das elektrothermische Problem wird die Box Methode verwendet. Eine kombinierte Kanten / Knoten Finite Elemente-Expansion mit verschiedenen Polynomgraden findet Anwendung für das optische Problem. Beide Probleme werden in Zylinderkoordinaten formuliert und gehen davon aus, dass die Anordnung rotationssymmetrisch ist. Die nichtlinearen Matrizengleichungen werden mittels der Newtonmethode gelöst. Die inhomogene Form der Maxwell Wellengleichung wird mit einem direkten Verfahren gelöst. Die Eigenpaare der homogenen Form werden mit dem Jacobi-Davidson QZ Algorithmus mit einem geeigneten Vorkonditionierer bestimmt. Die elektrothermischen Gleichungen, zusammen mit den Photonenratengleichungen, werden mittels einer Gummel-Iterationsprozedur an die Maxwell Wellengleichung gekoppelt.

Dank der effizienten Berechnung der optischen Moden, basierend auf einem Reiterationsverfahren, ist es zum ersten Mal möglich die vektorielle Maxwell Wellengleichung, für realistische VCSEL Strukturen, selbstkonsistent mit den elektrothermischen Gleichungen zu lösen.

Simulationsresultate werden mit Messungen verglichen und zeigen ausgezeichnete Übereinstimmung. Der praktischen Nutzen des Simulators wird mittels eines Tutorials demonstriert.

Chapter 1

Introduction

Semiconductor laser diodes with a vertical optical resonator structure were first proposed by Soda and Iga in 1979 [1]. The devices were termed vertical-cavity surface-emitting lasers (VCSEL) due to the novel concept of light emission perpendicular to the substrate surface as opposed to in-plane emission by traditional edge emitting lasers. The InGaAsP/InP material system was used for the original device.

In 1988 Iga [2] and 1989, 1991 Jewell [3, 4] presented the first room temperature continuous wave results for an electrically pumped device. In [4] 980 nm emission was demonstrated employing the AlGaAs/GaAs system with an active region composed of InGaAs quantum wells. VCSELs in the wavelength range 750–1050 nm manufactured in the AlGaAs/GaAs material system with GaAs and InGaAs active regions became available on a commercial scale in 1999[1].

VCSEL devices have attractive features:

- threshold current < 1 mA [5]
- wall plug efficiency $> 50\%$ [6]

[1] In 2002 around 9 million 850 nm, mostly 1.25–2.5 Gbit/s devices were shipped in the datacom market. Source: *Honeywell sees growth in VCSELs*, 18 August 2003, http://www.fibers.org, IOP Publishing Ltd.

- small signal modulation response > 20 GHz [7]
- radially symmetric optical far field (easy coupling to fibre)
- batch fabrication in two-dimensional arrays (low cost)
- on-wafer test prior to chipping and packaging
- suitable for high density planar integration in hybrid modules and photonic integrated circuits (small device size ≈ 10 μm diameter).

Recent advances have finally led to reliable VCSEL operation at the important telecommunication wavelengths 1300 nm and 1550 nm using the InGaAlAs/InP, InGaAsP/InP and InGaNAsSb/GaAs [8, 9, 10, 11].

1.1 Why Use CAD Software?

Traditionally, new designs of VCSEL device structures and changes to existing designs have been investigated purely experimentally: fabricating test series with parameter variations, characterising the devices and changing the design according to the results as shown in Fig. 1.1a.

Using a technology computer aided design (TCAD) software – as the one presented in this work – the same can potentially be achieved with a significantly reduced experimental effort, with drastically reduced turn-around times, and hence at lower cost (Fig. 1.1b). Prior to the fabrication of a prototype the new device design is analysed and optimised using a simulator. Eventually, a test device is fabricated and characterised. The measured results are then used to correct the parameters of the model and the design procedure is restarted from the top. In addition, special test structures are used to determine specific model parameters. In this way the accuracy of predicting device behaviour is continuously improved, and the number of prototype fabrication cycles lowered.

A reliable device model in the form of a simulator software together with an accurate set of parameters are preliminaries for fabless design and production shown in Fig. 1.2. This approach has recently gained interest among small photonics enterprises. The approach is

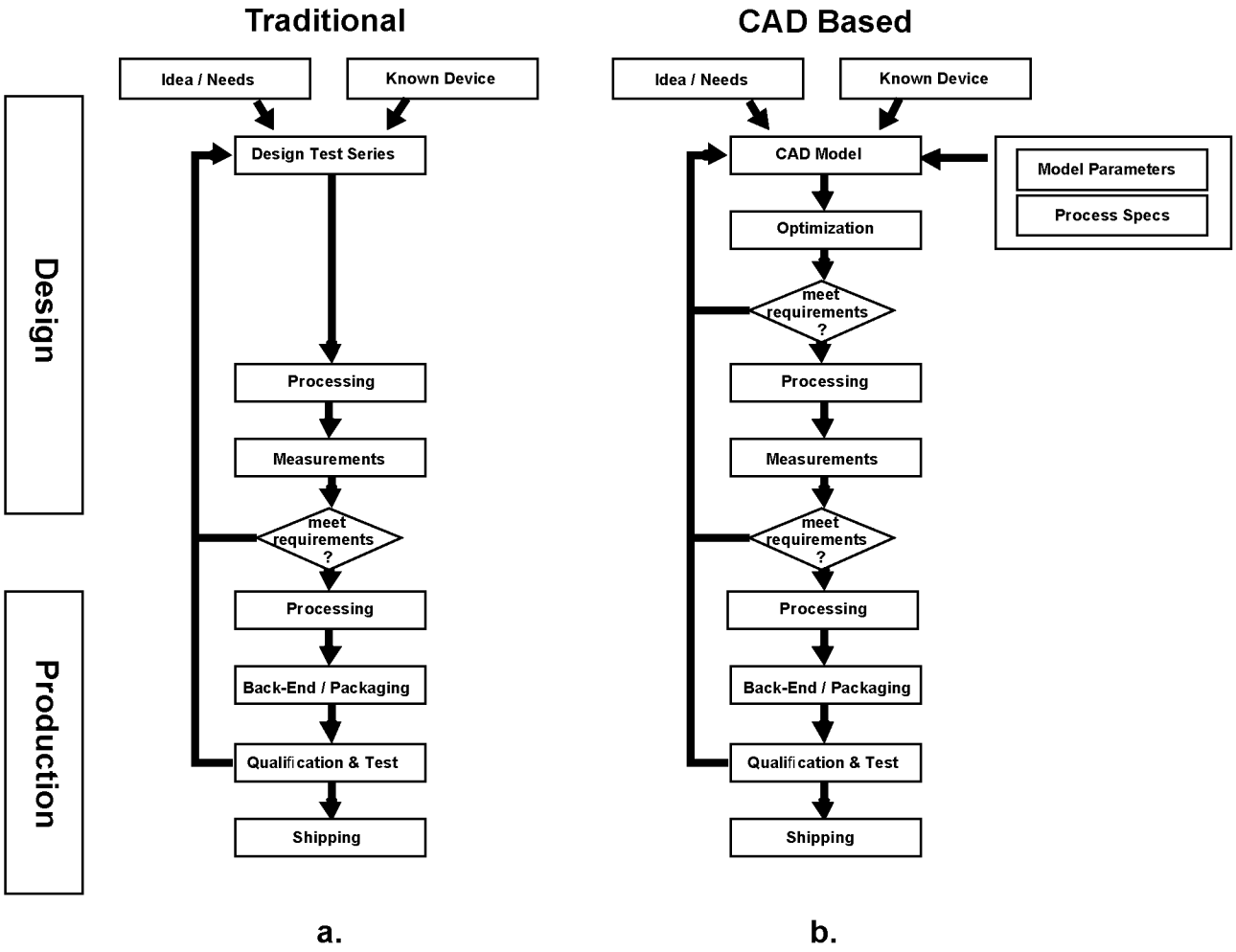

Figure 1.1: Schematic comparing the traditional (a) and TCAD based (b) photonics design concept.

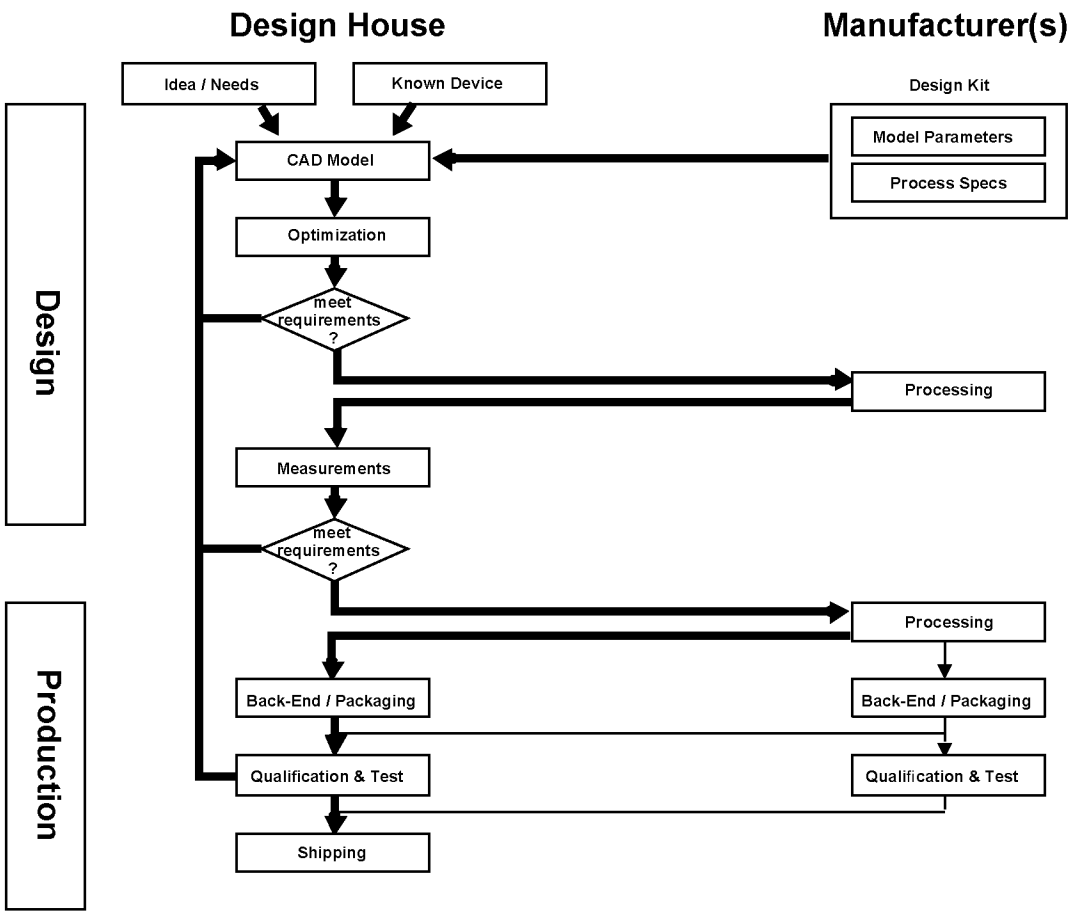

Figure 1.2: Schematic illustrating the fabless design and production approach.

promising for the manufacture of products with larger profit margins for comparatively small and/or specialised markets, as for instance the sensing market. Small design houses with in-depth expertise in a certain application area can have photonic components manufactured at low cost to their specifications at a large foundry. In this way, they can gain access to high-end fabrication processes that they could never afford and maintain in-house due to the prohibitive investments required.

1.2 Applications and Device Types

Present generation VCSEL devices are predominantly aimed at applications as inexpensive high performance light sources in wavelength division multiplexed optical fibre networks for data- and telecommunications. Devices for optical backplanes and short distance datacommunications ($<$ 300 m) are primarily at 850 nm. More recently 1300 nm and 1550 nm VCSELs destined at metropolitan network access and local area networks have become available. Furthermore, VCSELs have gained the attention of manufacturers of optical storage and signal processing equipment, displays, sensors and laser printers.

The basic structure of a VCSEL device is shown in Fig. 1.3. It consists of an electrically driven pin diode with an active region at the centre composed of one or more quantum wells[2]. Highly reflective diffractive mirrors confine the light perpendicular to the substrate and are embedded in the p and n regions. The mirrors, so called distributed Bragg reflectors (DBR), consist of quarter wavelength ($\lambda/4$) layers with alternating refractive indices created by epitaxial growth techniques.

VCSEL devices can be classified according to the wavelength that they operate at and the method used to introduce lateral electrical current and optical mode confinement. The former is dictated by the material used for the active region as was already pointed out at the beginning of Ch. 1. Control over the latter is one of the core issues in VCSEL design. Only the advent of the popular oxide confinement [12] has enabled VCSEL devices with truly low threshold currents ($<$ 1mA). An $Al_xGa_{1-x}As$ layer, with a high Al content, placed in a certain location on the vertical axis within the DBR is oxidized to a desired lateral depth. This forms an electrically insulating current aperture as well as a low refractive index optical confinement. The depth of the oxide aperture is well defined because the rate at which the $Al_xGa_{1-x}As$ is oxidized to Al_2O_3 is accurately controlled by the oxidation time and the Al content of the layer. Lateral confinement may be introduced by

- oxide aperture

[2]There are also optically pumped VCSEL diodes which will not be discussed in this work.

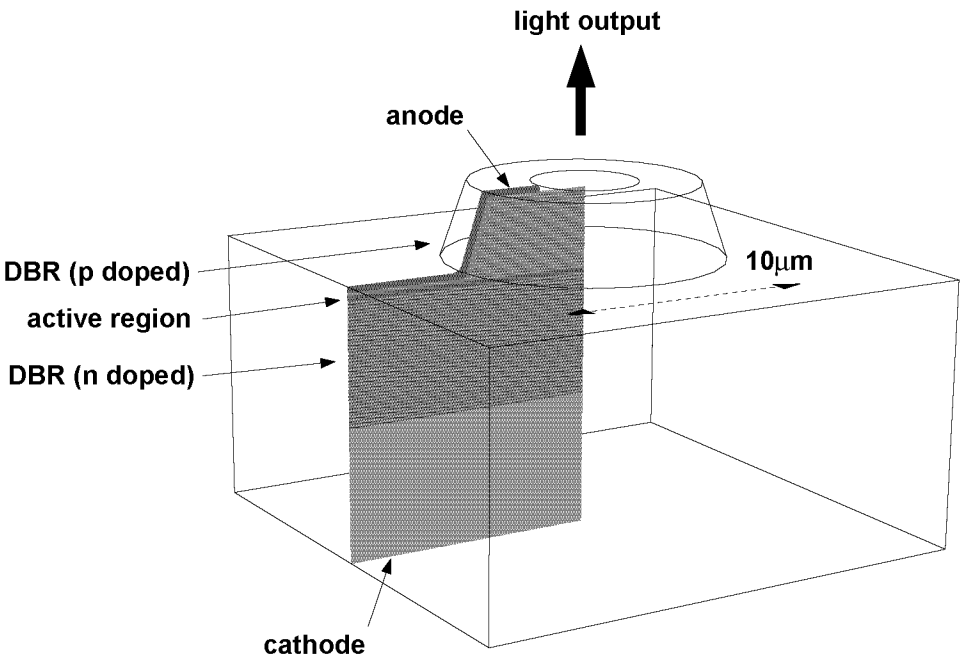

Figure 1.3: Basic VCSEL structure.

- proton irradiation
- etched mesa
- buried heterostructure
- buried tunnel junction.

Heat management is another core issue in VCSEL design. VCSELs are small in size and the layered DBR structures have inferior heat conductivity, especially the ones in the InGaAlAs/InP and InGaAsP/InP material systems. Additionally, for cost saving reasons, VCSELs have to operate uncooled over a large ambient temperature range, typically from 0 ... 80 °C. Hence, the optical gain spectrum and the cavity resonance shift at different material dependent rates over operating conditions. Moreover, at high temperatures optical gain can degrade due to temperature activated carrier leakage and non-radiative recombination. Additionally, the optical field distribution in the cavity changes because of the temperature induced variation of the refractive index. This effect is known as thermal lensing.

In conclusion, self-heating must be taken into account in a practical VCSEL simulation.

As an illustration, cross-sections of three different VCSEL structures are shown in Fig. 1.4. Figure 1.4a shows an etched mesa VCSEL. It is predominantly used for short distance communication at 850 nm in the AlGaAs/GaAs material system.

Figure 1.4b is a buried tunnel junction (BTJ) VCSEL with a bottom (anode side) DBR made of only a few periods of high index contrast insulating dielectric material. This VCSEL type is a promising candidate for communication at 1300 nm and 1550 nm using the InGaAlAs/InP material system. It is well known that this system has a lower maximum refractive index contrast and a lower thermal conductivity compared to the AlGaAs/GaAs system. This leads to a conflict in the requirements for low electrical resistance to minimise self-heating and high reflectivity which is particularly severe for the p-type DBR. The BTJ VCSEL overcomes this problem by employing the mentioned anode side dielectric DBR and an integrated metal heat sink. Furthermore, a buried tunnel junction establishes lateral current and optical mode confinement [8, 10].

Figure 1.4c is also targeted at 1300 nm and 1550 nm wavelengths. The anode side DBR is a metamorphic structure grown in the AlGaAs/GaAs system that provides higher maximum refractive index contrast than the InGaAsP/InP system. Additionally, a sacrificial layer between the cavity, that contains the active zone grown in the InGaAsP/InP system, and the metamorphic mirror has been etched away to make the latter a free structure suspended by the adjacent arms only. With this construction the metamorphic mirror can be electrostatically actuated and hence the resonant wavelength of the VCSEL cavity tuned to a desired point within a certain range. An oxide aperture for lateral current and optical mode confinement is introduced on the anode side just above the cavity [8, 13].

1.3 Scope of Work

Simple rate equation models are commonly used by device designers to obtain a qualitative insight into the operation of a device and can be made to reproduce measured results by a parameter fitting procedure

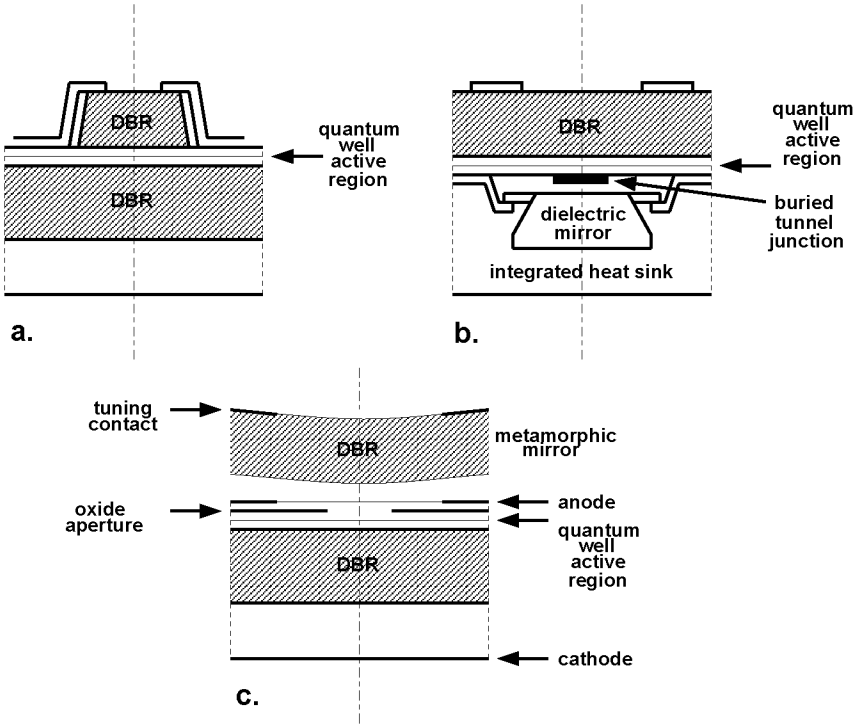

Figure 1.4: Schematic cross-sections of different rotationally symmetric VCSEL structures, (a) etched mesa VCSEL, (b) buried tunnel junction (BTJ) VCSEL, (c) micromechanical, electrostatically actuated tunable VCSEL

[14, 15]. A carrier rate equation describes the time evolution for the charge carriers (electrons and holes in the active region which are assumed equal in number) in a first reservoir

$$\frac{dN}{dt} = \frac{\eta_i I}{e} - R_{sp} - R_{nr} - G\,S \tag{1.1}$$

and a photon rate equation for the photons in a second reservoir

$$\frac{dS}{dt} = \beta_{sp} R_{sp} + \left(G - \frac{1}{\tau_{ph}}\right) S. \tag{1.2}$$

The variable N is the number of carriers, S the number of photons, and G the modal optical gain[3] due to stimulated emission. The optical gain can be modeled empirically with the three parameter formula

$$G(N,S) = G_0 \log \frac{N + N_s}{N_{tr} + N_s}. \tag{1.3}$$

The parameters are

- internal quantum efficiency η_i [1]
- spontaneous radiative emission rate R_{sp} $\left[\mathrm{s}^{-1}\right]$
- non-radiative emission rate R_{nr} $\left[\mathrm{s}^{-1}\right]$
- spontaneous emission coupling factor β_{sp} [1]
- optical gain coefficient G_0 $\left[\mathrm{s}^{-1}\right]$
- transparency carrier number N_{tr} [1] (at which G becomes positive)
- cavity photon life time τ_{ph} $\left[\mathrm{s}^{-1}\right]$.

Moreover, e is the elementary charge, and N_s a shift to force the natural logarithm to be finite at $N = 0$. The optical output power is given by

$$P_{out} = \frac{1}{\tau_m} S \hbar \omega \tag{1.4}$$

[3]The optical mode confinement factor is included in G.

with the photon energy $\hbar\omega$ and the energy loss rate $1/\tau_m$ through the VCSEL aperture.

In contrast to the zero-dimensional rate equation model given in Eqs. (1.1–1.4) the aim of this work is to devise a VCSEL model that is based on a microscopic theory. That is, the model shall self-consistently describe spatially resolved quantities, namely, electrical potential, electron and hole densities, local temperature, and mean optical intensity. The input parameters to the model equations are the *topology* of the device and the *local physical material parameters* as opposed to the *effective parameters* of the rate equation model. The spatially resolved quantities already provide the designer with valuable insights into device operation. Additionally, they can be used to compute electrical, thermal and optical terminal quantities. These can then be compared to results obtained from measurements.

The spatially resolved quantities are computed by a finite element approach. In practice, its limitation lies in the maximum size of the discretised problem that can be accommodated on a given computer, and the maximum permissible time to numerically solve the associated system of matrix equations. It will be shown in Ch. 4 that it is feasible to use finite elements to handle design tasks involving realistic VCSEL device structures. VCSEL devices may have arbitrary rotationally symmetric geometries such as the ones shown in Fig. 1.4. Examples in Ch. 4 are restricted to 840 nm and 980 nm devices using AlGaAs/GaAs with GaAs and InGaAs quantum wells. However, the approach is applicable to all common VCSEL material systems mentioned at the beginning of Ch. 1.

The laser model follows a semiclassical approach. The optical field is described by Maxwell's equations with a polarisation term. This term is due to the interaction between light and charge carriers and is determined by quantum mechanics.

In order to appreciate the modeling approach taken in this work an overview of important time constants of the physical processes involved is given. The figures give the correct order of magnitude for a VCSEL device with emission wavelength at $\lambda = 1$ μm.

1. Electron and hole mobilities are governed by the effective carrier mass, impurity and phonon scattering with a total rate of 10 ps^{-1} [16]. This determines how quickly the carrier density in

the intrinsic region of the pin diode can be modulated by alternatingly supplying and removing carriers by drift and diffusion.

2. Quantum well carrier capture and escape rates are 0.1–1.0 ps^{-1} [17, 18] given by carrier phonon scattering.

3. Relaxation of non-equilibrium carrier distributions is by carrier carrier scattering at a rate of 10 ps^{-1} [18, 19].

4. Recombination rate due to spontaneous emission, Auger, Shockley-Read-Hall (SRH, defect assisted) $\approx 1.0\ ns^{-1}$ (GaAs, strongly dependent on processing).

5. Recombination rate due to stimulated emission is proportional to $G\,S$ and can thus be controlled by modal gain G and optical intensity S.

6. Polarisation decay time is 100 fs [18, 19, 20].

7. Period of optical field is 3.3 fs.

8. Cavity round trip time for optical field is 100 fs (assume cavity diameter $\approx 10\ \mu$m).

9. Decay time of optical energy stored in cavity is 10 ps.

The model assumes that carriers remain in thermal equilibrium with the lattice. Hence, carrier transport is modeled by a thermodynamic (energy balance) model that takes into account self-heating of the device. At heterojunctions and quantum wells the model is enhanced by a thermionic emission model and a carrier capture and escape model, respectively.

The former assumption breaks down at high modulation frequencies when phonon scattering is becoming too slow to establish thermal equilibrium between carriers and lattice. This is particularly severe for quantum well capture and escape scattering (2). The relaxation mechanism (3) is normally still fast enough to maintain a Fermi distribution for electrons and holes at an elevated oscillating plasma temperature in the quantum well. Moreover, due to the slow phonon scattering the electron and hole density in the quantum well start to lag behind and oscillate out of phase with the bulk carrier density. This leads to

a carrier bottleneck at the bulk quantum well interface and hence to additional damping of the modulation response [18].

The model assumes that carrier carrier scattering (3) always establishes Fermi distributed carrier populations. This breaks down at very high optical intensities when stimulated recombination rate is high and carrier carrier scattering becomes too slow to maintain the Fermi distribution of the electrons and holes in the quantum well. This effect leads to spectral hole burning and applies to both continuous wave and modulated operation. In general, optical intensities in VCSELs are not sufficiently high to burn spectral holes in the active medium [18].

Items (4) and (5) state the reason why the modulation bandwidth of a laser diode exceeds by far the one of a light emitting diode. The resonance frequency of the modulation transfer function is approximately proportional to the modal differential gain a_N and the optical intensity S. A laser diode is therefore a *gain controlled* device whose bandwidth is intrinsically only limited by the optical gain available. However, in practice the bandwidth will be limited by gain saturation and the maximum rate at which carriers can be supplied and removed from the quantum well. In a light emitting diode the maximum bandwidth is limited by the relatively slow recombination process (spontaneous emission, Auger, SRH) to < 1 GHz. This can be improved by a resonant optical cavity that enhances the spontaneous emission process (Sec. 4.1.2).

In practical devices the modulation response is additionally limited by external wiring. This is represented by a compact model composed of resistances, capacitances and inductances external to the device model.

Two distinct groups of time constants can be identified in items (1–9): one of the order of femtoseconds and the other of picoseconds separated by approximately 2 orders of magnitude. Simulation on the fast femtosecond timescale is computationally prohibitive, especially for the spatially resolved complex structures shown in Fig. 1.4, and unsuitable to compute static (DC) and stationary (AC) characteristics of the VCSEL device that are important in practice. Instead a frequency domain approach changing in time on the slow picosecond

scale is employed[4].

Consider continuous wave operation first. At each point in the optical cavity the optical field on the fast timescale is Fourier transformed from the time domain to the frequency domain. It is then assumed that the wanted part of the optical field can be represented by a discrete spectrum. That is, in each point of the optical cavity a discrete complex valued spectrum is assumed over the same small set of frequencies. According to items (6) and (7) the period of the fast time domain optical field is short with respect to polarisation decay. If polarisation is equal to a term constant with the electric field plus a linear term, and polarisation dynamics is neglected, the effect of the polarisation can be represented by a constant optical gain term and a constant source term in the frequency domain representation. This approach works particularly well for VCSEL devices since they have a discrete optical spectrum with only a small number of frequencies corresponding to the optical modes.

If the VCSEL is modulated on the slower pico- to nanosecond timescale, the optical gain term, source term, and hence the complex amplitudes of the spectra also change on the slow time scale. It is then assumed that the optical field only depends on the instantaneous value of the gain term and source term.

By restricting the frequency domain representation to a discrete spectrum, linearising the polarisation in the electric field, and neglecting polarisation dynamics, the model can no longer reproduce certain effects. Emission linewidth, gain saturation at higher optical power, and coupling between optical modes are important features that are no longer rendered by the model.

1.4 Contents

This thesis is organised as follows:

Chapter 1: Introduction. VCSEL device simulation is motivated and different VCSEL device types and applications are presented. General aspects, scope and limitations of the device model are outlined.

[4]Refer to Sec. 2.1 for a more detailed derivation.

Chapter 2: Device Model Equations. The laser model and its sub-components are discussed. Particular emphasis is on the optical cavity model. Electro-thermal transport model, carrier transport models at heterointerfaces and quantum wells are reviewed briefly.

Chapter 3: Simulator Implementation. The numerical formulation of the optical cavity model and the electro-thermal transport model using finite elements is presented. Numerical solution methods are described including an efficient scheme to self-consistently couple optical and electro-thermal equations.

Chapter 4: Simulation Benchmarks and Examples. The optical solver is compared to other methods. Spontaneous emission enhancement of a microcavity, and a calibrated self-consistent electro-thermo-optical simulation of a VCSEL device is presented. In order to demonstrate the practical use of the simulator as a design tool the simulation of a modulation response, and the task of finding a device structure with maximum single mode power is performed in a design tutorial.

Chapter 5: Conclusion. Conclusions are given and open issues are discussed.

Chapter 2

Device Model Equations

The VCSEL model outlined in Ch. 1 is described in more detail. The model shall predict spatially resolved electrical potential, electron and hole densities, local temperature, and mean optical intensity using a semiclassical microscopic laser device model. Furthermore, the electrical, thermal and optical terminal quantities are determined. Static device characteristics as well as modulation and transient response shall be covered by the model. The input parameters to the model equations are the topology of the device and the local physical material parameters.

The solution given here respects the trade off between selected *model complexity* and reasonable *computational effort* to solve the associated numerical problem. For this work the limit of *reasonable* was set at 1 day computation time on a given reference computer[1].

2.1 Laser Model

The common feature of all semiclassical laser models is that they treat the optical field as a classical quantity using Maxwell's equations, while the polarisation due to the active medium is described by quantum theory. The reason why the optical field can be treated classically is due to the high optical intensity, equivalent to a large

[1] HP/Compaq AlphaServer ES45 1250 MHz / 32 GBytes.

number of photons. The high intensity is a consequence of the laser action in potentially one discrete optical mode at frequency ω. The electromagnetic energy stored in this mode is therefore well approximated by a continuous value in a classical sense as opposed to a quantized value in packets of energy $\hbar\omega$.

Semiclassical laser models essentially differ

- in how Maxwell's equations are represented
- in the extent that quantum physics is used to describe the polarisation term in Maxwell's wave equation.

The choice of descriptions is dictated by the physical effects that are to be captured and the desired input $\rightarrow$ output characteristic of the model.

At the core of the model developed in this work lies the photon rate equation [21, 22, 23]. That is, the optical field is decomposed into a given number of modes at discrete frequencies, and the temporal evolution of the mean electromagnetic energy in each mode is described by a separate rate equation. Related work with respect to VCSEL simulation is described in [16, 24, 25].

2.1.1 Semiclassical Laser Theory

There are two categories of representations for Maxwell's equations: The first represents the optical field on the *fast time scale* given by the period of electromagnetic oscillations. The wavelength $\lambda = 1\ \mu$m corresponds to a frequency of approximately 300 THz or a period of 3.3 fs. A time discretisation in this representation would therefore be in the sub-femto seconds.

The second category simplifies the representation considerably by employing the *slowly varying amplitude* approximation. It benefits from the fact that under certain conditions to be specified shortly the electromagnetic field can be represented as a product of a slowly varying complex amplitude and a complex phase rotating at the frequency of the optical field. The slowly varying amplitude can, for instance, be the result of modulating the VCSEL with a 1 Gbit/s data stream. Consequently, a time discretisation six orders of magnitude coarser than in the first category results. If a current transient has to be

dealt with by the device model envisaged here using the given computational resources the slowly varying amplitude approximation must be used.

The first category of models is required in order to render effects that emerge from changes of the optical field that evolve on a shorter timescale than the round trip time of a photon in the optical cavity. In contrast, the second, approximative representation is valid if the period during which the optical field changes exceeds the photon round trip time by far. This time is very short in a VCSEL cavity (< 1 ps) due to its small size.

It is therefore essential how fast the amplitude of the optical field changes in order to know which one of the two categories applies. In a dielectric medium with negligible magnetic properties the constitutive equations are

$$\boldsymbol{D}(\boldsymbol{r},t) = \varepsilon_0 \boldsymbol{E}(\boldsymbol{r},t) + \boldsymbol{P}(\boldsymbol{r},t) + \boldsymbol{K}(\boldsymbol{r},t) \tag{2.1}$$

$$\boldsymbol{B}(\boldsymbol{r},t) = \mu_0 \boldsymbol{H}(\boldsymbol{r},t) \tag{2.2}$$

where $\boldsymbol{P}(\boldsymbol{r},t)$, $\boldsymbol{K}(\boldsymbol{r},t)$ are the polarisation terms, $\boldsymbol{E}(\boldsymbol{r},t)$ is the electric, $\boldsymbol{H}(\boldsymbol{r},t)$ the magnetic field, ε_0 and μ_0 are the vacuum permittivity and permeability, respectively.

The polarisation $\boldsymbol{P}(\boldsymbol{r},t)$ is the response of the active medium to the electric field. If a linear response is assumed it is obtained by convolution of the electric field with a response function

$$\boldsymbol{P}(\boldsymbol{r},t) = \varepsilon_0 \int_0^\infty \chi(\boldsymbol{r},t,\tau)\boldsymbol{E}(\boldsymbol{r},t-\tau)d\tau \tag{2.3}$$

where $\chi(\boldsymbol{r},t,\tau)$ is the causal, first order polarisation impulse response of the medium. Furthermore, $\boldsymbol{K}(\boldsymbol{r},t)$ represents the contribution to $\boldsymbol{D}(\boldsymbol{r},t)$ due to spontaneous emission and is, therefore, independent of the electric field.

Using Maxwell's equations in the time domain, with charge density and current set to zero, and making use of the constitutive equations Eqs. (2.1) and (2.2) yields Maxwell's wave equation in the time domain

$$\nabla \times [\nabla \times \boldsymbol{E}(\boldsymbol{r},t)] + \frac{1}{c_0^2}\frac{\partial^2}{\partial t^2}\left[\varepsilon_r(\boldsymbol{r},t,\tau) * \boldsymbol{E}(\boldsymbol{r},t-\tau)\right] = -\mu_0 \frac{\partial^2}{\partial t^2}\boldsymbol{K}(\boldsymbol{r},t) \tag{2.4}$$

where c_0 is the vacuum speed of light, the star denotes convolution in τ and

$$\varepsilon_r(\boldsymbol{r}, t, \tau) = \delta(\tau) + \chi(\boldsymbol{r}, t, \tau). \tag{2.5}$$

It is seen from Eqs. (2.4) and (2.5) that $\boldsymbol{E}(\boldsymbol{r}, t)$ can be excited by $\chi(\boldsymbol{r}, t, \tau)$ and $\boldsymbol{K}(\boldsymbol{r}, t)$.

It is assumed that the term $\chi(\boldsymbol{r}, t, \tau)$ is *quasi* time-translationally invariant. The response function $\chi(\boldsymbol{r}, t, \tau)$ has a limited range because the polarisation induced by a pulse of electric field decays after a short time ($\approx$ 100 fs [18, 19, 20]). However, $\chi(\boldsymbol{r}, t, \tau)$ is not time-translationally invariant because it depends on how strongly the material is polarised, which is time dependent if, for instance, the VCSEL is modulated. The modulation period is a lot longer (10 GHz corresponds to 100 ps) than the time needed for the polarisation to decay. Therefore, $\chi(\boldsymbol{r}, t, \tau)$ is time-translationally invariant on the time scale of the polarisation τ but varies slowly on the time scale t.

Whereas in semiclassical laser modeling two major categories of representing Maxwell's wave equation can be identified, many different ways of computing the polarisation have been proposed with varying degrees of rigour and computational requirements. An overview of some of the methods is given in [18, 20, 26, 27]. The method chosen in this work is presented in Secs. 2.1.3 and 2.1.4.

2.1.2 Photon Rate Equation

The photon round trip time is very short in a VCSEL cavity ($<$ 1 ps), due to its small size. Hence, the first order polarisation impulse response of the medium $\chi(\boldsymbol{r}, t, \tau)$ in Eq. (2.3) can be assumed time-translationally invariant. It is therefore valid to assume that the optical field depends only on the instantaneous value of the time-dependent dielectric function $\varepsilon_r(\boldsymbol{r}, t, \omega)$ [2]. Thus, the slowly varying amplitude approximation can be applied and holds up to high modulation frequencies[3].

[2] This is called the adiabatic approximation [21].

[3] Note that if the condition for the photon round trip time is only fulfilled marginally an additional criterion applies that also includes the modulation depth. If this criterion breaks down it turns out that the concept of the photon rate equation can still be maintained if the spontaneous emission term is modified [21].

Employing the mode expansion [21][4]

$$\boldsymbol{E}(\boldsymbol{r},t) = \sum_{k=1}^{N} a_k(t)\underline{\boldsymbol{E}}_k(\boldsymbol{r},t)e^{-i\int_0^t \omega_k'(\tau)d\tau} + c.c. \tag{2.6}$$

with the complex-valued vector $\underline{\boldsymbol{E}}_k(\boldsymbol{r},t)$, the complex-valued scalar $a_k(t)$ the real-valued scalar function $\omega_k'(t)$, and c.c. denoting the complex conjugate, Maxwell's wave equation

$$\nabla \times \mu_r^{-1}(\boldsymbol{r}) \cdot [\nabla \times \boldsymbol{E}(\boldsymbol{r},t)] + \frac{1}{c_0^2}\frac{\partial^2}{\partial t^2}\left[\varepsilon_r(\boldsymbol{r},t,\tau) * \boldsymbol{E}(\boldsymbol{r},t-\tau)\right] = \boldsymbol{F}(\boldsymbol{r},t) \tag{2.7}$$

is transformed into a set of N decoupled scalar differential equations

$$\frac{d}{dt}\mathsf{S}_k(t) = -2\omega_k''(t)\,\mathsf{S}_k(t) + R_k^{sp}(t) \tag{2.8}$$

with $k = 1,\ldots,N$, called photon rate equations, for the N optical modes considered, and the following eigenproblem

$$\begin{aligned} &\nabla \times \mu_r^{-1}(\boldsymbol{r}) \cdot [\nabla \times \underline{\boldsymbol{E}}_k(\boldsymbol{r},t)] + \frac{{\omega_k'}^2(t)}{c_0^2}\varepsilon_r(\boldsymbol{r},t,\omega_k') \cdot \underline{\boldsymbol{E}}_k(\boldsymbol{r},t) \\ &= \omega_k''(t)\,\tilde{\varepsilon}_r(\boldsymbol{r},t,\omega_k') \cdot \underline{\boldsymbol{E}}_k(\boldsymbol{r},t) \end{aligned} \tag{2.9}$$

to be evaluated for every t with

$$\begin{aligned} \tilde{\varepsilon}_r(\boldsymbol{r},t,\omega_k') &= \frac{\partial}{\partial\omega_k'}\left[\frac{\omega_k'(t)^2}{c_0^2}\varepsilon_r(\boldsymbol{r},t,\omega_k')\right] \\ &= \frac{2i\omega_k'(t)}{c_0^2}\left[\frac{\omega_k'(t)}{2}\frac{\partial}{\partial\omega_k'}\varepsilon_r(\boldsymbol{r},t,\omega_k') + \varepsilon_r(\boldsymbol{r},t,\omega_k')\right]. \end{aligned} \tag{2.10}$$

The photon rate equations describe the time evolution of electromagnetic energy $\mathsf{S}_\mu(t)$ in each mode. The source term $\boldsymbol{F}(\boldsymbol{r},t)$ replacing the right hand side in Eq. (2.4) is due to spontaneous emission. The term $R_k^{sp}(t)$ is its equivalent in the picture of the photon rate equation and is given in Sec. 2.1.4. The rate of change $2\omega_\mu''(t)$ is determined by the eigenvalue of Eq. (2.9). Because optical gain and

[4]Refer to App. A for more details on the derivation of Eqs. (2.7-2.12).

loss are present in $\mu_r^{-1}(\boldsymbol{r})$, $\varepsilon_r(\boldsymbol{r}, t, \omega_k')$ [5] and materials are reciprocal, Eq. (2.9) is a generalised, non-Hermitian, complex symmetric eigenproblem. The modal frequency $\omega_k'(t)$ can be found by solving Eq. (2.9) and requiring $\omega_k''(t)$ to be real-valued.

The eigenvector $\underline{\boldsymbol{E}}_k(\boldsymbol{r}, t)$ is the complex field representation of the optical mode k. The terms $\varepsilon_r(\boldsymbol{r}, t, \omega_k')$, $S_k(t)$, $\omega_k'(t)$, $\omega_k''(t)$ and $\underline{\boldsymbol{E}}_k(\boldsymbol{r}, t)$ are all functions of time that vary at most with the modulation.

Assuming the dielectric function

$$\varepsilon_r(\boldsymbol{r}, t, \omega_k') = \left(n(\boldsymbol{r}, t)^2 - \frac{c_0^2}{4{\omega_k'}^2} \alpha(\boldsymbol{r}, t)^2 \right) + i \frac{n(\boldsymbol{r}, t) c_0}{\omega_k'} \alpha(\boldsymbol{r}, t) \quad (2.11)$$

with refractive index $n(\boldsymbol{r}, t)$ and material absorption and gain $\alpha(\boldsymbol{r}, t)$ independent of ω_k' [6] and $|\omega_k''| \ll |\omega_k'|$, which is true for optical modes of practical VCSEL devices, the eigenproblem (2.9) can be rewritten in the familiar form

$$\nabla \times \mu_r^{-1}(\boldsymbol{r}) \cdot [\nabla \times \underline{\boldsymbol{E}}_k(\boldsymbol{r}, t)] = \frac{\omega_k^2(t)}{c_0^2} \varepsilon_r(\boldsymbol{r}, t, \omega_k) \cdot \underline{\boldsymbol{E}}_k(\boldsymbol{r}, t). \quad (2.12)$$

For practical calculations a linear eigenproblem is obtained if ω_k' in $\tilde{\varepsilon}_r(\boldsymbol{r}, t, \omega_k')$ of Eq. (2.9) and ω_k in $\varepsilon_r(\boldsymbol{r}, t, \omega_k)$ of Eq. (2.12) are set to a fixed reference frequency ω_0 which is chosen close to the frequencies of the modes under consideration. Consequently, the solutions of Eq. (2.9) can be normalised and the orthogonality relation be given by the following generalised inner product with respect to the reference ω_0 [21, 22] [7]

$$\left(\underline{\boldsymbol{E}}_i(\boldsymbol{r}, t), \underline{\boldsymbol{E}}_j(\boldsymbol{r}, t) \right)_{\tilde{\varepsilon}, \omega_0} = \iiint_V \underline{\boldsymbol{E}}_i(\boldsymbol{r}, t) \cdot \tilde{\varepsilon}_r(\boldsymbol{r}, t, \omega_0) \cdot \underline{\boldsymbol{E}}_j(\boldsymbol{r}, t) \, dV = \delta_{ij} \quad (2.13)$$

where V is the mode volume[8].

In general, as the laser simulation evolves in time, $\omega_k(t)$ and $\underline{\boldsymbol{E}}_k(\boldsymbol{r}, t)$ and $R_k^{sp}(t)$ have to be re-evaluated.

---

[5] The material functions $\mu_r^{-1}(\boldsymbol{r})$ and $\varepsilon_r(\boldsymbol{r}, t, \omega_k')$ will later turn out to be tensors and therefore the dot product applies.

[6] Since the ω_k' of the set of modes considered are close together in frequency this is a valid assumption.

[7] The optical mode pattern $\underline{\boldsymbol{E}}_i(\boldsymbol{r}, t)$ used here was defined in Eq. 2.6 and has unit 1.

[8] The mode volume V will defined in Sec. 2.2.3.

2.1.3 Optical Material Gain and Loss

The local optical material gain (negative sign) and absorption (positive sign) in the quantum well active region with respect to energy E is given by [23, 26]

$$\alpha(\boldsymbol{r}, E) = C_0 \sum_{i,j} \int_0^\infty |M_{i,j}|^2 \rho^{el}(\boldsymbol{r}, E')(f_i^C(\boldsymbol{r}, E') + f_j^V(\boldsymbol{r}, E') - 1) \cdot L(E, E')\, dE' \quad \left[\mathrm{cm}^{-1}\right] \tag{2.14}$$

with

$$C_0 = \frac{\pi\, e^2}{n(\boldsymbol{r})\, c_0\, \varepsilon_0\, m_0^2\, \omega}. \tag{2.15}$$

Here $|M_{i,j}|^2$ is the optical matrix element, $\rho^{el}(\boldsymbol{r}, E')$ the reduced electronic density of states, $f_i^C(\boldsymbol{r}, E')$ and $f_j^V(\boldsymbol{r}, E')$ the local Fermi-Dirac distributions of electrons and holes at temperature $T(\boldsymbol{r})$ and quasi Fermi energies $E_{F,n}^{2D}(\boldsymbol{r})$ and $E_{F,p}^{2D}(\boldsymbol{r})$, $L(E, E')$ is the linewidth broadening function [23], $n(\boldsymbol{r})$ is the refractive index, and m_0 the free electron mass. Integration is over energy space and summation is over the electron and hole sub-bands of the quantum well. Formulas for the optical matrix element are given in [26].

Free carrier theory is employed to calculate the optical gain and Fermi's Golden Rule is applied. An effective mass parabolic band approximation with a linear temperature dependence of the band gap is used for the bandstructure of electrons, light and heavy holes, which is a fair assumption for the AlGaAs/GaAs system. Flat bands are assumed in real space. This assumption is valid if the diode is turned on in the forward conducting state which is true for a laser diode above threshold. The stationary Schrödinger equation is solved in 1D to obtain the quantum-mechanical wave functions for bound states and the corresponding sub-band structure of the quantum well. Strain is included using a single band approximation. The quasi Fermi energies $E_{F,n}^{2D}$ and $E_{F,p}^{2D}$ govern the occupation of the combined states of all conduction sub-bands or valence sub-bands, respectively [23].

The simulation approach used here is not limited to the above assumptions. More advanced models are available if an increase in

computational effort can be afforded. In [28, 29] the bandstructure is determined by a $k \cdot p$ calculation including strain and valence band mixing effects. Moreover, the optical gain is computed taking into account tilting of the band edges in real space. It is feasible to include many-body effects up to the screened Hartree-Fock approximation. Due to the high computational requirements more rigorous treatments are only possible in special cases [20, 29, 30].

The assumption of Fermi distributions for carriers is not valid in general. It breaks down, for instance, in the case of strong spectral hole burning, in which carriers are distributed in energy space according to a non-equilibrium distribution. Nevertheless, in the VCSEL case, a quantum kinetic approach [18] has shown that for realistic carrier carrier scattering rates $1/\tau_{c-c} \approx 10$ ps^{-1} optical intensities are normally not sufficiently high to burn spectral holes in a semiconductor active medium. If required, spectral hole burning can be included empirically via a gain saturation term [31].

Outside the active region the dielectric function uses static parameters. That is, constant complex refractive indices are assumed for optical absorption induced by carriers or metallic regions (Sec. 3.1.1).

2.1.4 Spontaneous Emission

A rigorous model of spontaneous emission requires a quantum mechanical description of the optical field [32], which semiclassical laser theory does not provide. The spontaneous emission process depends on the spectral mode density given by its environment. That is, spontaneous emission can be enhanced or inhibited with respect to the situation in free space by placing the electron-hole pairs in a resonant cavity. This is called the Purcell effect. In a VCSEL cavity one has such a situation.

Since this work aims at modeling VCSEL operation above threshold, the power contributed by the spontaneous emission term $R_k^{sp}(t)$ in Eq. (2.8) will be negligible on the scale of the laser output power, and is only required to initiate the laser action. Moreover, since the optical losses of the cavity are rather high, lasing threshold currents will not be affected by a change of $R_k^{sp}(t)$ within the bounds of typical spontaneous emission enhancement factors [33]. Thus, in the simulation examples presented in Ch. 4 the free space optical mode density

is used instead of the optical mode density in the cavity[9].

The local spontaneous emission photon rate per unit volume per energy interval is given by [23, 26]

$$r^{sp}(\boldsymbol{r},E) = C_0 \frac{c_0}{n(\boldsymbol{r})} \rho^{opt}(\boldsymbol{r},E) \sum_{i,j} \int_0^\infty |M_{i,j}|^2 \rho^{el}(\boldsymbol{r},E') f_i^C(\boldsymbol{r},E') f_j^V(\boldsymbol{r},E') \cdot L(E,E')\, dE' \quad \left[\mathrm{s}^{-1}\mathrm{cm}^{-3}\mathrm{eV}^{-1}\right] \tag{2.16}$$

where the meaning of the parameters is the same as in Eq. (2.14). The enhancement or inhibition of spontaneous emission is taken into account classically by the optical mode density function $\rho^{opt}(\boldsymbol{r},E)$, which gives the number of states with photon energy E per unit volume and energy interval in cm^{-3} eV^{-1}. In a VCSEL cavity the optical mode density depends on the direction of the polarisation vector. Therefore, $\rho^{opt}(\boldsymbol{r},E)$ gives an effective mode density averaged over the solid angle.

The spontaneous emission photon rate contribution $R_k^{sp}(t)$ to mode k in Eq. (2.8) is [22, 23]

$$R_k^{sp}(t) = \mathrm{Re}\left[\frac{(\underline{\boldsymbol{E}}_k(\boldsymbol{r},t), \tilde{r}^{sp}(\boldsymbol{r},\hbar\omega_k')\underline{\boldsymbol{E}}_k(\boldsymbol{r},t))_{\tilde{\varepsilon},\omega_0}}{(\underline{\boldsymbol{E}}_k(\boldsymbol{r},t), \underline{\boldsymbol{E}}_k(\boldsymbol{r},t))_{\tilde{\varepsilon},\omega_0}}\right] \quad \left[\mathrm{s}^{-1}\right] \tag{2.17}$$

using the inner product (2.13) and the rate given by[10]

$$\tilde{r}^{sp}(\boldsymbol{r},E) = C_0 \frac{c_0}{n(\boldsymbol{r})} \sum_{i,j} \int_0^\infty |M_{i,j}|^2 \rho^{el}(\boldsymbol{r},E') f_i^C(\boldsymbol{r},E') f_j^V(\boldsymbol{r},E') \cdot L(E,E')\, dE' \quad \left[\mathrm{s}^{-1}\right]. \tag{2.18}$$

For this choice of units for $R_k^{sp}(t)$ the scalar S_k in Eq. (2.8) corresponds to the number of photons in mode k.

[9] Clearly, such reasoning does not apply to spontaneous emission devices as resonant-cavity LEDs (RCLED) [34] or to investigations into VCSEL spontaneous emission power.

[10] This is the spontaneous emission rate $r^{sp}(\boldsymbol{r},E)$ in Eq. (2.16) before shaping with the optical mode density function $\rho^{opt}(\boldsymbol{r},E)$.

2.2 Optical Cavity Model

A VCSEL cavity is by nature an open boundary structure: the main purpose of the device is to emit electromagnetic energy stored in optical modes inside the cavity into free space. It is essential to know how high the emission rate of this radiation is, how much of it is available at the aperture of the VCSEL, and how much is lost due to radiation in other directions. In practical VCSEL devices additional scattered radiation is often caused by oxide apertures and related device features which can lead to unwanted additional cavity losses. Equally, such scattering effects can be employed to introduce losses *by design*. The goal is to control the emission of each mode individually and, for instance, to enhance power emitted by a wanted optical mode and suppress others. Moreover, in devices such as resonant cavity light emitting diodes (RCLED) the mode density is altered to achieve enhanced spontaneous emission. Clearly, these emission phenomena are only present when the VCSEL cavity is modeled as an open structure. Practical VCSEL simulation examples in which the effect of the open boundary is demonstrated are given in Ch. 4.

The actual VCSEL cavity structure, as pointed out in Sec. 1.3, is described in terms of a dielectric function

$$\varepsilon_r(\boldsymbol{r},\omega) = \varepsilon_r'(\boldsymbol{r},\omega) + i\varepsilon_r''(\boldsymbol{r},\omega) \tag{2.19}$$

with a potentially arbitrary spatial profile. It assumes a complex valued form in the frequency domain due to the presence of optical gain and loss. In addition, the fact that the spatial profile can change stepwise has to be accounted for.

If general VCSEL structures are to be treated, the scalar approximation of Maxwell's vectorial wave equation assuming weak guidance does no longer hold [35]. Furthermore, due to the cylindrical symmetry of the VCSEL cavity, electromagnetic waves can no longer be decomposed into scalar TE and TM waves as is possible for a planarly layered medium with infinite extension in layer direction. Instead, hybrid vectorial HE and EH modes are obtained. Hence, a general VCSEL structure demands solving Maxwell's vectorial wave equation.

The inhomogeneous form in the frequency domain of Eq. (2.12) is

given by

$$\nabla \times \mu_r(\boldsymbol{r})^{-1} \cdot [\nabla \times \underline{\boldsymbol{E}}(\boldsymbol{r})] - \frac{\omega^2}{c_0^2} \varepsilon_r(\boldsymbol{r}) \cdot \underline{\boldsymbol{E}}(\boldsymbol{r}) = \underline{\boldsymbol{F}}(\boldsymbol{r}, \omega) \tag{2.20}$$

subject to an open boundary. The term $\underline{\boldsymbol{F}}(\boldsymbol{r}, \omega)$ corresponds to a source of finite extent as, for instance, given by spontaneous emission in the active region. At frequency ω of the source the response of the cavity is given by the electric field $\underline{\boldsymbol{E}}(\boldsymbol{r})$.

If $\underline{\boldsymbol{F}}(\boldsymbol{r}, \omega)$ is set to $\mathbf{0}$ the eigenproblem (2.12)

$$\nabla \times \mu_r(\boldsymbol{r})^{-1} \cdot (\nabla \times \underline{\boldsymbol{E}}_k(\boldsymbol{r})) = \frac{\omega_k^2}{c_0^2} \varepsilon_r(\boldsymbol{r}) \cdot \underline{\boldsymbol{E}}_k(\boldsymbol{r}) \tag{2.21}$$

results. The solutions $\omega_k = \omega_k' - i\omega_k''$ and $\underline{\boldsymbol{E}}_k(\boldsymbol{r})$ are the complex eigenfrequency and eigenmode respectively, with ω_k' the resonance angular velocity and ω_k'' the rate of increase (negative sign) or decay (positive sign) of the electric field of mode k.

Equation (2.21) has nontrivial solutions $\underline{\boldsymbol{E}}_k(\boldsymbol{r}) \neq \mathbf{0}$ with $\nabla \times \underline{\boldsymbol{E}}_k(\boldsymbol{r}) \equiv \mathbf{0}$, the nullspace of the curl, and consequently $\omega_k = 0$. These solutions are equivalent to the ones that can be obtained by taking the gradient of a certain scalar function $\phi(\boldsymbol{r})$

$$\underline{\boldsymbol{E}}(\boldsymbol{r}) = -\nabla\phi(\boldsymbol{r}). \tag{2.22}$$

They correspond to static $\omega_k = 0$ solutions when the presence of a certain distribution of free charges is assumed. Although no charges were assumed originally in Sec. 2.1.1 such a hypothetical charge distribution does not alter the form of Eqs. (2.20) and (2.21). Hence, in order to reinstate the no charges requirement and to suppress the static solutions the divergence free condition

$$\nabla \cdot \varepsilon_r(\boldsymbol{r}) \cdot \underline{\boldsymbol{E}}(\boldsymbol{r}) \equiv 0 \tag{2.23}$$

has to be imposed in addition to Eqs. (2.20) and (2.21). This condition is implicitly assumed throughout this work.

In order to reconstruct the response to an arbitrary source distribution $\underline{\boldsymbol{F}}(\boldsymbol{r}, \omega)$ in an inhomogeneous medium it is useful to define a diadic Green's function $\underline{\boldsymbol{G}}(\boldsymbol{r}, \boldsymbol{r}')$ as follows [36]

$$\nabla \times \left(\mu_r(\boldsymbol{r})^{-1} \cdot (\nabla \times \underline{\boldsymbol{G}}(\boldsymbol{r}, \boldsymbol{r}'))\right) - \frac{\omega^2}{c_0^2} \varepsilon_r(\boldsymbol{r}) \cdot \underline{\boldsymbol{G}}(\boldsymbol{r}, \boldsymbol{r}') = \mu_r(\boldsymbol{r}) \underline{\boldsymbol{I}} \delta(\boldsymbol{r} - \boldsymbol{r}') \tag{2.24}$$

as response to a point dipole source with a certain orientation given by the unity vector $\underline{\boldsymbol{I}}$. By virtue of linearity the response to an arbitrary source $\underline{\boldsymbol{F}}(\boldsymbol{r},\omega)$ oscillating at frequency ω can be written as the superposition of responses to point sources at $\boldsymbol{r}'$

$$\underline{\boldsymbol{E}}(\boldsymbol{r}) = \iiint_{V_F} \underline{\boldsymbol{G}}(\boldsymbol{r},\boldsymbol{r}') \cdot \underline{\boldsymbol{F}}(\boldsymbol{r}',\omega) d\boldsymbol{r}' \tag{2.25}$$

over the domain V_F where the source is nonzero.

2.2.1 Uniqueness of Solutions

In order to further discuss the implications of a cavity with open boundaries the uniqueness theorem for boundary value problems has to be recalled. It provides the conditions under which a solution to Eq. (2.20) is unique. These are the boundary conditions, and, additionally, the radiation condition for open boundary problems.

Uniqueness of Solutions for the Bounded Problem

Consider first the problem bounded by a surface Γ_V shown in Fig. 2.1a with a source of finite extent and an inhomogeneity of finite extent given by $\varepsilon_r(\boldsymbol{r})$ and $\mu_r(\boldsymbol{r})^{-1}$. Two solutions of Eq. (2.20) for ω real-valued are called $\underline{\boldsymbol{E}}^{(1)}(\boldsymbol{r})$ and $\underline{\boldsymbol{E}}^{(2)}(\boldsymbol{r})$ and their associated magnetic fields $\underline{\boldsymbol{H}}^{(1)}(\boldsymbol{r})$ and $\underline{\boldsymbol{H}}^{(2)}(\boldsymbol{r})$, respectively, are given by the relation

$$\underline{\boldsymbol{H}}(\boldsymbol{r}) = \frac{1}{i\omega}\mu_0\mu_r(\boldsymbol{r})^{-1} \cdot \nabla \times \underline{\boldsymbol{E}}(\boldsymbol{r}). \tag{2.26}$$

The uniqueness theorem states that the two solutions $\underline{\boldsymbol{E}}^{(1)}(\boldsymbol{r})$, $\underline{\boldsymbol{H}}^{(1)}(\boldsymbol{r})$ and $\underline{\boldsymbol{E}}^{(2)}(\boldsymbol{r})$, $\underline{\boldsymbol{H}}^{(2)}(\boldsymbol{r})$ are identical for all $\boldsymbol{r}$ if

- $\mathbf{e}_n \times \underline{\boldsymbol{E}}^{(1)} = \mathbf{e}_n \times \underline{\boldsymbol{E}}^{(2)}$ on part of Γ_V and $\mathbf{e}_n \times \underline{\boldsymbol{H}}^{(1)} = \mathbf{e}_n \times \underline{\boldsymbol{H}}^{(2)}$ on the rest of Γ_V.

and $\varepsilon_r(\boldsymbol{r})$, $\mu_r(\boldsymbol{r})^{-1}$ provide loss or gain and $\mathbf{e}_n$ is the unity vector normal to the boundary Γ_V. That is, provided either a net loss or gain is present in the cavity, and the two solutions for a real-valued ω satisfy the same boundary condition for the tangential component of $\underline{\boldsymbol{E}}$ or $\underline{\boldsymbol{H}}$ the two solutions are identical for all $\boldsymbol{r}$ inside Γ_V [36].

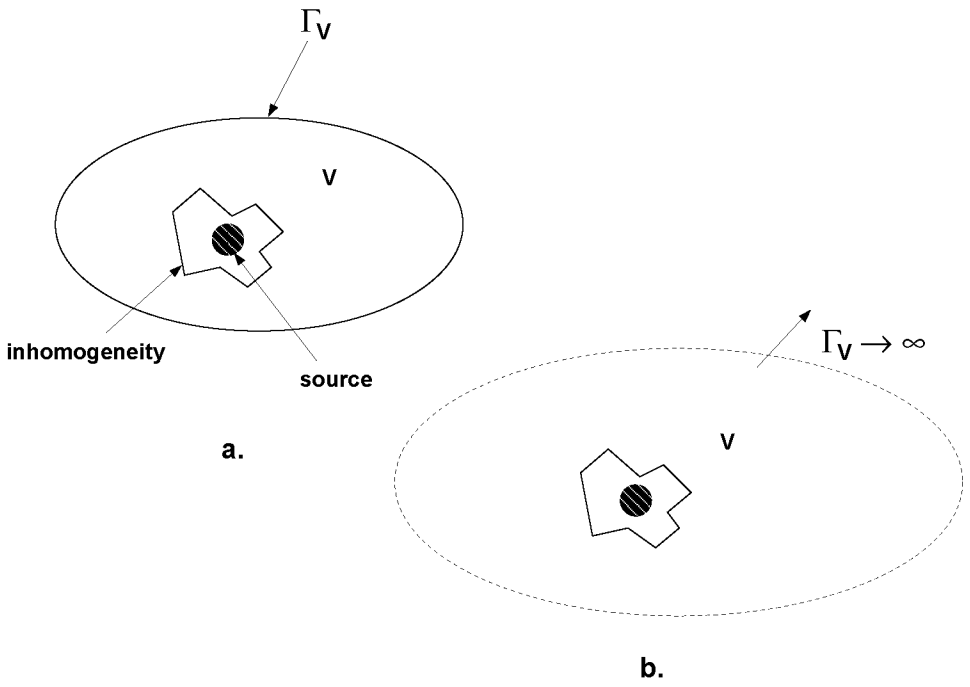

Figure 2.1: Radiation losses in VCSEL Cavity; (a) bounded problem, (b) open boundary problem

Loss or gain have to be present in such a way that the resonances ω_k given by Eq. (2.21) are shifted off the real axis in the complex plane. If an ω_k comes to lie on the real axis the uniqueness of the solution for $\omega = \omega_k$ in Eq. (2.20) can no longer be guaranteed. It is then possible to generate multiple distinct solutions by superposing the particular solution of Eq. (2.20) with an arbitrary linear combination of eigenvector solutions (corresponding to eigenvalue ω_k) of the homogeneous problem in Eq. (2.21). Uniqueness can in this case be reinstalled by adding an arbitrarily small constant gain or loss to both $\varepsilon_r(\boldsymbol{r})$, $\mu_r(\boldsymbol{r})^{-1}$. In this way, uniqueness can be achieved even if, as is the case for practical VCSEL cavities, loss and gain are present concurrently.

In the following, homogeneous boundary conditions will be used. That is, one of

- $\mathbf{e}_n \times \underline{\boldsymbol{E}}(\boldsymbol{r}) = \mathbf{0}$, the perfectly electric conducting (PEC) surface
- $\mathbf{e}_n \times \underline{\boldsymbol{H}}(\boldsymbol{r}) = \mathbf{0}$, the perfectly magnetic conducting (PMC) surface

will be used.

Uniqueness of Solutions for the Open Boundary Problem

Consider now the problem bounded by a surface $\Gamma_V \to \infty$ shown in Fig. 2.1b with a source of finite extent and an inhomogeneity of finite extent placed at the origin. The inhomogeneity is given by $\varepsilon_r(\boldsymbol{r})$ and $\mu_r(\boldsymbol{r})^{-1}$. When $\Gamma_V \to \infty$ the resonance frequencies ω_k of Eq. (2.21) become gradually denser and eventually form a continuum in the limit. This implies that uniqueness of solutions of Eq. (2.20) is not guaranteed at any frequency ω. The same remedy as in the last section will be applied here to obtain uniqueness. A small loss is introduced. With this small loss $\underline{\boldsymbol{E}}_k(\boldsymbol{r})$ will either decrease exponentially when $|\boldsymbol{r}| \to \infty$ (if the wave is outgoing) or increase exponentially when $|\boldsymbol{r}| \to \infty$ (if the wave is incoming). If only the outgoing solutions are kept, which are the solutions that are relevant from a physical point of view, uniqueness is reestablished.

The uniqueness theorem stated for the bounded problem can be extended for open boundary problems as follows. The two solutions $\underline{\boldsymbol{E}}^{(1)}(\boldsymbol{r})$ ($\underline{\boldsymbol{H}}^{(1)}(\boldsymbol{r})$) and $\underline{\boldsymbol{E}}^{(2)}(\boldsymbol{r})$ ($\underline{\boldsymbol{H}}^{(2)}(\boldsymbol{r})$) are identical for all $\boldsymbol{r}$ if

- only outgoing waves are allowed at the boundary $\Gamma_V \to \infty$.

This can be achieved by introducing an arbitrarily small constant loss in $\varepsilon_r(\boldsymbol{r})$ and $\mu_r(\boldsymbol{r})^{-1}$ [36].

In conclusion, the boundary conditions at Γ_V assure that a solution to Eq. (2.20) is unique. If the problem has an open boundary, additionally, the radiation condition, only outgoing waves at $\Gamma_V \to \infty$, can be invoked to maintain uniqueness[11].

2.2.2 Practical Radiation Boundary Conditions

Numerical calculations can only deal with finite size computational problems. For arbitrarily shaped sources and inhomogeneities of finite extent it is therefore often not possible to impose the true radiation condition because of the infinite nature of the condition: *only outgoing waves at* $\Gamma_V \to \infty$.

[11] A similar treatment can be applied to extend the validity of Huygens' Principle to open boundary problems.

A practical open boundary problem is therefore characterised as follows in the context of this work: there is a region of interest V that contains the finite source and inhomogeneity. The region V is bounded by the surface Γ_V at a finite distance from its contents. Outside this boundary electromagnetic waves are only outgoing. Therefore, the radiation condition at Γ_V is an approximation of the true radiation condition that requires outgoing waves at $|\boldsymbol{r}| \to \infty$. If the finite element method is used to solve Eqs. (2.20) and (2.21) inside Γ_V the radiation condition at Γ_V is replaced by an artificial boundary condition on Γ_V. The aim is to make the boundary appear as transparent as possible to outgoing waves or, put differently, to minimise non physical reflections from the boundary. Different boundary conditions have been devised for this purpose:

- *Absorbing Boundary Conditions* (ABC)
- *Boundary Integral Equations*
- *Eigenfunction Expansions*

The main advantage of ABCs is that they lead to localised relations between the fields at the boundary. It will become apparent in Sec. 3.1.3 that this retains the highly sparse structure of the finite element systems matrices, which enables their treatment by efficient standard numerical methods. The disadvantage is that ABCs realise the radiation condition only approximately. In order to keep the error low they have to be placed some distance away from the finite source and inhomogeneity[12]. An overview of classical methods is given in [37]. A more recent approach employing so-called Perfectly Matched Layers (PML) will be presented in Sec. 2.2.3.

The boundary integral method incorporates the radiation condition using appropriate Green's functions for the exterior fields. As a result the domain that has to be discretised by finite elements for the interior fields can be kept to a minimum. The interior and exterior fields are coupled using the field continuity conditions at the interface Γ_V of the interior and exterior region. Boundary integral methods have the disadvantage of being inflexible if large classes of

[12] As rule of thumb placing the boundary Γ_V "a couple of wavelengths" away from the VCSEL cavity produces reasonable results.

different structures have to be dealt with. Furthermore, they yield full or partially full system matrices whose numerical treatment requires excessive amounts of memory and computation time.

Alternatively, the exterior fields can be expanded in eigenfunctions instead of Green's functions as in the method described previously. The two methods are closely related since, in theory, a Green's function can always be expressed in terms of an eigenfunction expansion. Similar advantages and disadvantages follow. An overview of the boundary integral and eigenfunction expansion method is given in [38].

In summary, ABCs are suitable if the inhomogeneity inside Γ_V consists of many small homogeneous regions or, in the limit, continuously changing material properties as in the case of a VCSEL cavity. For problems with large, piecewise homogeneous regions, for example problems that address antenna radiation and scattering from perfectly conducting objects in air, the boundary integral and eigenfunction expansion method are appropriate. Additionally, as will be shown, ABCs give accurate results as long as most of the electromagnetic energy of a solution is concentrated within Γ_V. Otherwise poor accuracy results and boundary integral and eigenfunction expansion methods have to be used.

Solutions of Eq. (2.21) for a free dielectric sphere subject to the radiation condition will be presented as an illustration [39, 40]. The advantage of this example is that, due to the spherical symmetry of the problem, placing Γ_V at the sphere/air interface is equivalent to placing it at $\Gamma_V \to \infty$. The problem is then reduced to fulfilling the interface conditions at the sphere/air interface for the electromagnetic wave inside the sphere and waves that are only outgoing outside the sphere. The solutions can be separated in TE and TM waves. Semi-analytic solutions are available for this problem. That is, the expressions for the electric and magnetic field $\underline{\boldsymbol{E}}_k(\boldsymbol{r})$, $\underline{\boldsymbol{H}}_k(\boldsymbol{r})$ can be written down explicitely using the complex resonance frequency ω_k that is obtained by numerically solving the transcendent characteristic equation for TE_{nmr} waves

$$\frac{J_{n-1/2}(Z_{nmr})}{J_{n+1/2}(Z_{nmr})} = \frac{H^{(2)}_{n-1/2}(\frac{Z_{nmr}}{\sqrt{\varepsilon_r}})}{\sqrt{\varepsilon_r} H^{(2)}_{n+1/2}(\frac{Z_{nmr}}{\sqrt{\varepsilon_r}})} \tag{2.27}$$

and for TM_{nmr} waves

$$\frac{n}{Z_{nmr}} - \frac{J_{n-1/2}(Z_{nmr})}{J_{n+1/2}(Z_{nmr})} = \frac{n \cdot \varepsilon_r}{Z_{nmr}} - \sqrt{\varepsilon_r}\frac{H^{(2)}_{n-1/2}(\frac{Z_{nmr}}{\sqrt{\varepsilon_r}})}{H^{(2)}_{n+1/2}(\frac{Z_{nmr}}{\sqrt{\varepsilon_r}})} \tag{2.28}$$

with

$$Z_{nmr} = \frac{\sqrt{\varepsilon_r \mu_r}}{c_0} r_0 \left(\omega'_{nmr} + i\omega''_{nmr}\right). \tag{2.29}$$

For each integer $n \geq 1$ there is a corresponding discrete set of solutions ω_{nmr} in r. The system is degenerate in the index m that governs the periodicity of the field in azimuthal direction. The terms ε_r and μ_r are the relative permittivity and permeability of the sphere, respectively, and are assumed $\varepsilon_r = \mu_r = 1$ for air. Furthermore, r_0 is the radius of the sphere and c_0 the speed of light in vacuum. The term $J_{n+1/2}$ is the first kind Bessel function and $H^{(2)}_{n+1/2}$ the Hankel function of the second kind of the order $n+1/2$. For details of the field solution refer to [39].

The characteristic equations can be solved with arbitrary finite precision. The problem, therefore, lends itself perfectly as a benchmark to assess methods of imposing the radiation condition, as for instance PML.

Figures 2.2a and 2.2b show the results of Eq. 2.27 (TE waves) and Figs. 2.3a and 2.3b show the results of Eq. 2.28 (TM waves) for a variation in ε_r. Two distinct types of solutions can be identified. For $\varepsilon_r \to \infty$ solutions are either the zeroes of the first kind Bessel function where Z_{nmr} is finite and real-valued, or the zeroes of the second kind Hankel function where $Z_{nmr}/\sqrt{\varepsilon_r}$ is finite and complex-valued. The former can be identified in Fig. 2.2a as a curve virtually constant with $\varepsilon_r \to \infty$, whereas the latter is a curve increasing exponentially on a semilogarithmic scale. The former will be called *interior* and the latter *exterior* solutions. The distinction between interior and exterior modes is clear for any value of ε_r in the TE case. In the TM case, however, coupling phenomena between the two types are evident. The two types of modes can be explained physically. The interior modes concentrate the electromagnetic energy in the volume of the sphere or close to its surface. In contrast, exterior modes concentrate the electromagnetic energy outside the sphere. In the limit $\varepsilon_r \to \infty$ the

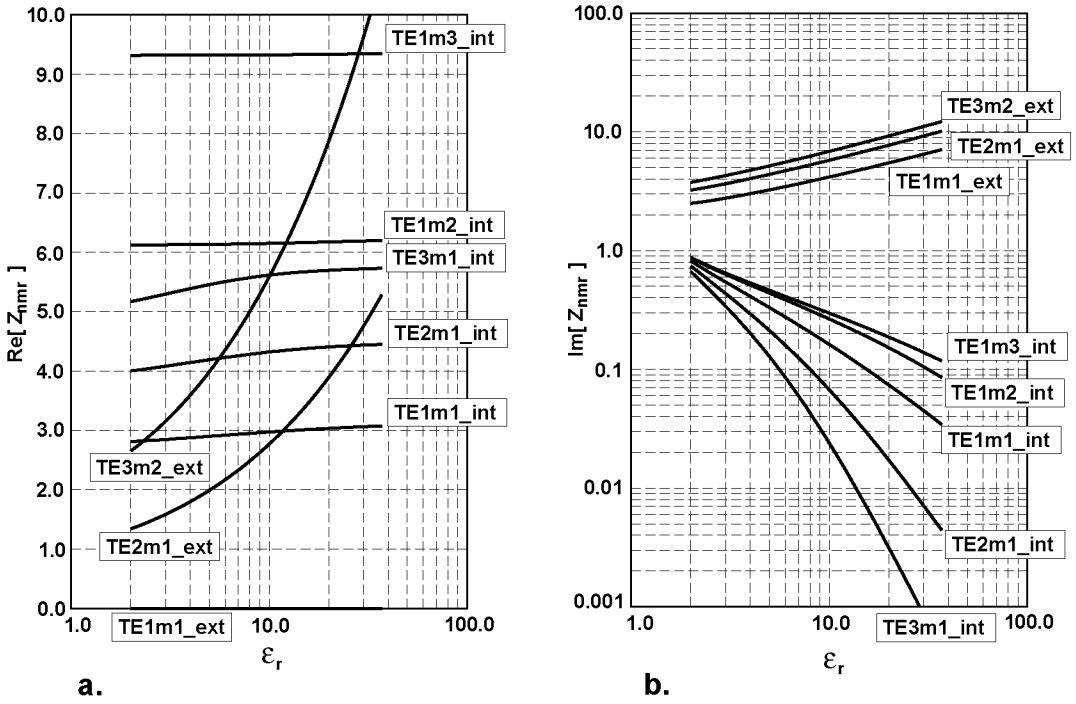

Figure 2.2: TE interior (int) and exterior (ext) mode eigenvalues Z_{nmr} versus ε_r of the free dielectric sphere; (a) Re $[Z_{nmr}]$, (b) Im $[Z_{nmr}]$.

surface becomes totally reflective and waves can exist only either on the inside (zero of the first kind Bessel function) or the outside (zero of the second kind Hankel function) of the sphere. Only interior modes can achieve quality factors $Q \gg 1$ that are of practical relevance in optical resonators. The Q factor of external modes is always smaller than 1.

2.2.3 Perfectly Matched Layers

The perfectly matched interface proposed in [41] is an interface between two half spaces. One of them is lossy, the Perfectly Matched Layer (PML), and the interface is non-reflecting for plane waves of all frequencies and all angles of incidence and polarisations. The PML is therefore an ABC that can be used to truncate a computational domain.

The principle underlying the PML concept is most easily understood by interpreting it as a coordinate stretching method in the fre-

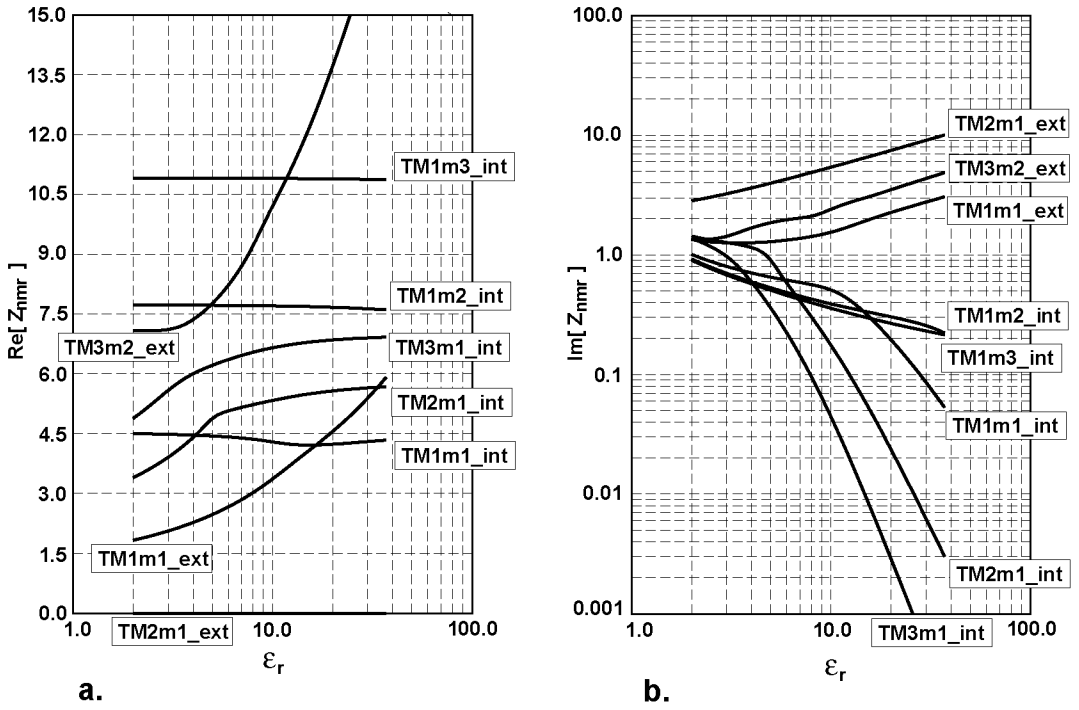

Figure 2.3: TM interior (int) and exterior (ext) mode eigenvalues Z_{nmr} versus ε_r of the free dielectric sphere; (a) $\mathrm{Re}\,[Z_{nmr}]$, (b) $\mathrm{Im}\,[Z_{nmr}]$.

quency domain [38, 42]. This view is summarized in the first half of this section. In the second half the validity of using a PML to truncate a computational domain is assessed by the free dielectric sphere example.

Consider the source-free, modified Maxwell equations in the frequency domain

$$\nabla_s \times \underline{\boldsymbol{E}}(\boldsymbol{r}) = i\omega\mu_0\mu_r\underline{\boldsymbol{H}}(\boldsymbol{r}) \tag{2.30}$$
$$\nabla_s \times \underline{\boldsymbol{H}}(\boldsymbol{r}) = -i\omega\varepsilon_0\varepsilon_r\underline{\boldsymbol{E}}(\boldsymbol{r}) \tag{2.31}$$
$$\nabla_s \cdot (\varepsilon_0\varepsilon_r\underline{\boldsymbol{E}}(\boldsymbol{r})) = 0 \tag{2.32}$$
$$\nabla_s \cdot (\mu_0\mu_r\underline{\boldsymbol{H}}(\boldsymbol{r})) = 0 \tag{2.33}$$

with ∇_s defined as

$$\nabla_s = \frac{1}{s_x}\frac{\partial}{\partial_x}\boldsymbol{e}_x + \frac{1}{s_y}\frac{\partial}{\partial_y}\boldsymbol{e}_y + \frac{1}{s_z}\frac{\partial}{\partial_z}\boldsymbol{e}_z \tag{2.34}$$

for the Cartesian coordinate system, that is, the standard ∇ operator with coordinates stretched by certain factors s_x, s_y and s_z. Similar formulations exist for cylindrical, spherical coordinate systems and anisotropic ε_r and μ_r [43]. Here, ε_r and μ_r are assumed isotropic.

First, the behaviour of a plane wave subject to the modified Maxwell equations shall be investigated. The plane wave

$$\underline{\boldsymbol{E}}(\boldsymbol{r}) = \underline{\boldsymbol{E}}_0 e^{i\boldsymbol{k}\boldsymbol{r}} \tag{2.35}$$
$$\underline{\boldsymbol{H}}(\boldsymbol{r}) = \underline{\boldsymbol{H}}_0 e^{i\boldsymbol{k}\boldsymbol{r}} \tag{2.36}$$

with wave vector $\boldsymbol{k}$ is inserted in Eqs. (2.30-2.33). The set of equations

$$\boldsymbol{k}_s \times \underline{\boldsymbol{E}}(\boldsymbol{r}) = \omega\mu_0\mu_r\underline{\boldsymbol{H}}(\boldsymbol{r}) \tag{2.37}$$
$$\boldsymbol{k}_s \times \underline{\boldsymbol{H}}(\boldsymbol{r}) = -\omega\varepsilon_0\varepsilon_r\underline{\boldsymbol{E}}(\boldsymbol{r}) \tag{2.38}$$
$$\boldsymbol{k}_s \cdot (\varepsilon_0\varepsilon_r\underline{\boldsymbol{E}}(\boldsymbol{r})) = 0 \tag{2.39}$$
$$\boldsymbol{k}_s \cdot (\mu_0\mu_r\underline{\boldsymbol{H}}(\boldsymbol{r})) = 0 \tag{2.40}$$

with

$$\boldsymbol{k}_s = \frac{k_x}{s_x}\boldsymbol{e}_x + \frac{k_y}{s_y}\boldsymbol{e}_y + \frac{k_z}{s_z}\boldsymbol{e}_z \tag{2.41}$$

is then obtained. Taking the cross product $(\boldsymbol{k}_s\times)$ of Eq. (2.37) gives

$$\boldsymbol{k}_s \times [\boldsymbol{k}_s \times \underline{\boldsymbol{E}}(\boldsymbol{r})] = \omega\mu_0\mu_r \boldsymbol{k}_s \times \underline{\boldsymbol{H}}(\boldsymbol{r}) = -\frac{\omega^2}{c_0^2}\mu_r\varepsilon_r \underline{\boldsymbol{E}}(\boldsymbol{r}). \tag{2.42}$$

Using the vector identity $\boldsymbol{a}\times(\boldsymbol{b}\times\boldsymbol{c}) = (\boldsymbol{a}\cdot\boldsymbol{c})\,\boldsymbol{b} - (\boldsymbol{a}\cdot\boldsymbol{b})\,\boldsymbol{c}$ on the last equation and applying Eq. (2.39) yields

$$(\boldsymbol{k}_s \cdot \boldsymbol{k}_s)\,\underline{\boldsymbol{E}}(\boldsymbol{r}) = \frac{\omega^2}{c_0^2}\mu_r\varepsilon_r \underline{\boldsymbol{E}}(\boldsymbol{r}) \tag{2.43}$$

for all $\boldsymbol{r}$ and hence the dispersion relation

$$\boldsymbol{k}_s \cdot \boldsymbol{k}_s = \left(\frac{k_x}{s_x}\right)^2 + \left(\frac{k_y}{s_y}\right)^2 + \left(\frac{k_z}{s_z}\right)^2 = \frac{\omega^2}{c_0^2}\mu_r\varepsilon_r = \kappa^2. \tag{2.44}$$

The latter equation describes the surface of a sphere and the solutions for $\boldsymbol{k}$ are

$$\boldsymbol{k} = \kappa s_x \sin\theta\cos\varphi\cdot\boldsymbol{e}_x + \kappa s_y \sin\theta\sin\varphi\cdot\boldsymbol{e}_y + \kappa s_z\cos\theta\cdot\boldsymbol{e}_z. \tag{2.45}$$

Going back to Eqs. (2.35) and (2.36), it can be seen that a wave will be attenuated in the x direction if s_x is a complex number, and similarly for the y and z directions.

Next, the plane wave reflection by the interface between two half spaces 1 and 2, with stretching factors s_{1x}, s_{1y}, s_{1z} and s_{2x}, s_{2y}, s_{2z} is investigated. For the TE case with $\underline{\boldsymbol{E}}(\boldsymbol{r})$ perpendicular to the z direction (Fig. 2.4) the incident, reflected and transmitted fields can be written as

$$\underline{\boldsymbol{E}}^i(\boldsymbol{r}) = \underline{\boldsymbol{E}}_0 e^{i\boldsymbol{k}^i\boldsymbol{r}} \tag{2.46}$$

$$\underline{\boldsymbol{E}}^r(\boldsymbol{r}) = R^{TE}\underline{\boldsymbol{E}}_0 e^{i\boldsymbol{k}^r\boldsymbol{r}} \tag{2.47}$$

$$\underline{\boldsymbol{E}}^t(\boldsymbol{r}) = T^{TE}\underline{\boldsymbol{E}}_0 e^{i\boldsymbol{k}^t\boldsymbol{r}}. \tag{2.48}$$

Using tangential continuity conditions at the interface for the electric and magnetic field the reflection and transmission coefficients

$$R^{TE} = \frac{k_{1z}s_{2z}\mu_{r2} - k_{2z}s_{1z}\mu_{r1}}{k_{1z}s_{2z}\mu_{r2} + k_{2z}s_{1z}\mu_{r1}} \tag{2.49}$$

$$T^{TE} = \frac{2k_{1z}s_{2z}\mu_{r2}}{k_{1z}s_{2z}\mu_{r2} + k_{2z}s_{1z}\mu_{r1}} \tag{2.50}$$

$$\tag{2.51}$$

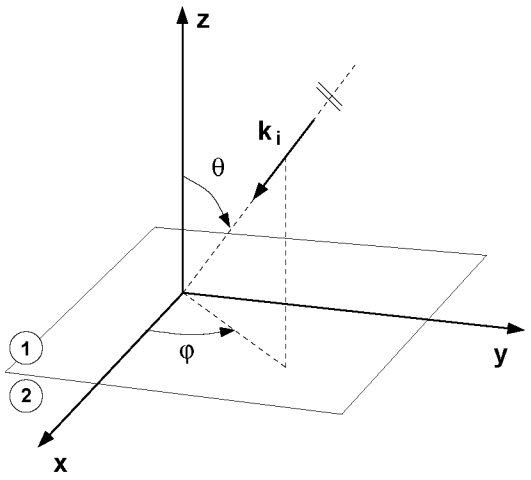

Figure 2.4: Plane wave reflection at an interface between two half spaces.

and similarly for the TM case

$$R^{TM} = \frac{k_{1z}s_{2z}\varepsilon_{r2} - k_{2z}s_{1z}\varepsilon_{r1}}{k_{1z}s_{2z}\varepsilon_{r2} + k_{2z}s_{1z}\varepsilon_{r1}} \tag{2.52}$$

$$T^{TM} = \frac{2k_{1z}s_{2z}\varepsilon_{r2}}{k_{1z}s_{2z}\varepsilon_{r2} + k_{2z}s_{1z}\varepsilon_{r1}} \tag{2.53}$$

are obtained. The phase matching conditions $k_{1x} = k_{2x}$ and $k_{1y} = k_{2y}$ give

$$\kappa_1 s_{1x} \sin\theta_1 \cos\varphi_1 = \kappa_2 s_{2x} \sin\theta_2 \cos\varphi_2 \tag{2.54}$$

$$\kappa_1 s_{1y} \sin\theta_1 \sin\varphi_1 = \kappa_2 s_{2y} \sin\theta_2 \sin\varphi_2. \tag{2.55}$$

Setting $\varepsilon_{r1} = \varepsilon_{r2}$, $\mu_{r1} = \mu_{r2}$, $s_{1x} = s_{2x}$ and $s_{1y} = s_{2y}$ yields

$$\theta_1 = \theta_2, \quad \varphi_1 = \varphi_2, \quad R^{TE} = 0, \quad R^{TM} = 0, \tag{2.56}$$

independent of the choice for s_{1z} and s_{2z}, the frequency and the angle of incidence. For $s_{2z} = s' + is''$ evanescent waves with $\mathrm{Im}\,[k_{1z}] > 0$ decay faster with $s' \geq 1$ and propagating waves with $\mathrm{Re}\,[k_{1z}] > 0$ decay exponentially with $s'' \geq 1$ in half space 2.

According to Eqs. (2.41) and (2.35) the propagating waves will be attenuated by the factor

$$e^{\kappa_2 s'' z \cos\theta} \tag{2.57}$$

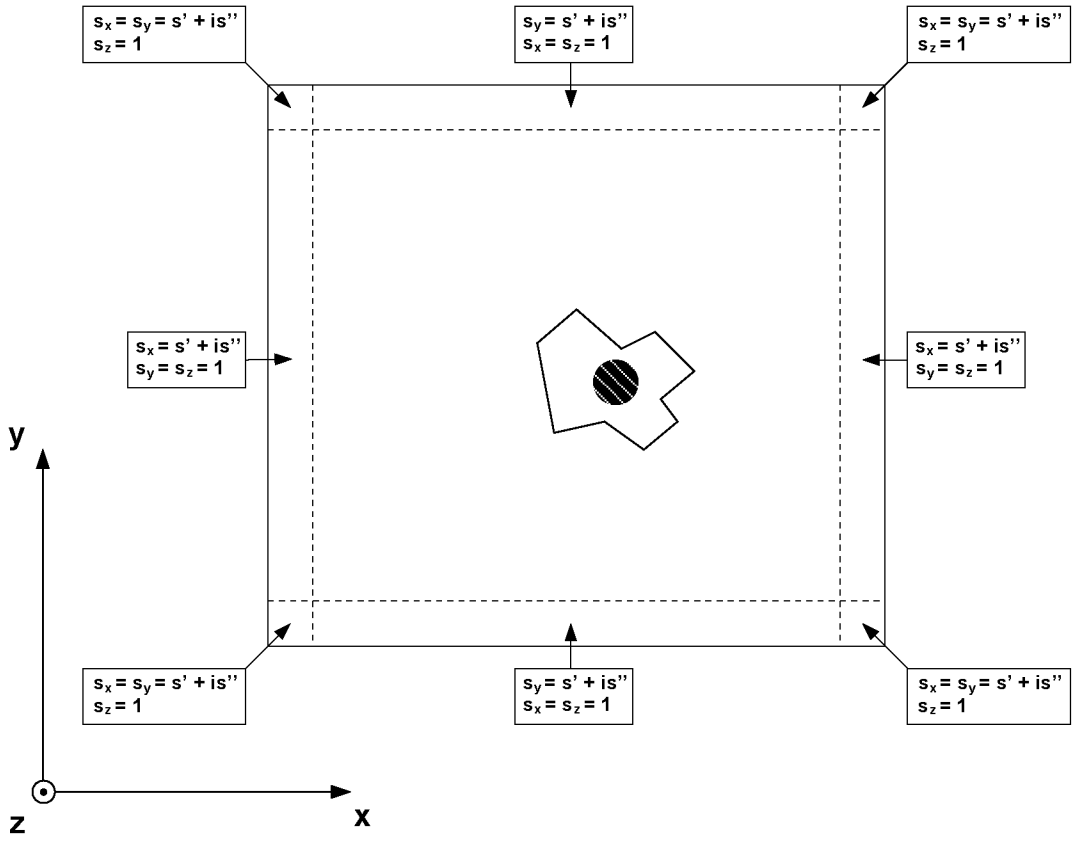

Figure 2.5: Choice of s_x, s_y and s_z for PML terminated by PEC boundary.

in the z direction. If the computational domain is truncated with a Dirichlet boundary at a distance L from the interface, the magnitude of residual reflections due to the Dirichlet boundary becomes

$$|R(\theta)| = e^{-2\kappa_2 s'' L \cos\theta} \tag{2.58}$$

assuming κ_2 to be real valued. Moreover, the perfectly matched interface is only non-reflecting for the continuous problem. Discretisation by finite elements introduces additional parasitic reflections.

The choice of s_x, s_y and s_z in a transversal plane that is normal to the z axis is shown in Fig. 2.5. The extension of the scheme along the z axis is straightforward.

In the remaining part of this section the validity of the PML ABC is assessed using the free dielectric sphere example introduced in Sec. 2.2.2. The results computed by the finite element method

employing a PML ABC to truncate the computational domain are compared to the accurate semi-analytic solutions of the problem.

Figures 2.6 and 2.7 show the interior modes of a free dielectric sphere with radius 1 μm . The cross-section of the sphere is approximated with a 50 segment polygon. Inside the PML region $s' = 1$, and s'' evolves with a quadratic profile from $s''_I = 0$ on Γ_I to $s''_O = 5.0$ on Γ_O according to App. B. All results are given for the same second order $\approx \lambda/20$ discretisation with a sphere to PML separation d_{sep} of 2.90λ and a PML thickness d_{PML} of 0.75λ. The structure specifications are with respect to $\lambda = 6.6$ μm which corresponds to the vacuum wavelength of the interior TE1m1 mode at $\varepsilon_r \approx 10$ [13].

Figures 2.8 and 2.9 show the effect of changing the PML parameter s''_O and varying the separation d_{sep}, respectively. Results change only slightly if d_{sep} is varied and as long as $s''_O \approx 5.0$. Note that results for very weak confinements are affected only.

The experiment shows that finite elements combined with a PML ABC are suitable for modeling interior modes of radiating cavities as long as they sufficiently concentrate the electromagnetic energy in their volume, that is, in the sphere example, for sufficiently high ε_r. For weak confinements the dispersion characteristic of the finite element / PML solution changes to an exterior like solution, although the semi-analytic reference solution continues to show interior type behaviour. This is demonstrated in Fig. 2.6 for the interior TE1m1 mode when $\varepsilon_r < 5$ ($Q < 3$). The transition from interior to exterior with changing ε_r for this mode is also apparent in the optical field pattern shown in Fig. 2.10. Although finite elements with PML ABC yield solutions with exterior type dispersion characteristic they have no correspondence to the true exterior modes of the cavity. With the exception of TE1m1, finite element solutions in Figs. 2.6 and 2.7 are only shown down to values of ε_r where they still correctly reproduce the respective interior modes. At lower values the spectrum is contaminated with the mentioned incorrect exterior type solutions.

Despite these shortcomings for very weak confinements the combination of finite elements with a PML ABC is perfectly suited for

[13] Inside and in the vicinity of the sphere the mesh density is increased by a factor of $\sqrt{\varepsilon_r}$ for $\varepsilon_r = 10$. Note that the relative mesh density with respect to the vacuum wavelength of the interior TE1m1 mode varies as the latter changes from 3.2 μm to 12.5 μm over the range considered here.

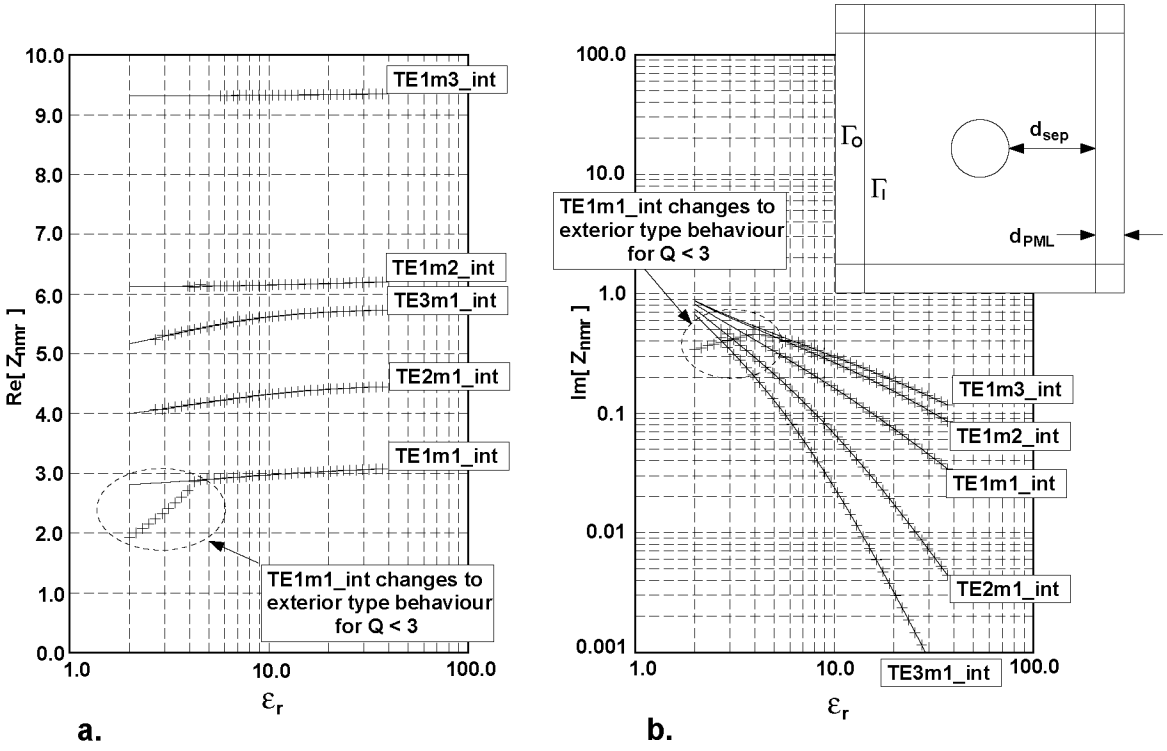

Figure 2.6: TE interior mode eigenvalues Z_{nmr} versus ε_r of the free dielectric sphere; $d_{sep} = 2.90\lambda$, $d_{PML} = 0.75\lambda$ at $\lambda = 6.6$ μm, $s''_O = 5.0$; semi-analytic solution (solid line) and finite element solution +: (a) Re $[Z_{nmr}]$, (b) Im $[Z_{nmr}]$.

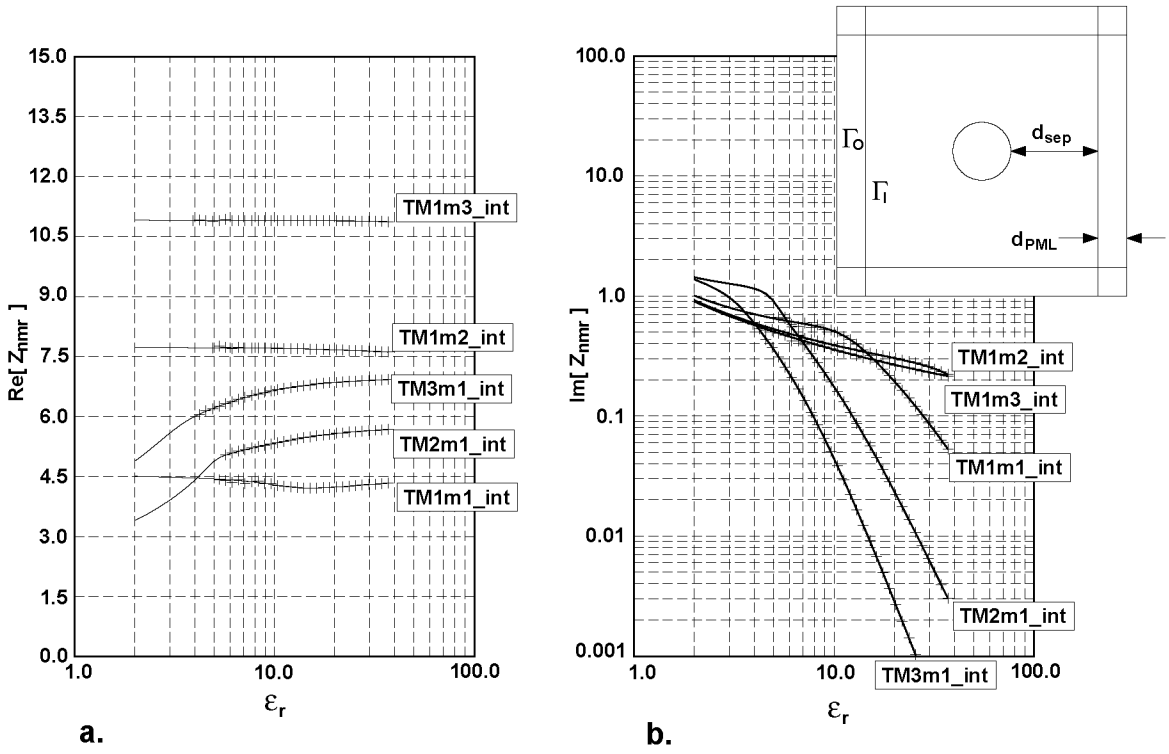

Figure 2.7: TM interior mode eigenvalues Z_{nmr} versus ε_r of the free dielectric sphere; $d_{sep} = 2.90\lambda$, $d_{PML} = 0.75\lambda$, at $\lambda = 6.6$ μm, $s''_O = 5.0$; semi-analytic solution (solid line) and finite element solution +: (a) $\mathrm{Re}\,[Z_{nmr}]$, (b) $\mathrm{Im}\,[Z_{nmr}]$.

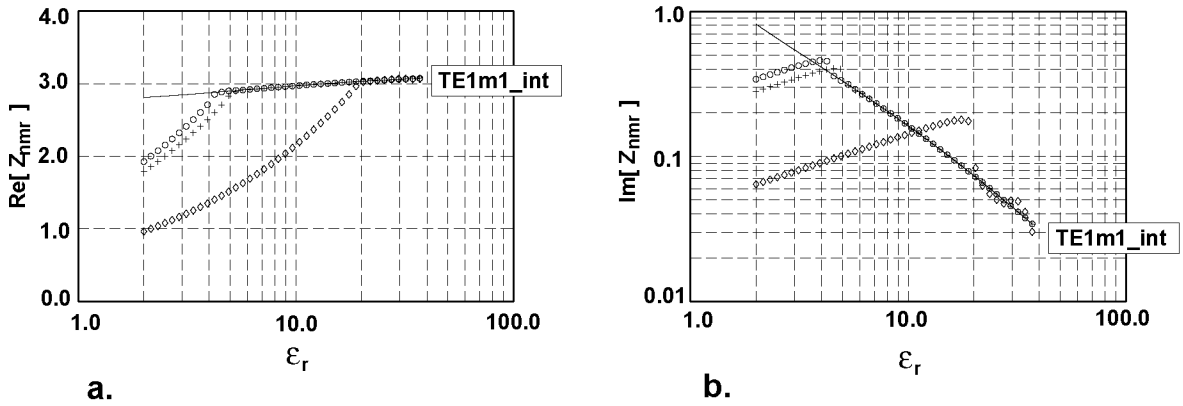

Figure 2.8: TE1m1 interior mode eigenvalue Z_{1m1} versus ε_r of the free dielectric sphere; $d_{sep} = 2.90\lambda$, $d_{PML} = 0.75\lambda$, at $\lambda = 6.6$ μm; semi-analytic solution (solid line) and finite element solution $s''_O = 1.0$ $\diamond$, $s''_O = 5.0$ $\circ$, $s''_O = 25.0$ + : (a) $\mathrm{Re}\,[Z_{1m1}]$, (b) $\mathrm{Im}\,[Z_{1m1}]$.

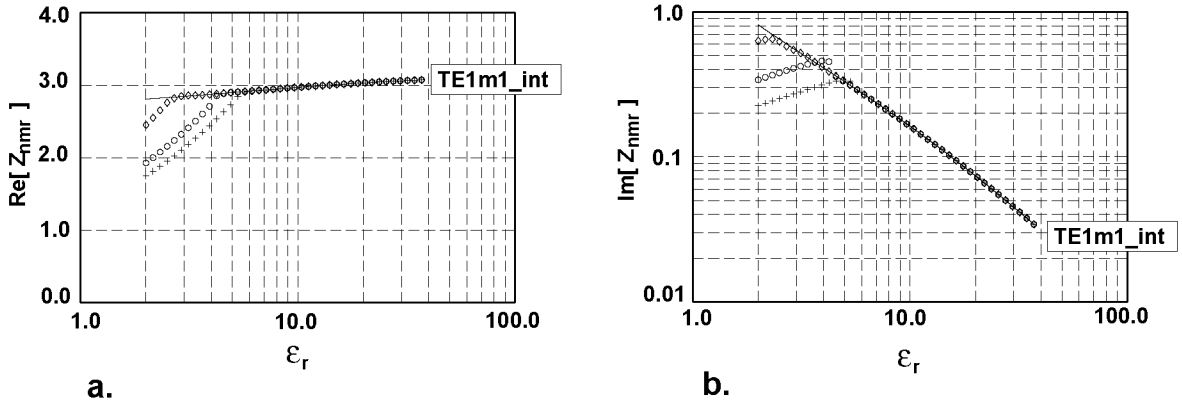

Figure 2.9: TE1m1 interior mode eigenvalue Z_{1m1} versus ε_r of the free dielectric sphere; $d_{PML} = 0.75\lambda$, at $\lambda = 6.6$ μm, $s''_O = 5.0$; semi-analytic solution (solid line) and finite element solution $d_{sep} = 1.4\lambda$ $\diamond$, $d_{sep} = 2.9\lambda$ $\circ$, $d_{sep} = 4.4\lambda$ $+$: (a) $\mathrm{Re}\,[Z_{1m1}]$, (b) $\mathrm{Im}\,[Z_{1m1}]$.

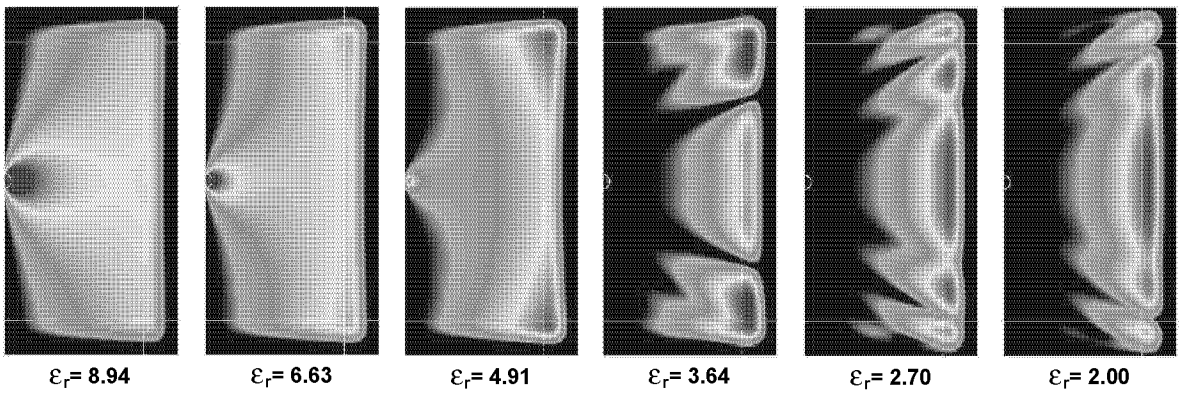

Figure 2.10: Intensity of TE1m1 interior mode, logarithmic colour scale; transition from solution with electromagnetic energy concentrated inside sphere to solution with energy concentrated outside sphere.

the task of modeling VCSEL optical resonators because their Q values are orders of magnitude in excess of the limit detected here for a dielectric sphere. Remember that the high Q values in VCSEL optical resonators are achieved by highly reflective diffractive mirrors.

2.2.4 Electromagnetic Energy Density and Its Rate of Change

In order to compute the optical power generated in the active region, the power coupled through the aperture of a VCSEL device and dissipated in the DBR material, etc. the *modal* parameter ω_k'' in the photon rate equation (2.8), has to be decomposed into its constituents. Moreover, it will be shown in Sec. 2.4 that it is necessary to compute the local generation and dissipation of optical energy to compute the local carrier recombination and generation rate.

In order to obtain these parameters it is helpful to calculate the local generation and dissipation rates of optical energy for a medium with local optical gain and loss, recalling that the latter was derived from quantum mechanical considerations. These local quantities are summed up appropriately over space and yield the required modal parameters.

It is assumed here that the rate of change of the field amplitudes and frequency is small compared to their frequency. It is then possible to use a stationary time dependence of the electric and magnetic fields in complex phasor notation

$$\boldsymbol{E}(\boldsymbol{r},t) = \sqrt{2}\mathrm{Re}\left[\underline{\boldsymbol{E}}(\boldsymbol{r})\, e^{-i\omega t}\right] \tag{2.59}$$

$$\boldsymbol{H}(\boldsymbol{r},t) = \sqrt{2}\mathrm{Re}\left[\underline{\boldsymbol{H}}(\boldsymbol{r})\, e^{-i\omega t}\right] \tag{2.60}$$

to compute the local instantaneous energy density and its rate of change. This is a valid approximation on the time scale of a modulation period within the bounds that were defined in Sec. 2.1. The dependence of the field amplitudes and frequency on the slow timescale is omitted here for the sake of clarity.

The local time dependent Poynting vector, electric and magnetic energy density are [44]

$$\begin{aligned}\boldsymbol{S}(\boldsymbol{r},t) &= \boldsymbol{E}(\boldsymbol{r},t) \times \boldsymbol{H}(\boldsymbol{r},t) \\ &= \mathrm{Re}\left[\underline{\boldsymbol{E}}(\boldsymbol{r}) \times \underline{\boldsymbol{H}}^*(\boldsymbol{r}) + \underline{\boldsymbol{E}}(\boldsymbol{r}) \times \underline{\boldsymbol{H}}(\boldsymbol{r})\, e^{-2i\omega t}\right]\end{aligned} \tag{2.61}$$

$$w_e(\boldsymbol{r},t) = \frac{1}{2}\boldsymbol{D}(\boldsymbol{r},t)\cdot\boldsymbol{E}(\boldsymbol{r},t)$$
$$= \frac{1}{2}\mathrm{Re}\left[\underline{\boldsymbol{E}}^T(\boldsymbol{r})\cdot\varepsilon_0\varepsilon_r(\boldsymbol{r})\cdot\underline{\boldsymbol{E}}^*(\boldsymbol{r}) + \underline{\boldsymbol{E}}^T(\boldsymbol{r})\cdot\varepsilon_0\varepsilon_r(\boldsymbol{r})\cdot\underline{\boldsymbol{E}}(\boldsymbol{r})\,e^{-2i\omega t}\right] \tag{2.62}$$

$$w_m(\boldsymbol{r},t) = \frac{1}{2}\boldsymbol{B}(\boldsymbol{r},t)\cdot\boldsymbol{H}(\boldsymbol{r},t)$$
$$= \frac{1}{2}\mathrm{Re}\left[\underline{\boldsymbol{H}}^T(\boldsymbol{r})\cdot\mu_0\mu_r(\boldsymbol{r})\cdot\underline{\boldsymbol{H}}^*(\boldsymbol{r}) + \underline{\boldsymbol{H}}^T(\boldsymbol{r})\cdot\mu_0\mu_r(\boldsymbol{r})\cdot\underline{\boldsymbol{H}}(\boldsymbol{r})\,e^{-2i\omega t}\right] \tag{2.63}$$

written as the sum of contributions constant and oscillating at frequency 2ω. Due to Faraday's equation

$$\nabla\times\underline{\boldsymbol{E}}(\boldsymbol{r}) = i\omega\mu_0\mu_r(\boldsymbol{r})\underline{\boldsymbol{H}}(\boldsymbol{r}) \tag{2.64}$$

Eq. (2.63) can be recast in terms of the electric field

$$w_m(\boldsymbol{r},t) = \frac{1}{2}\mathrm{Re}\Big\{\left[\nabla\times\underline{\boldsymbol{E}}(\boldsymbol{r})\right]^T\cdot\frac{1}{\omega^2\mu_0}\left[\mu_r^{-1}(\boldsymbol{r})\right]^*\cdot\left[\nabla\times\underline{\boldsymbol{E}}^*(\boldsymbol{r})\right]$$
$$+\left[\nabla\times\underline{\boldsymbol{E}}(\boldsymbol{r})\right]^T\cdot\frac{1}{\omega^2\mu_0}\mu_r^{-1}(\boldsymbol{r})\cdot\left[\nabla\times\underline{\boldsymbol{E}}(\boldsymbol{r})\right]e^{-2i\omega t}\Big\}. \tag{2.65}$$

Noticing that the real part of a complex number does not change when the complex conjugate of it is taken

$$\langle w(\boldsymbol{r})\rangle = \frac{1}{2}\mathrm{Re}\Big\{\underline{\boldsymbol{E}}^T(\boldsymbol{r})\cdot\varepsilon_0\varepsilon_r(\boldsymbol{r})\cdot\underline{\boldsymbol{E}}^*(\boldsymbol{r})$$
$$+\left[\nabla\times\underline{\boldsymbol{E}}(\boldsymbol{r})\right]^T\cdot\frac{1}{\omega^2\mu_0}\mu_r^{-1}(\boldsymbol{r})\cdot\left[\nabla\times\underline{\boldsymbol{E}}^*(\boldsymbol{r})\right]\Big\} \tag{2.66}$$

is obtained for the total local electromagnetic energy averaged over time. If PMLs are employed, ∇_s presented in Sec. 2.2.3, instead of ∇ should be used in all equations. Alternatively, if PMLs are interpreted as complex anisotropic diagonal tensor material, as will be shown in Sec. 3.1.1, $\varepsilon_r(\boldsymbol{r})$ and $\mu_r(\boldsymbol{r})$ are complex diagonal tensors.

According to Poynting's theorem the divergence of Eq. (2.61) averaged over time, that is, the local mean generation or dissipation rate of electromagnetic energy per volume, can be written as

$$\langle\nabla\cdot\boldsymbol{S}(\boldsymbol{r})\rangle = \mathrm{Re}\left[\underline{\boldsymbol{H}}^*(\boldsymbol{r})\cdot(\nabla\times\underline{\boldsymbol{E}}(\boldsymbol{r})) - \underline{\boldsymbol{E}}(\boldsymbol{r})\cdot(\nabla\times\underline{\boldsymbol{H}}^*(\boldsymbol{r}))\right], \tag{2.67}$$

which by Eq. (2.64) and Ampere's equation

$$\nabla \times \underline{\boldsymbol{H}}(\boldsymbol{r}) = -i\omega\varepsilon_0\varepsilon_r\underline{\boldsymbol{E}}(\boldsymbol{r}) \tag{2.68}$$

can be rewritten in terms of the electric field only

$$\begin{aligned}\langle \nabla \cdot \boldsymbol{S}(\boldsymbol{r})\rangle = \mathrm{Re}\Big[& i\omega\underline{\boldsymbol{E}}^T(\boldsymbol{r}) \cdot \varepsilon_0\varepsilon_r(\boldsymbol{r}) \cdot \underline{\boldsymbol{E}}^*(\boldsymbol{r}) \\ & - \left(\nabla \times \underline{\boldsymbol{E}}(\boldsymbol{r})\right)^T \cdot \frac{i}{\omega\mu_0}\mu_r^{-1}(\boldsymbol{r}) \cdot \left(\nabla \times \underline{\boldsymbol{E}}^*(\boldsymbol{r})\right)\Big],\end{aligned} \tag{2.69}$$

again noticing that taking the complex conjugate does not change the result.

Integrating Eqs. (2.66) and (2.69) over a certain volume gives the electromagnetic energy and its generation or dissipation rate for that region. For example, the power coupled through the aperture of the VCSEL device can be calculated as

$$P_{out} = \iiint\limits_{TPML} \langle \nabla \cdot \boldsymbol{S}(\boldsymbol{r})\rangle \, dV \tag{2.70}$$

with $TPML$ defined in Fig. 2.11. Similarly, the optical power generated in the active region, the power dissipated in the DBRs, the laterally radiated power, etc. can be calculated individually.

Assume that the electric field is given by optical mode k. By normalising the power supplied from a source or dissipated to a sink with the optical energy stored in the mode a characteristic energy transfer rate is obtained. In the example of the power coupled through the aperture this is

$$L_{out,k} = \frac{\iiint\limits_{TPML} \langle \nabla \cdot \boldsymbol{S}_k(\boldsymbol{r})\rangle \, dV}{\iiint\limits_{O} \langle w_k(\boldsymbol{r})\rangle \, dV} \tag{2.71}$$

with O bounded by Γ_O shown in Fig. 2.11. In the limit of a scalar electric field approximation Eq. (2.71) for the modal gain and loss is equivalent to the so-called overlap integral [14][14].

[14] In simple rate equation models this is replaced by $\Gamma v_g \alpha$ where Γ is the confinement factor, v_g is the group velocity, and α is the material gain or loss.

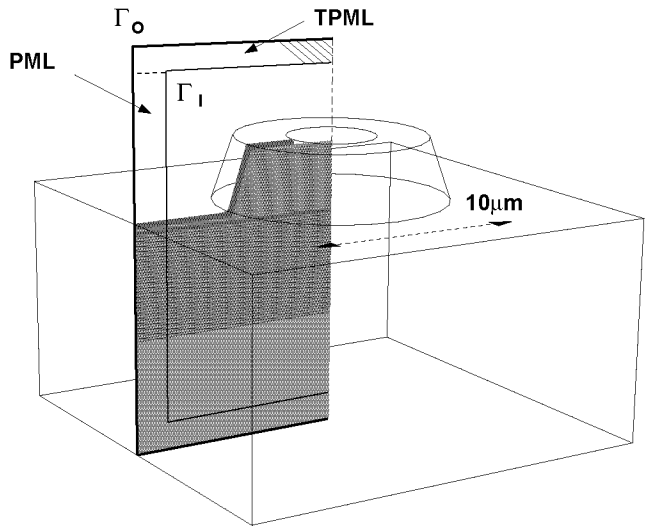

Figure 2.11: The region labelled TPML is the portion of the PML lining that absorbs the usable optical power emitted through the aperture of the VCSEL.

2.2.5 Variational Principle

Variational methods were originally developed to solve problems in theoretical physics. The basic idea is to formulate the physical problem in terms of a functional that has a stationary property at the exact solution of the problem. A functional is a mapping from a vector space to a scalar space. Often this scalar has a direct physical significance. In a second step trial functions are used to approximate the solution in order to minimise or maximise the functional.

With the advent of the computer it was shown that variational methods are ideally suited to formulate boundary value problems that are to be solved using numerical methods. It will be shown in Sec. 3.1.3 how this applies to the finite element method. Alternatively, Galerkin's Method can be used. An important advantage of the variational method over the latter is that the difference between essential and natural boundary conditions is clearly demonstrated.

Whether the variational method is applicable or not therefore depends on the availability of a variational formulation of a physical problem. In electromagnetics the physical problem is usually given in terms of differential equations (Eq. 2.20). In [36, 38] a route to deriving functionals for wave equations in electromagnetics is outlined.

The generalised variational principle has to be applied to Eq. (2.20). Due to optical gain, loss, and a radiation condition imposed by PML $\varepsilon_r(\boldsymbol{r})$ and $\mu_r(\boldsymbol{r})$ are complex symmetric tensors. Using homogeneous Dirichlet (PEC) and von Neumann (PMC) boundary conditions, the variational functional reads[15]

$$\begin{aligned} F(\underline{\boldsymbol{E}}) =& \frac{1}{2} \iiint_O \left[(\nabla \times \underline{\boldsymbol{E}}) \cdot \mu_r^{-1} \cdot (\nabla \times \underline{\boldsymbol{E}}) - \frac{\omega^2}{c_0^2} \varepsilon_r \cdot \underline{\boldsymbol{E}} \cdot \underline{\boldsymbol{E}} \right] dV \\ & - \iiint_O \underline{\boldsymbol{E}} \cdot \underline{\boldsymbol{F}}(\omega)\, dV. \end{aligned} \tag{2.72}$$

The dependence of $\underline{\boldsymbol{E}}$ and $\underline{\boldsymbol{F}}$ on $\boldsymbol{r}$ is omitted for the sake of clarity. Integration is over O given in Fig. 2.11. Homogeneous von Neumann boundary conditions (PMC) are natural boundary conditions. Homogeneous Dirichlet boundary conditions are essential boundary conditions and have to be imposed in addition to finding the stationary point of Eq. (2.72). For the eigenproblem Eq. (2.21) the variational functional is given by Eq. (2.72) with the source term $\underline{\boldsymbol{F}}(\omega)$ set to zero.

The Rayleigh-Ritz method is used here to formulate the variational functional Eq. (2.72) as a numerical problem. It is based on the idea that an approximation of the accurate solution of Eq. (2.20) can be found by minimising or maximising the variational functional Eq. (2.72) with respect to a test function that is inserted. This can be done by varying the coefficients c_j of a test function expanded like

$$\underline{\tilde{\boldsymbol{E}}}(\boldsymbol{r}) = \sum_{j=1}^{N} c_j \underline{\boldsymbol{E}}^{(j)}(\boldsymbol{r}) \tag{2.73}$$

where $\underline{\boldsymbol{E}}^{(j)}(\boldsymbol{r})$ are expansion functions that have been chosen beforehand. In practice, the goal consists in bringing the variation of the functional as close to zero as possible, that is, to locate the stationary point of Eq. (2.72) as accurately as possible. How well this goal is reached depends on the test function employed and the expansion functions chosen. Finite element expansion functions are one possibility for this choice and will be discussed in Sec. 3.1.3.

[15] Note the absence of the $*$ (complex conjugate) in the inner product.

2.2.6 VCSEL Mode Designation

A labeling scheme analogous to the one for the step-index optical fibre [45] is commonly used to identify the optical modes that are relevant to the lasing operation of circularly symmetric VCSEL devices. Such a scheme will only cover a subset of all eigensolutions of Eq. (2.21) for a VCSEL cavity. Nevertheless, it will be employed throughout. Note that only circularly symmetric devices will be considered, although other structures, such as square devices, have been proposed.

The modes of circular waveguides with a PEC boundary can be divided into two sets: the TE_{mn} (transverse electric field) modes with $E_z = 0$ and $H_z \neq 0$, and the TM_{mn} (transverse magnetic field) modes with $H_z = 0$ and $E_z \neq 0$. The z axis is directed along the waveguide, index m is the azimuthal, and index n the radial mode order. The transversal fields in a cylindrical coordinate system $\underline{\boldsymbol{E}} = (E_r, E_\phi, E_z)^T$, $\underline{\boldsymbol{E}} = (H_r, H_\phi, H_z)^T$ are linked to the z components E_z and H_z as

$$E_r = -\frac{1}{n^2\omega^2/c_0^2 - k_z^2}\left(\frac{m\omega\mu_0}{r}H_z - ik_z\frac{\partial E_z}{\partial r}\right) \tag{2.74}$$

$$E_\phi = -\frac{1}{n^2\omega^2/c_0^2 - k_z^2}\left(i\omega\mu_0\frac{\partial H_z}{\partial r} + \frac{k_z m}{r}E_z\right) \tag{2.75}$$

$$H_r = \frac{1}{n^2\omega^2/c_0^2 - k_z^2}\left(\frac{mn^2\omega\varepsilon_0}{r}E_z + ik_z\frac{\partial H_z}{\partial r}\right) \tag{2.76}$$

$$H_\phi = \frac{1}{n^2\omega^2/c_0^2 - k_z^2}\left(in^2\omega\varepsilon_0\frac{\partial E_z}{\partial r} - \frac{k_z m}{r}H_z\right) \tag{2.77}$$

with the local refractive index n, angular frequency ω and propagation constant k_z.

For the step-index fibre, assuming an infinite external cladding region, only the modes for $m = 0$ with radial field patterns split into TE_{0n} and TM_{0n} modes. If $m \neq 0$, hybrid HE_{mn} and EH_{mn} modes result with both E_z and H_z non zero and two-fold degeneracy. The hybrid mode designation derives from the observation that for HE_{mn} modes the transversal fields according to Eqs. (2.74-2.77) are dominated by H_z and for EH_{mn} by E_z. HE_{11} is the fundamental mode of the circular step-index fibre since it propagates for all frequencies ω.

If the fibre is only weakly guiding, that is

$$\frac{1}{2}\frac{n_1^2 - n_2^2}{n_1^2} = \Delta \ll 1, \tag{2.78}$$

the hybrid modes can be re-expressed in terms of linearly polarised (LP_{mn}) modes according to the following rules:

- LP_{0n} is derived from an HE_{1n} mode
- LP_{1n} is derived from a TE_{0n}, TM_{0n}, and HE_{2n} mode
- LP_{mn} ($m \geq 2$) is derived from an $\mathrm{HE}_{(m+1)n}$ and an $\mathrm{EH}_{(m-1)n}$ mode.

Figure 2.12 shows a schematic representation of the correspondence between hybrid and LP modes in the weakly guiding approximation. Again, as for the hybrid modes, index m is the azimuthal and index n the radial mode order. The axial fields E_z and H_z are of the order Δ times the magnitude of the non-vanishing transverse field components. The approximate LP modes are therefore almost TEM waves for very small Δ. Depending on whether the sums or the differences of the hybrid modes are formed, two linearly polarised modes with orthogonal fields result. From the hybrid mode degeneracy a two-fold degeneracy for LP modes with $m = 0$ and a four-fold degeneracy for those with $m \neq 0$ follows.

From a mathematical point of view circularly symmetric structures provide no preferred direction for the polarisation of the LP or the underlying hybrid modes. From a physical point of view this symmetry is always broken by the non-circular symmetry of the material that is used to make a VCSEL device, and by imperfections of the circular VCSEL structure itself. If follows that practical VCSEL devices emit in two different polarisation states: a parallel and an orthogonal state. The directions relate to the crystallographic axes of the material [46].

In almost any application polarisation flips have to be prevented. That is, a change of lasing on one polarisation of a mode to the other polarisation. There are several methods that are used to pick the wanted polarisation direction and suppress the other: polarisation dependent gain medium and mis-oriented substrates to achieve a polarisation dependent modal gain, sub wavelength gratings on top of

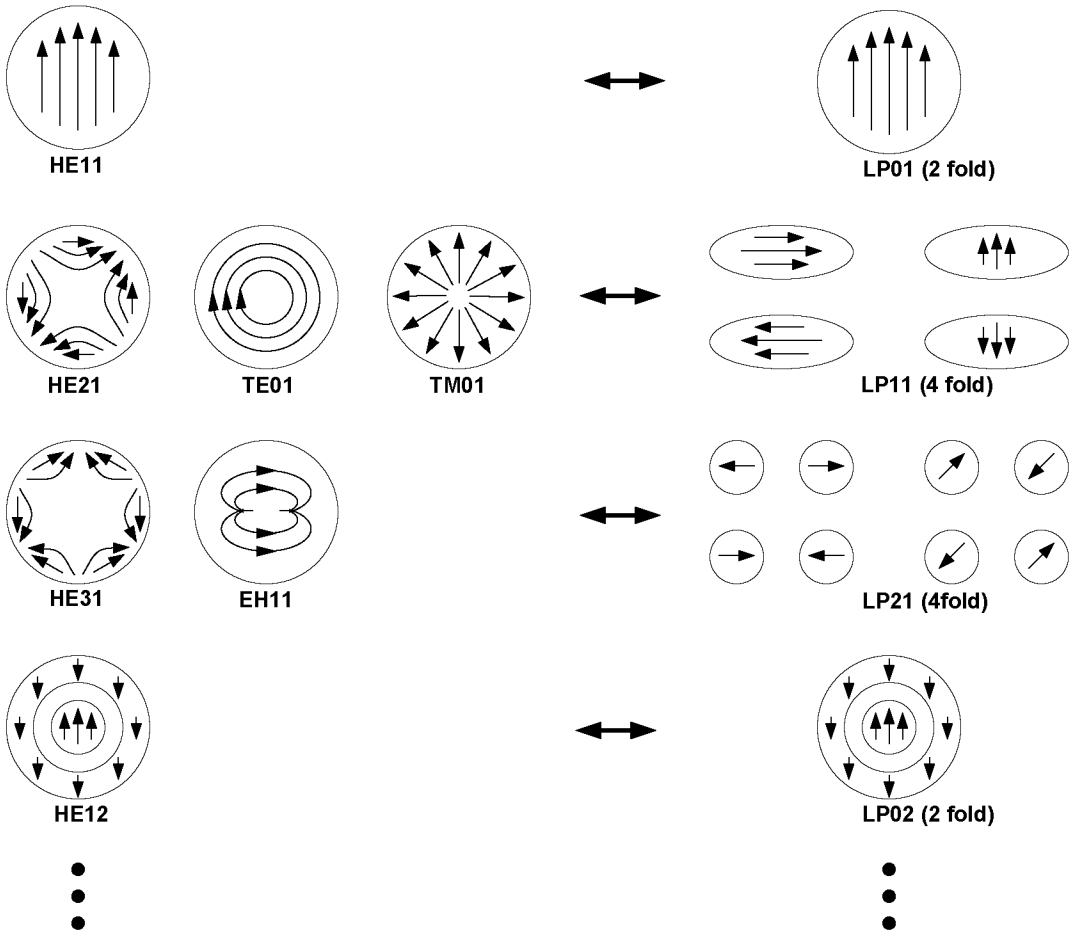

Figure 2.12: Schematic of correspondence between hybrid and LP modes in weakly guiding approximation. Arrows indicate direction of electric field.

the DBR to provide a polarisation dependent reflectivity; furthermore, strain induced birefringence [47], asymmetric mesa shapes and top metal contacts [46].

The model developed in this work assumes stable polarisation of the optical modes and no flips.

2.3 Electro-Thermal Transport Model

For the bulk electro-thermal carrier transport a thermodynamic model that accounts for self-heating is employed. A detailed description can be found in [29, 48, 49, 50]. Only a brief summary is given here. The main prerequisite of the model is the assumption of local thermal equilibrium between the charge carriers and the lattice. Optionally, it is possible to invoke a hydrodynamic model in case the lattice and the charge carriers are not in thermal equilibrium.

The basic equations of the thermodynamic model comprise the Poisson equation

$$\nabla \cdot (\varepsilon \nabla \phi) = -e \left(p - n + N_D^+ - N_A^- \right) \tag{2.79}$$

for the electrostatic potential, and the continuity equations for the electrons, holes and the local heat

$$\nabla \cdot \boldsymbol{j}_n = e \left(R + \frac{\partial}{\partial t} n \right) \tag{2.80}$$

$$-\nabla \cdot \boldsymbol{j}_p = e \left(R + \frac{\partial}{\partial t} p \right) \tag{2.81}$$

$$-\nabla \cdot \boldsymbol{S} = H + c_{th} \frac{\partial}{\partial t} T, \tag{2.82}$$

respectively. The electron and hole densities n and p, the lattice and carrier temperature T, and the electrostatic potential ϕ are the unknowns of this system of non-linear equations. The electron and hole current densities, and the conductive heat flow are denoted by $\boldsymbol{j}_n$, $\boldsymbol{j}_p$ and $\boldsymbol{S}$, respectively. All of these quantities are in fact functions of $\boldsymbol{r}$ and t, but the arguments will be omitted in the following to keep notation simple. Furthermore, N_D^+ and N_A^- are the ionised donor and

acceptor concentrations, e is the elementary charge, ε the electrical permittivity and c_{th} the total heat capacity of the semiconductor.

The net recombination rate R in the non-active bulk region is assumed equal to the radiative recombination rate due to spontaneous emission R^{sp} plus the non-radiative recombination rate composed of the Auger R^a and SRH R^{srh} rates [51]

$$R^{sp} = C_{sp}\left(np - n_i^2\right) \tag{2.83}$$

$$R^a = \left(C_n n + C_p p\right)\left(np - n_i^2\right) \tag{2.84}$$

$$R^{srh} = \frac{np - n_i^2}{\tau_p\left(n + n_i\right) + \tau_n\left(p + n_i\right)}. \tag{2.85}$$

The coefficients C_{sp}, τ_n, τ_p are the bulk spontaneous emission coefficient, and the minority carrier lifetimes for electrons and holes, respectively. The parameter n_i is the intrinsic carrier density. Since R^{sp} and R^{srh} are assumed to contribute only little to the total current when the VCSEL is in the lasing state C_{sp} is taken as a constant and τ_n, τ_p as dependent on the doping concentration only. The Auger coefficients assume a temperature dependence

$$C_n(T) = A_n + B_n^{(1)}\left(\frac{T}{T_0}\right) + B_n^{(2)}\left(\frac{T}{T_0}\right)^2 \tag{2.86}$$

$$C_p(T) = A_p + B_p^{(1)}\left(\frac{T}{T_0}\right) + B_p^{(2)}\left(\frac{T}{T_0}\right)^2 \tag{2.87}$$

with $T_0 = 300$ K [16]. The coefficients in Eqs. (2.83), (2.85) and (2.86) can vary strongly and often depend on device processing conditions. They are therefore regarded as fitting parameters in the following.

The net heat generation rate H is given by

$$H = \frac{\boldsymbol{j}_n \cdot \boldsymbol{j}_n}{en\mu_n} + \frac{\boldsymbol{j}_p \cdot \boldsymbol{j}_p}{ep\mu_p} + eR\left[\phi_p - \phi_n + T\left(P_p - P_n\right)\right] - \boldsymbol{j}_n \cdot T\nabla P_n - \boldsymbol{j}_p \cdot T\nabla P_p. \tag{2.88}$$

[16] Moreover, the temperature dependence of the Auger coefficients has been shown to exhibit an exponential characteristic with a threshold at a certain activation energy [52]. This behaviour is observed in long wavelength devices at 1300 and 1550 nm in particular.

The first two terms represent the electron and hole Joule heating rates where μ_n and μ_p are the electron and hole mobilities. The second term is the recombination heat with quasi Fermi potentials ϕ_n and ϕ_p for electrons and holes. The last term is the Thomson/Peltier heating rate. The absolute thermoelectric powers P_n and P_p are approximated by the analytical formulas for a non-degenerate semiconductor and parabolic energy bands

$$P_n = \frac{k_B}{e}\left(\log\frac{n}{N_c} - \frac{5}{2}\right) \tag{2.89}$$

$$P_p = \frac{k_B}{e}\left(-\log\frac{p}{N_v} + \frac{5}{2}\right) \tag{2.90}$$

with Boltzmann's constant k_B and the effective density of states N_c, N_v for the conduction and valence band.

To account for the high carrier densities Fermi-Dirac distribution functions are employed and hence

$$n = N_c F_{1/2}\left(\frac{-e\phi_n - \mathsf{E}_c}{k_B T}\right) \tag{2.91}$$

$$p = N_v F_{1/2}\left(\frac{\mathsf{E}_v + e\phi_p}{k_B T}\right) \tag{2.92}$$

applies, where $F_{1/2}$ are Fermi integrals of order one half. The conduction and valence bands E_c and E_v are defined as

$$\mathsf{E}_c = -\chi + \Delta\mathsf{E}_{g,c} - e\left(\phi - \phi_{ref}\right) \tag{2.93}$$

$$\mathsf{E}_v = -\chi - \mathsf{E}_g + \Delta\mathsf{E}_{g,v} - e\left(\phi - \phi_{ref}\right) \tag{2.94}$$

with electron affinity χ, band gap E_g, and band gap narrowing described by $\Delta\mathsf{E}_{g,c}$ and $\Delta\mathsf{E}_{g,v}$. The reference potential ϕ_{ref} is normally set to the Fermi potential of the intrinsic semiconductor. The quasi Fermi potentials are linked to the quasi Fermi levels by

$$\mathsf{E}_{F,n} = -e\phi_n \tag{2.95}$$

$$\mathsf{E}_{F,p} = -e\phi_p. \tag{2.96}$$

In the bulk region Eqs. (2.79-2.82) are completed by the flux equa-

tions for the charge carriers and the conductive heat

$$\boldsymbol{j}_n = -en\mu_n \left(\nabla\phi_n + P_n\nabla T\right) \tag{2.97}$$

$$\boldsymbol{j}_p = -ep\mu_p \left(\nabla\phi_p + P_p\nabla T\right) \tag{2.98}$$

$$\boldsymbol{S} = -\kappa_{th}\nabla T \tag{2.99}$$

with the total thermal conductivity κ_{th} of the semiconductor.

The effect of the Peltier heat generated at the anode and cathode contacts is assumed negligible with respect to the remaining heat sources.

2.4 Carrier Transport at Heterointerfaces and Quantum Wells

Heterointerfaces can be modeled using a thermionic emission model [53]. However, the carrier transport in the DBR of a VCSEL structure (Fig. 1.3) is rendered by transport through a homogeneous region, except for the DBR layers closest to the λ cavity. The homogeneous region is assigned an effective conductivity for heat, electrons and holes, and an effective heat capacity.

This is justified by the fact that the forward biased doped heterointerfaces graded over 20 nm merely introduce an additional series resistance due to a small potential barrier formed by a space charge region caused by majority carrier diffusion from the wide band gap to the lower band gap material as shown in Fig. 2.13. Furthermore, the net carrier recombination rate in the DBR away from the λ cavity is comparatively low. Figure 2.13 shows that the minority carrier density reaches thermal equilibrium very quickly moving away from the λ cavity into the DBR. Hence, the net Peltier/Thomson effect will also be low in a region where one wide and one narrow band gap material are alternated in a periodic fashion, as is the case in an AlGaAs DBR stack.

However, to appropriately account for the carrier injection from the DBR region into the λ cavity the first one or two periods of the DBR periods have to be included in the electro-thermal model. The key advantage substituting the DBR stack with a homogeneous material is the reduced computational effort in solving the electro-thermal

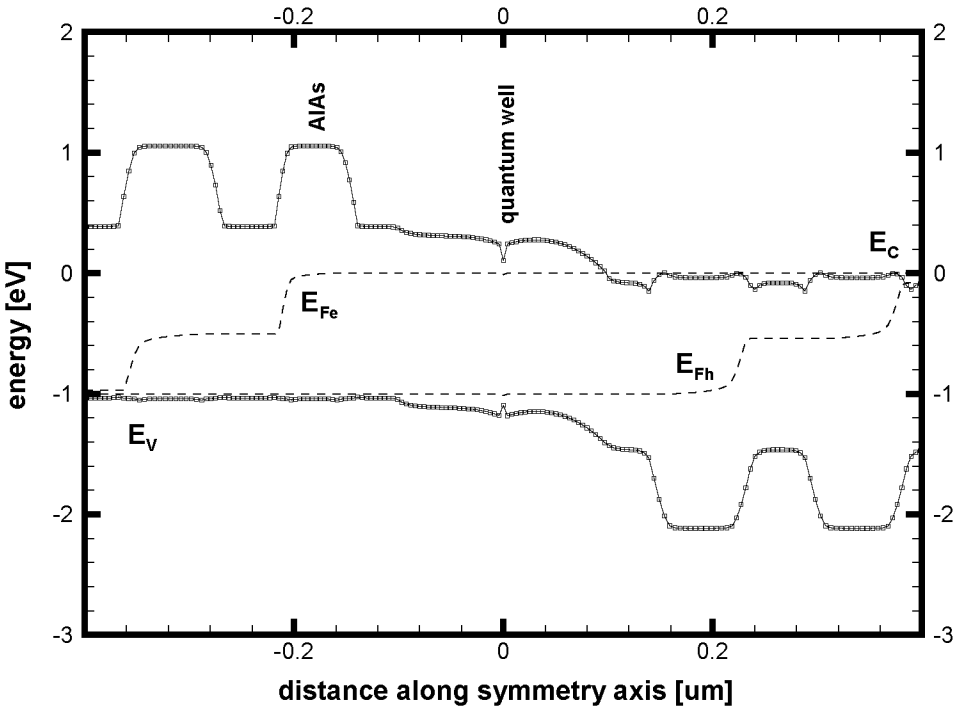

Figure 2.13: Cut of energy band diagram along symmetry axis of VCSEL device structure for a forward bias of 1.0 V. Conduction and valence bands, and quasi Fermi energies for electrons and holes are shown. Peaks in conduction band on n-doped side and valence band on p-doped side are caused by majority carrier diffusion from wide band gap to low band gap material.

system of equations in the 2D finite element formulation that is envisaged here. The effective parameters of the homogeneous material can easily be determined in a 1D simulation taking all heterointerfaces into account, or be derived from measurements.

Abrupt heterointerfaces are modeled using a thermionic emission model [23, 53]. The model provides current density equations perpendicular to the interface. Graded heterointerfaces are covered by the thermodynamic model described in Sec. 2.3.

Quantum wells are treated as ballistic transport scattering centres for carriers [17, 23, 54, 55]. This yields current density equations perpendicular to the edges of the quantum wells, and, additionally, capture and escape rate equations for the scattered carriers. In the quantum well the carrier densities bound to a quantum well n^{2D}, p^{2D}

are connected to the mobile carrier densities n, p "above" the quantum well via a net carrier capture rate given by

$$C^{cap} = \left(1 - e^{\frac{e\left(\phi_n^{2D} - \phi_n\right)}{k_B T}}\right)\left(1 - \frac{n^{2D}}{N^{2D}}\right)\frac{n^{3D}}{\tau_e} \tag{2.100}$$

for the electrons and similarly for the holes with the electron quasi Fermi potentials ϕ_n and ϕ_n^{2D} for the mobile and bound electrons, respectively. The parameter N^{2D} is the sum of all quantum well states per unit volume, and τ_e is an effective electron scattering time. Equation (2.100) holds as long as ϕ_n^{2D} and ϕ_p^{2D} remain below the band edge of the barrier.

In the quantum well region the continuity equation (2.80) is replaced by the following set of equations

$$\nabla \cdot \boldsymbol{j}_n = e\left(R + C^{cap} + \frac{\partial}{\partial t} n\right) \tag{2.101}$$

$$\nabla \cdot \boldsymbol{j}_n^{2D} = e\left(R^{nr} + R^{sp} + R^{st} - C^{cap} + \frac{\partial}{\partial t} n^{2D}\right) \tag{2.102}$$

for the electrons and equally for the holes. The quantum well regions correspond to the active region of the device. Therefore, the net recombination rate consists of stimulated radiative recombination and optical generation R^{st}, spontaneous radiative recombination R^{sp}, and non-radiative recombination (Auger and SRH) R^{nr}. For the latter the heat generated by the recombination processes is taken into account as part of H in Eq. (2.82). Equation (2.102) together with current equations similar to Eqs. (2.97) and (2.98), using the appropriate parameters for lateral current flow, describe carrier transport in the quantum well plane. For the Poisson equation (2.79) the electron and hole densities n and p are equal to the sum of mobile and bound electrons n^{2D} and holes p^{2D}.

The local carrier recombination / generation rate per unit volume due to stimulated emission / optical absorption in the active region

comprising all N modes is [23, 26]

$$R^{st}(\boldsymbol{r}) = \sum_{k=1}^{N} \frac{\nabla \cdot \boldsymbol{S}_k(\boldsymbol{r})}{\iiint_V w_k(\boldsymbol{r})\, dV} S_k$$
$$= \sum_{k=1}^{N} \frac{-\mathrm{Im}\left[\omega_k' \underline{\boldsymbol{E}}_k(\boldsymbol{r}) \cdot \varepsilon_r(\boldsymbol{r}, \omega_k') \cdot \underline{\boldsymbol{E}}_k^*(\boldsymbol{r})\right]}{\frac{1}{2}\mathrm{Re}\left[\iiint_V \underline{\boldsymbol{E}}_k(\boldsymbol{r}) \cdot \varepsilon_r(\boldsymbol{r}, \omega_k') \cdot \underline{\boldsymbol{E}}_k^*(\boldsymbol{r})\, dV\right]} S_k \quad \left[\mathrm{s}^{-1}\mathrm{cm}^{-3}\right] \tag{2.103}$$

according to Sec. 2.2.4 for a scalar $\varepsilon_r(\boldsymbol{r})$ neglecting the contribution of the magnetic field. The local relative generation / dissipation rate is evaluated with respect to the optical energy contained in mode k [17].

The local recombination due to spontaneous emission in the active region is given by integrating Eq. (2.16) over energy space

$$R^{sp}(\boldsymbol{r}) = \int_0^\infty r^{sp}(\boldsymbol{r}, E) dE \quad \left[\mathrm{s}^{-1}\mathrm{cm}^{-3}\right]. \tag{2.104}$$

The quasi Fermi potentials ϕ_n^{2D} and ϕ_p^{2D} govern the occupation of the combined states of all conduction sub-bands or valence sub-bands, respectively. The assumption of Fermi distributions is not valid in general. It breaks down, for instance, in the case of strong spectral hole burning in which carriers are distributed in energy space according to a non-equilibrium distribution. Nevertheless, in the case of VCSELs, intensities are normally not sufficiently high to burn spectral holes in the carrier distribution of the active region. According to [18] it is more important to take into account a carrier temperature T_p for the electron-hole plasma separate from the lattice temperature at high modulation frequencies. Carrier phonon scattering is then no

[17] The unit in which this energy is counted is immaterial here, but it is determined by the choice of the unit for $R_k^{sp}(t)$ in Eq. (2.8). In this work $R_k^{sp}(t)$ is a photon rate and given in s^{-1}. Hence, S_k corresponds to the number of photons in mode k. Alternatively, by multiplying $R_k^{sp}(t)$ with the photon energy $\hbar\omega_k'$ in Joules the variable S_k would correspond to the electromagnetic energy in mode k in SI units.

longer sufficiently effective to cool the carriers that are approximately Fermi distributed at a temperature T_p down to a Fermi distribution at lattice temperature T_l. This leads to an additional damping of the modulation response of the device.

Chapter 3

Simulator Implementation

The VCSEL simulator was implemented in the DESSIS device simulator [23, 29, 48, 49, 56]. The LUMI mode solver library was developed as an extension in order to handle the optical problem presented in Sec. 2.2. The mode solver library can be used stand-alone via a Tcl [57] scripting interface or coupled to the DESSIS device simulator. When used in the latter configuration the electro-thermal and optical equations can be solved self-consistently by an iteration scheme (Sec. 3.3.3). Static, small signal modulation, and large signal transient responses of the VCSEL device can be computed with the simulator.

The simulator assumes a rotationally symmetric VCSEL device structure that is discretised with 2D finite elements in the cross-section perpendicular to the wafer surface as shown in Fig. 1.3. In principle, one could use 3D finite elements to even compute rotationally non-symmetric devices. However, a full 3D formulation is not feasible with the computational resources presently available.

The complexity of the electro-thermal device equations does not permit a 2D finite element discretisation of the individual DBR heterointerfaces. Instead, the DBRs are represented as homogeneous regions with effective material parameters, except for the DBR layers closest to the λ cavity. In contrast, due to the long-ranging wave

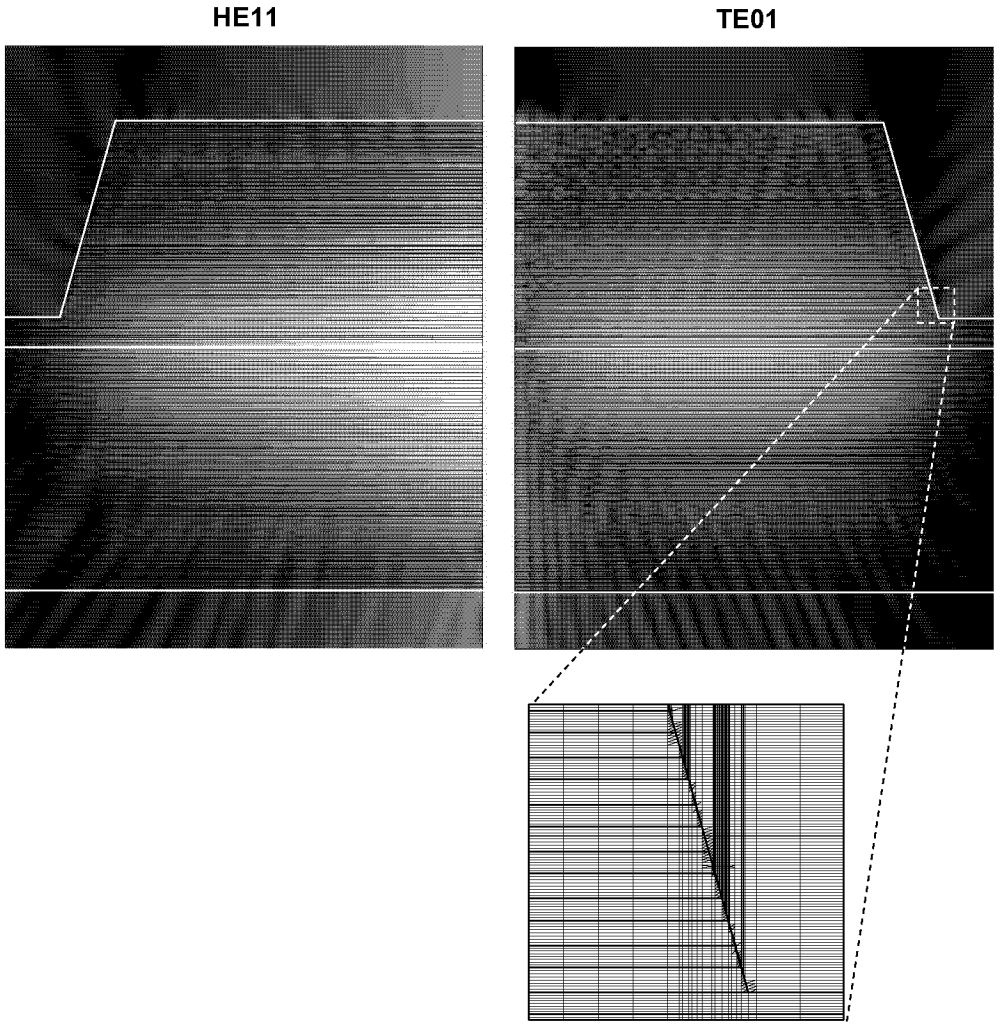

Figure 3.1: Normalised optical intensity of fundamental HE11 and first order TE01 modes on logarithmic grey scale. Inset shows portion of the mesh used to discretise the optical problem. The VCSEL structure has an intra cavity contact and an oxide aperture with r_{ox} = 1 μm at a field node position.

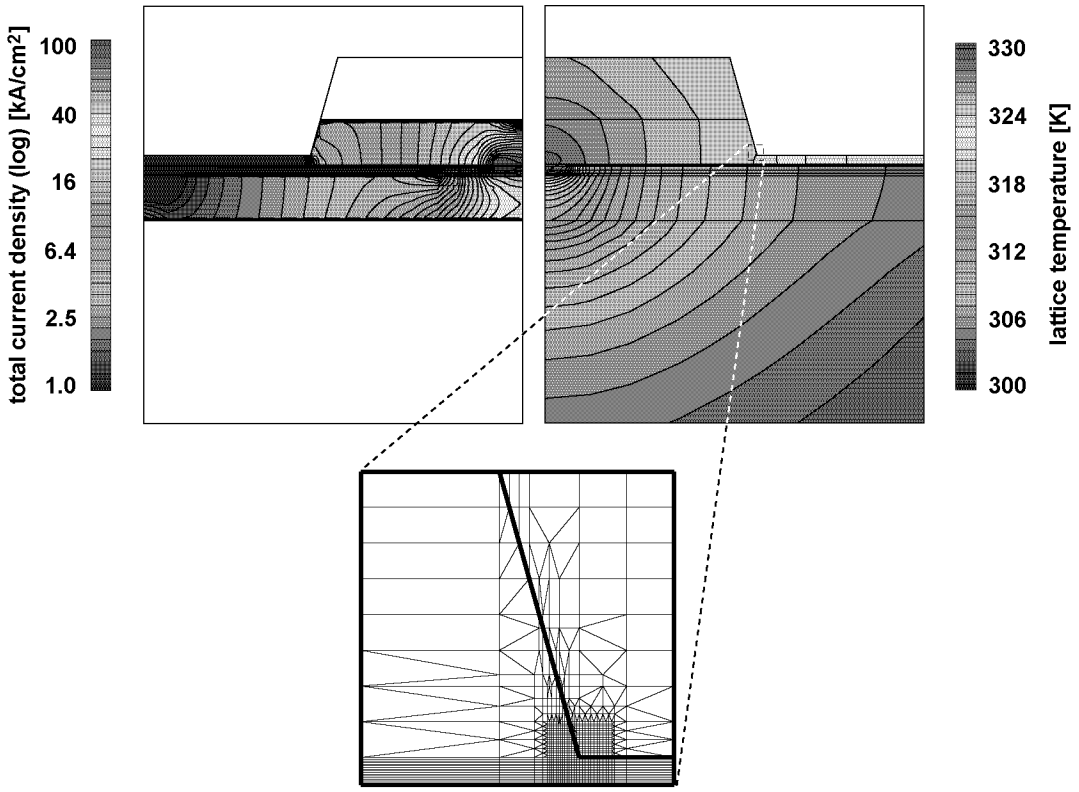

Figure 3.2: Total current density distribution on logarithmic colour scale and lattice temperature profile lattice temperature distribution on linear colour scale. Terminal current is 5.3 mA and output power 1.3 mW. Inset shows portion of mesh used to discretise the electro-thermal problem. The VCSEL structure has an intra cavity contact and an oxide aperture with $r_{ox} = 1$ μm at a field node position.

nature of the electromagnetic radiation in the VCSEL resonator, the DBR heterointerfaces have to be resolved for the optical problem. Consequently, two separate meshes are used. A coarser one for the electro-thermal problem and a finer one for the optical problem. Linear interpolation translates variables between the two meshes. The insets in Figs. 3.1 and 3.2 show representative examples of meshes used for the optical and electro-thermal problem, respectively, for a VCSEL structure with an intra cavity contact.

In order to adapt the size of the computational problems to the individual physical problems the simulation is decomposed into three domains shown in Figs. 3.1 and 3.2. The largest area is covered by

the thermal domain shown on the right of Fig. 3.2 where only the thermal equations are solved. This ensures that the contacts to the thermal bath held at the ambient temperature can be kept sufficiently remote from the core VCSEL device. The influence of the thermal contacts on the temperature distribution in the VCSEL device can be reduced in this way. The area shown on the left in Fig. 3.2 defines the extent of the electro-thermal domain, where in addition to the thermal equations, the electronic equations are solved (Sec. 3.2). This domain is deliberately chosen smaller to reduce the memory requirement and run-time of the computational problem. Figure 3.1 shows the extent of the optical domain where the optical equations are solved (Sec. 3.1).

3.1 Maxwell Wave Equation

Various methods of computing the optical modes of VCSEL devices were proposed in the past [24, 58] – [72]. Only some of them [24, 63, 67, 69] can take into account a general form of an arbitrary, non-uniform dielectric function (2.19) and are potentially suitable to integrate self-consistently with a laser simulator. Other methods are computationally less demanding but assume idealised dielectric functions and neglect effects of continuous temperature, carrier, optical gain and loss distributions, and the detailed geometry of the optical cavity.

A promising approach is described in [63]. The beam propagation method (BPM) is combined with the discrete Bessel transform (DBT). Laterally homogeneous regions are represented by transfer matrices in a Fourier-Bessel form, and laterally inhomogeneous layers are treated using BPM. The method is efficient as long as only a small proportion of all regions has to be treated using BPM, as the method becomes too computationally intensive otherwise.

In [24] a Green's function formalism is used. For a general VCSEL structure the computation of the Green's functions and the solution of the resulting dense eigenvalue problem becomes prohibitive in computational complexity, especially, if they have to be re-evaluated over the operation range of the VCSEL device.

A layer-wise expansion into a discrete set of vectorial modes and mode-matching at the layer interfaces is employed in [69]. As sam-

pling along an interface is less costly than over a region this can be an effective approach. However, the finer the vertical discretisation into layers and the more terms in the discrete set of modes the more time consuming this method will become. In principle, the former method can be extended to handle an arbitrary subdivision of the device structure in the lateral direction: a multiple cylindrical shell problem. It is clear that at a certain number of subdivisions there will no longer be an advantage of sampling the problem along the region interfaces compared to sampling it over the region. At this point, the tasks reduces to selecting suitable expansion functions for the regions.

Finite element expansion functions are a possible choice. Because they are simple to compute they can be used for structures subdivided into a large number of regions. That is, to use an element expansion per region which is then equivalent to an element of a mesh. In addition, by using the variational method they yield sparse matrix numerical problems that can be solved efficiently by standard numerical methods. Furthermore, the finite element formulation of the problem can be tuned by changing the order of the expansion functions. In this way the number of elements can be traded for the sparsity of the matrix problem for a given accuracy of the result.

The finite element approach employed in this work is related to [65, 67]. With this approach, in principle, optical modes for arbitrary VCSEL geometries can be computed. Up to now the finite element approach has always fallen short of handling problems that occur as soon as realistic VCSEL devices are considered. How this limitation is overcome by a finite element approach and its efficient solution using the iterative Jacobi-Davidson [73, 74] algorithm is demonstrated here. This section deals with the finite element formulation of Eqs. 2.20 and 2.21 for realistic, circularly symmetric VCSEL structures.

3.1.1 Permittivity and Permeability Functions

According to Sec. 2.2 the optical field in a VCSEL structure is obtained by solving Maxwell's wave equation in the frequency domain subject to a radiation condition

$$\nabla \times \Lambda^{-1}(\boldsymbol{r}) \cdot (\nabla \times \underline{\boldsymbol{E}}(\boldsymbol{r})) - \frac{\omega^2}{c_0^2} \Lambda(\boldsymbol{r}) \varepsilon_r(\boldsymbol{r}) \cdot \underline{\boldsymbol{E}}(\boldsymbol{r}) = \underline{\boldsymbol{F}}(\boldsymbol{r}, \omega) \qquad (3.1)$$

with

$$\varepsilon_r(\boldsymbol{r},\omega) = \varepsilon_r'(\boldsymbol{r},\omega) + i\varepsilon_r''(\boldsymbol{r},\omega). \tag{3.2}$$

The tensor function $\Lambda(\boldsymbol{r})$ [75] is given by

$$\Lambda(\boldsymbol{r}) = \begin{bmatrix} \frac{s_y(\boldsymbol{r})s_z(\boldsymbol{r})}{s_x(\boldsymbol{r})} & 0 & 0 \\ 0 & \frac{s_z(\boldsymbol{r})s_x(\boldsymbol{r})}{s_y(\boldsymbol{r})} & 0 \\ 0 & 0 & \frac{s_x(\boldsymbol{r})s_y(\boldsymbol{r})}{s_z(\boldsymbol{r})} \end{bmatrix} \tag{3.3}$$

for the Cartesian coordinate system using $s_x(\boldsymbol{r})$, $s_y(\boldsymbol{r})$, and $s_z(\boldsymbol{r})$ as prescribed in Fig. 2.5. The tensor $\Lambda(\boldsymbol{r})$ represents the operator ∇_s (Eq. 2.34) in terms of a material with anisotropic permittivity and permeability. The advantage of this approach is that the standard ∇ operator can be used for the formulation of the problem. The equivalence of the two representations can immediately be verified by comparing Eqs. (2.30–2.33) and

$$\nabla \times \underline{\boldsymbol{E}}^a(\boldsymbol{r}) = i\omega\mu_0\mu_r\Lambda(\boldsymbol{r}) \cdot \underline{\boldsymbol{H}}^a(\boldsymbol{r}) \tag{3.4}$$

$$\nabla \times \underline{\boldsymbol{H}}^a(\boldsymbol{r}) = -i\omega\varepsilon_0\varepsilon_r\Lambda(\boldsymbol{r}) \cdot \underline{\boldsymbol{E}}^a(\boldsymbol{r}) \tag{3.5}$$

$$\nabla \cdot (\varepsilon_0\varepsilon_r\Lambda(\boldsymbol{r}) \cdot \underline{\boldsymbol{E}}^a(\boldsymbol{r})) = 0 \tag{3.6}$$

$$\nabla \cdot (\mu_0\mu_r\Lambda(\boldsymbol{r}) \cdot \underline{\boldsymbol{H}}^a(\boldsymbol{r})) = 0. \tag{3.7}$$

The fields in Eqs. (2.30–2.33) and Eqs. (3.4–3.7) are related according to $E_\eta^a(\boldsymbol{r}) = s_\eta(\boldsymbol{r})E_\eta(\boldsymbol{r})$ and $H_\eta^a(\boldsymbol{r}) = s_\eta(\boldsymbol{r})H_\eta(\boldsymbol{r})$ with $\eta = x, y, z$.

For the complex refractive index $n(\boldsymbol{r})+i\kappa(\boldsymbol{r})$ the dielectric function reads

$$\varepsilon_r(\boldsymbol{r},\omega) = \left(n^2(\boldsymbol{r},\omega) - \kappa^2(\boldsymbol{r},\omega)\right) + i\,2n(\boldsymbol{r},\omega)\kappa(\boldsymbol{r},\omega). \tag{3.8}$$

Due to causality the real and imaginary part $\varepsilon_r'(\boldsymbol{r},\omega)$ and $\varepsilon_r''(\boldsymbol{r},\omega)$ of Eq. (3.2) are inter-related by the Kramers-Kronig relation [26]. The refractive index is assumed linearly temperature dependent according to

$$n(\boldsymbol{r},\omega,T) = n_0(\boldsymbol{r},\omega)\ (1 + \alpha_n(\boldsymbol{r},\omega)\ (T - T_0)) \tag{3.9}$$

with a temperature coefficient $\alpha_n(\boldsymbol{r},\omega)$. Equation (3.8) together with (3.9) is used to cover the following processes[1]

[1] An extensive review of the dielectric functions and their dependence on temperature, doping and extrinsic carrier density for some material systems can be found in [76] and [77]

- direct and indirect interband absorption near the band edge (for non active regions)
- free-carrier absorption (particularly severe for long wavelength 1300 nm and 1550 nm VCSEL devices)
- interconduction band and intervalence band absorption
- absorption in metallic regions

everywhere except in the active region, where the dielectric function reads

$$\varepsilon_r(\boldsymbol{r},\omega) = \left(n(\boldsymbol{r},\omega)^2 - \frac{c_0^2}{4\omega^2}\alpha(\boldsymbol{r},\omega)^2\right) + i\frac{n(\boldsymbol{r},\omega)c_0}{\omega}\alpha(\boldsymbol{r},\omega) \qquad (3.10)$$

with loss / gain $\alpha(\boldsymbol{r},\omega)$ given in Eq. (2.14) due to local interband absorption / stimulated emission.

The source term $\underline{\boldsymbol{F}}(\boldsymbol{r},\omega)$ in Eq. (3.1) is used to represent fluctuations due to spontaneous emission in the active region.

3.1.2 BOR Variational Functional

A Body Of Revolution (BOR) variational functional for rotationally symmetric device structures is presented. Maxwell's vectorial wave equation Eq. (2.20), subject to the radiation condition imposed by PML in the form of an anisotropic material $\Lambda(\boldsymbol{r})$ according to Eqs. (3.4–3.7) with complex scalar relative permittivity $\varepsilon_r(\boldsymbol{r})$ and permeability $\mu_r \equiv 1$, is given by Eq. (3.1). The corresponding variational functional according to Eq. (2.72) reads

$$\begin{aligned} F(\underline{\boldsymbol{E}}) =& \frac{1}{2}\iint_O \int_0^{2\pi} \left[(\nabla\times\underline{\boldsymbol{E}})\cdot\Lambda^{-1}\cdot(\nabla\times\underline{\boldsymbol{E}}) - \frac{\omega^2}{c_0^2}\underline{\boldsymbol{E}}\cdot\varepsilon_r\Lambda\cdot\underline{\boldsymbol{E}}\right]\rho\,d\phi\,d\rho\,dz \\ & - \iint_O \int_0^{2\pi} \underline{\boldsymbol{E}}\cdot\underline{\boldsymbol{F}}(\omega)\rho\,d\phi\,d\rho\,dz \end{aligned} \qquad (3.11)$$

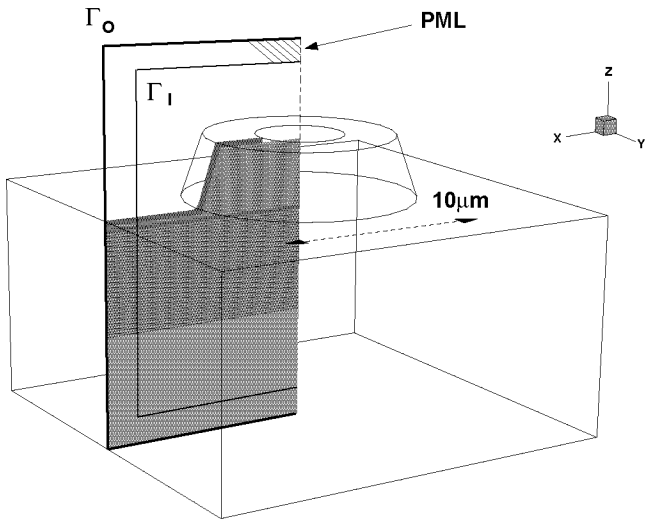

Figure 3.3: VCSEL device structure for simulation. The contours of the boundaries Γ_I and Γ_O are shown on a cross-section of the device.

in cylindrical coordinates with the dependence of $\underline{\boldsymbol{E}}$ and $\underline{\boldsymbol{F}}$ on ρ, ϕ and z omitted for clarity. The VCSEL cavity is enclosed by an inner boundary Γ_I (Fig. 3.3). Outside this boundary electro-magnetic waves are only outgoing due to the PML. Since the waves will be extinct by the PML when they reach the outer boundary Γ_O it can be used to truncate the computational problem. Integration is over the cylindrical volume V. Its cross section O in cylindrical coordinates is bounded by Γ_O. Homogeneous Dirichlet (PEC) and von Neumann (PMC) boundary conditions are applied on Γ_O. PMC are natural boundary conditions. PEC are essential boundary conditions and have to be imposed.

Since the VCSEL device structure is assumed rotationally symmetric, a Fourier series in ϕ, shown in Fig. 3.4, is used to expand $\underline{\boldsymbol{E}}$ in Eq. (3.11).

The field $\underline{\boldsymbol{E}}$ can be split with respect to the ρ-z plane for $\phi = 0$ into a symmetric part

$$\begin{aligned}\underline{\boldsymbol{E}}_s(\rho,\phi,z) =& \underline{\boldsymbol{E}}_{T,0}(\rho,z) \\ &+ \sum_{m=1}^{\infty} \left[\underline{\boldsymbol{E}}_{T,m}(\rho,z)\cos m\phi + E_{\phi,m}(\rho,z)\mathbf{e}_\phi \sin m\phi\right]\end{aligned} \tag{3.12}$$

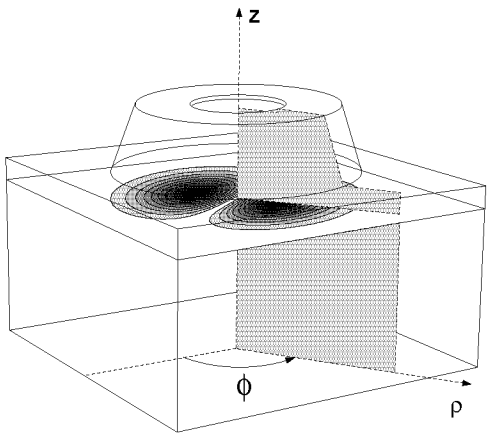

Figure 3.4: Fourier series expansion in ϕ (BOR)

and an asymmetric part

$$\underline{\boldsymbol{E}}_a(\rho,\phi,z) = E_{\phi,0}(\rho,z)\mathbf{e}_\phi + \sum_{m=1}^{\infty}\left[\underline{\boldsymbol{E}}_{T,-m}(\rho,z)\sin m\phi + E_{\phi,-m}(\rho,z)\mathbf{e}_\phi\cos m\phi\right] \tag{3.13}$$

where $\underline{\boldsymbol{E}}_{T,m}(\rho,z) = [E_{\rho,m}(\rho,z), 0, E_{z,m}(\rho,z)]^T$ is the in-plane and $E_{\phi,m}(\rho,z)$ the out of plane component of the vector $\underline{\boldsymbol{E}}(\rho,\phi,z)$.

Inserting the expansion $\underline{\boldsymbol{E}}(\rho,\phi,z) = \underline{\boldsymbol{E}}_s(\rho,\phi,z) + \underline{\boldsymbol{E}}_a(\rho,\phi,z)$ into the variational functional and taking the first variation gives

$$F(\underline{\boldsymbol{E}}) = F(\underline{\boldsymbol{E}}_s + \underline{\boldsymbol{E}}_a) \tag{3.14}$$

$$\frac{\delta F}{\delta \underline{\boldsymbol{E}}} = \frac{\delta F}{\delta \underline{\boldsymbol{E}}}\underbrace{\frac{\delta \underline{\boldsymbol{E}}}{\delta \underline{\boldsymbol{E}}_s}}_{1}\bigg|_{\underline{\boldsymbol{E}}_a} + \frac{\delta F}{\delta \underline{\boldsymbol{E}}}\underbrace{\frac{\delta \underline{\boldsymbol{E}}}{\delta \underline{\boldsymbol{E}}_a}}_{1}\bigg|_{\underline{\boldsymbol{E}}_s} = 0 \tag{3.15}$$

and similarly if $\underline{\boldsymbol{E}}$ is expanded like the series shown in Eqs. (3.12) and (3.13). Hence, due to the linearity of the sum in the expansion, finding the stationary point with respect to $\underline{\boldsymbol{E}}$ is equivalent to finding the stationary point with respect to each term in the expansion. Furthermore, when multiplying the terms of the expansion in Eqs. (3.12) and (3.13) to evaluate the variational functional, only products containing $\sin^2 m\phi$ and $\cos^2 m\phi$ or products constant in ϕ yield contributions in

the integration for ϕ from 0 to 2π. That is, all cross products vanish. It follows that the variational problem in $F(\underline{\boldsymbol{E}})$ can be treated by solving a series of variational problems $F_m(\underline{\boldsymbol{E}}_m)$, each one corresponding to a term of the expansion.

Note that decoupling $F(\underline{\boldsymbol{E}})$ into independent problems $F_m(\underline{\boldsymbol{E}}_m)$ is only possible if the functions ε_r, Λ and $\underline{\boldsymbol{F}}(\omega)$ can be separated into two components: one with a radial and the other with an azimuthal dependence. Only then will the cross products of terms in the expansion vanish. Otherwise, there will be coupling between the terms. The decoupling property is the requirement that the 3D VCSEL problem can be solved as a set of 2D problems[2].

Since the field must be continuous on the axis of the circularly symmetric structure, certain properties follow for the coefficients of the expansion along the z axis. They are easily deduced from symmetry considerations evident from Fig. 2.12:

- $m = 0 \Longrightarrow E_{\rho,0}(0,z) = 0$ and $E_{\phi,0}(0,z) = 0$
- $m = 1 \Longrightarrow E_{z,0}(0,z) = 0$
- $m > 1 \Longrightarrow E_{\rho,0}(0,z) = 0$, $E_{\phi,0}(0,z) = 0$ and $E_{z,0}(0,z) = 0$

Inserting the 0th term of the asymmetric expansion Eq. (3.13) and its curl into Eq. (3.11), and integrating ϕ from 0 to 2π yields

$$
\begin{aligned}
&F(\underline{\boldsymbol{E}}_{a,0}) = \\
&\pi \iint\limits_{O} \left(\nabla_T E_{a,\phi,0} + \frac{1}{\rho} \mathbf{e}_\rho E_{a,\phi,0} \right) \cdot \Lambda_T'^{-1} \cdot \left(\nabla_T E_{a,\phi,0} + \frac{1}{\rho} \mathbf{e}_\rho E_{a,\phi,0} \right) \rho \\
&- \frac{\omega^2}{c_0^2} \varepsilon_r \Lambda_\phi E_{a,\phi,0} E_{a,\phi,0} \rho \, d\rho \, dz \\
&- 2\pi \iint\limits_{O} E_{a,\phi,0} F_{a,\phi,0}(\omega) \rho \, d\rho \, dz,
\end{aligned}
\tag{3.16}
$$

[2]Given the computational resources mentioned at the beginning of Ch. 3 the decoupling property is a necessary requirement to obtain numerical problems of manageable size.

inserting the 0th term of the symmetric expansion Eq. (3.12)

$$\begin{aligned} F(\underline{\boldsymbol{E}}_{s,0}) = \pi &\iint\limits_O \frac{1}{\Lambda_\phi} \left(\nabla_T \times \underline{\boldsymbol{E}}_{s,T,0}\right) \left(\nabla_T \times \underline{\boldsymbol{E}}_{s,T,0}\right) \\ &- \frac{\omega^2}{c_0^2} \varepsilon_r \underline{\boldsymbol{E}}_{s,T,0} \cdot \Lambda_T \cdot \underline{\boldsymbol{E}}_{s,T,0} \rho \, d\rho \, dz \\ &- 2\pi \iint\limits_O \underline{\boldsymbol{E}}_{s,T,0} \cdot \underline{\boldsymbol{F}}_{s,T,0}(\omega) \, d\rho \, dz, \end{aligned} \tag{3.17}$$

and inserting the mth term with $m \geq 1$ of the symmetric expansion Eq. (3.12)

$$\begin{aligned} F(\underline{\boldsymbol{E}}_{s,m}) = \pi &\iint\limits_O \Bigg[\frac{1}{\Lambda_\phi} \left(\nabla_T \times \underline{\boldsymbol{E}}_{s,T,m}\right) \left(\nabla_T \times \underline{\boldsymbol{E}}_{s,T,m}\right) \\ &+ \left(\nabla_T E_{s,\phi,m} + \frac{m}{\rho} \underline{\boldsymbol{E}}_{s,T,m} + \frac{1}{\rho} \mathbf{e}_\rho E_{s,\phi,m} \right) \cdot \Lambda_T'^{-1} \\ &\cdot \left(\nabla_T E_{s,\phi,m} + \frac{m}{\rho} \underline{\boldsymbol{E}}_{s,T,m} + \frac{1}{\rho} \mathbf{e}_\rho E_{s,\phi,m} \right) \Bigg] \rho \\ &- \frac{\omega_k^2}{c_0^2} \varepsilon_r \left[\underline{\boldsymbol{E}}_{s,T,m} \cdot \Lambda_T \cdot \underline{\boldsymbol{E}}_{s,T,m} + \Lambda_\phi E_{s,\phi,m} E_{s,\phi,m} \right] \rho \, d\rho \, dz \\ &- 2\pi \iint\limits_O \underline{\boldsymbol{E}}_{s,T,m} \cdot \underline{\boldsymbol{F}}_{s,T,m} + E_{s,\phi,m} F_{s,\phi,m} \rho \, d\rho \, dz, \end{aligned} \tag{3.18}$$

with ∇_T defined as

$$\nabla_T = \frac{\partial}{\partial_\rho} \mathbf{e}_\rho + \frac{\partial}{\partial_z} \mathbf{e}_z. \tag{3.19}$$

The diagonal tensors Λ, Λ_T and Λ_T' read

$$\Lambda = \begin{bmatrix} \Lambda_\rho & 0 & 0 \\ 0 & \Lambda_\phi & 0 \\ 0 & 0 & \Lambda_z \end{bmatrix} \quad \Lambda_T = \begin{bmatrix} \Lambda_\rho & 0 & 0 \\ 0 & 0 & 0 \\ 0 & 0 & \Lambda_z \end{bmatrix} \quad \Lambda_T' = \begin{bmatrix} \Lambda_z & 0 & 0 \\ 0 & 0 & 0 \\ 0 & 0 & \Lambda_\rho \end{bmatrix} \tag{3.20}$$

for cylindrical coordinates. The entries for Λ_ρ, Λ_ϕ and Λ_z are given in App. B.

It is evident from Eqs. (3.16) and (3.17) that the variational functional decouples into two problems for $m = 0$. Functional Eq. (3.16) in $E_{a,\phi,0}$ will give solutions that correspond to the TE_{mn} modes, and Eq. (3.17) in $\underline{\boldsymbol{E}}_{s,T,0}$ solutions that correspond to the TM_{mn} modes. In Eq. (3.18), for $m \geq 1$, the components of the field $\underline{\boldsymbol{E}}_{s,T,0}$ remain coupled. Hence, the solutions will be the HE_{mn} and EH_{mn} modes of the cavity. The asymmetric counterpart of Eq. (3.18) will yield the same HE_{mn} and EH_{mn} modes, but rotated by 90 degrees in azimuthal direction. This corresponds to the two polarisation directions pointed out in Sec. 2.2.6.

Some of the integrals in Eqs. (3.16–3.18) contain a factor with a $1/\rho$ dependence. What seems unbounded for $\rho \to 0$ at first sight turns out to be bounded if the continuity conditions for the field on the symmetry axis of the structure are observed. The $1/\rho$ behaviour still poses a problem if the integrals have to be evaluated numerically close to the symmetry axis, as this leads to very large numerical values and cancellation effects. The $1/\rho$ behaviour can be removed by introducing a variable substitution [78, 79, 80] for Eq. (3.16) $m = 0$

$$\frac{1}{\rho} E_{a,\phi,m} \leftarrow \tilde{E}_{a,\phi,m}, \tag{3.21}$$

and for Eq. (3.18) $m \geq 1$

$$\frac{m}{\rho} \underline{\boldsymbol{E}}_{s,T,m} + \frac{1}{\rho} \mathbf{e}_\rho E_{s,\phi,m} \leftarrow m \underline{\tilde{\boldsymbol{E}}}_{s,T,m}. \tag{3.22}$$

Equation (3.17) does not show the $1/\rho$ problem.

The variational problem is now solved by searching for the stationary point of Eqs. (3.16–3.18) subject to a PEC boundary condition on Γ_O and a PMC boundary condition on the axis.

If the substitutions in Eqs. (3.21) and (3.22) are not used, the continuity conditions on the axis may be imposed additionally in order to reduce the order of the finite element problem. However, they must not necessarily be imposed according to [81].

The BOR expansion yields the two lowest order, linearly polarised, fundamental LP01 (HE11 for $m = 1$) and first order LP11 (TE01 for $m = 0$ + TM01 for $m = 0$ + HE21 for $m = 2$) modes immediately (Fig. 3.1).

3.1.3 Combined Edge Node Finite Element Basis Functions

Finite element basis functions are used to expand the test function Eq. (2.73). The subdomains of the finite element basis functions are the triangle and the rectangle. The test function is inserted into Eqs. (3.16–3.18) and the integrals evaluated element by element. Simple analytical expressions for the integrals are available only for some special cases. In general, evaluation is performed by Gauss quadrature.

As finite element basis functions, the standard first order Lagrange (vertex) and first order Nédélec (edge) [82] (Whitney [83]), and the second order vertex and edge basis functions presented in [84] are employed. The latter form a hierarchical basis. That is, the first order basis is a subset of the second order basis. The advantage of hierarchical bases is that the element order can be changed in a systematic fashion. This is particularly useful for the so-called *hp* finite element method in which the resolution of finite element discretisation is traded for the order of the basis. The aim of the *hp* method is to give an optimum balance between required computational resources and accuracy of the approximation for a wide range of problems. A hierarchical basis is then useful because compatibility amongst finite elements is assured even if they differ in the selected basis orders.

A hierarchical basis with arbitrary order for node and edge finite elements is given in [85] (Ainsworth and Coyle basis) and discussed in the context of circularly symmetric cavities in [81].

The idea of solving Eqs. (3.16–3.18) with a combination of node and edge finite elements is presented in [78]. The assignment of the transverse $\underline{\boldsymbol{E}}_T(\rho, z)$ and azimuthal field component $E_\phi(\rho, z)$ to degrees of freedom (DOF)[3] of first order node and edge finite element basis functions is illustrated in Fig. 3.5. This choice eliminates the issue of spurious modes, which will be discussed in Sec. 3.1.4.

The placement of DOF for first and second order triangular and rectangular subdomains [84] is shown in Fig. 3.6. The first and second order basis functions corresponding to these DOF are given in App. C.

[3]The degrees of freedom correspond to the coefficients of the finite element basis functions that have to be determined in the course of finding the solution for Eqs. (3.16–3.18).

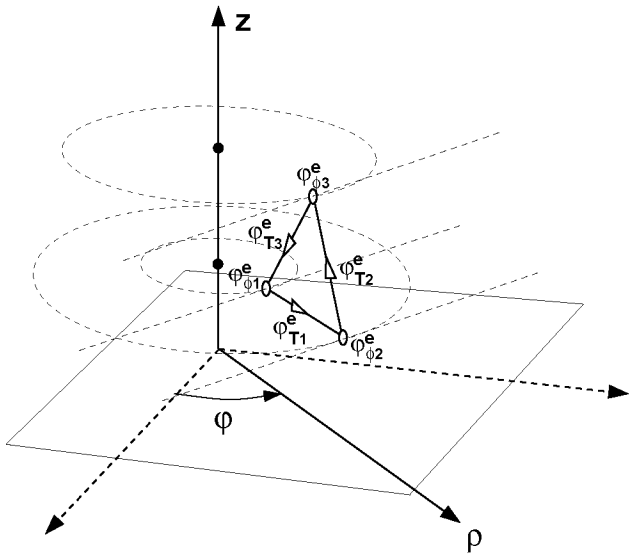

Figure 3.5: Combined node and edge finite element basis function ensures continuity of the tangential component of $\underline{\boldsymbol{E}}(\boldsymbol{r})$ on the surface of the circularly symmetric body formed by a finite element.

The finite element matrix assembly procedure is demonstrated in the following for the variational functional (3.18) with $m \geq 1$ using the substitution (3.22) for first order basis functions. The procedure for higher order basis functions is performed along the same lines.

The finite element expansion of the field

$$\underline{\boldsymbol{E}}_m(\rho, \phi, z) = \underline{\boldsymbol{E}}_{T,m}(\rho, z) \cos m\phi + E_{\phi,m}(\rho, z)\mathbf{e}_\phi \sin m\phi \qquad (3.23)$$

over either a triangular or rectangular subdomain of element e is then given by

$$\underline{\boldsymbol{E}}_{T,m}(\rho, z) = \sum_{i=1}^{3,4} \varphi^e_{Ti}\mathbf{N}^e_i(\rho, z) \quad E_{\phi,m}(\rho, z) = \sum_{i=1}^{3,4} \varphi^e_{\phi i} N^e_i(\rho, z). \quad (3.24)$$

When Eq. (3.23) and Eq. (3.24) are inserted into the variational functional (3.18) and integrations are carried out elementwise a matrix

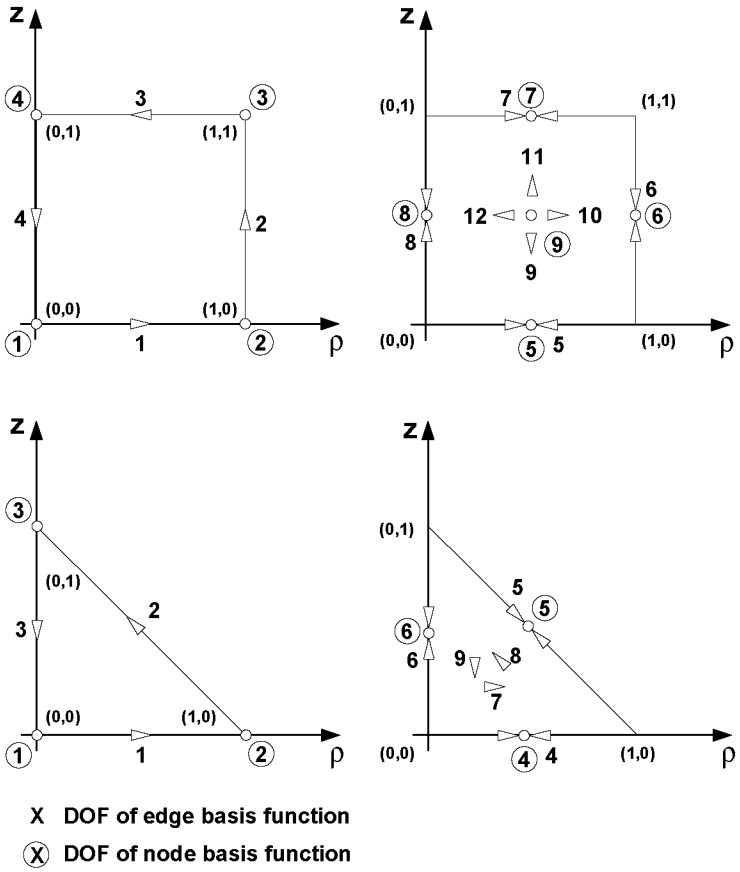

Figure 3.6: Placement of degrees of freedom (DOF) in triangles and rectangles for first and second order functions.

equation of the form

$$
\begin{aligned}
F\left(\begin{Bmatrix}\psi_{T,m}\\ \psi_{\phi,m}\end{Bmatrix}\right) =& \begin{Bmatrix}\varphi_{T,m}\\ \varphi_{\phi,m}\end{Bmatrix}^T \cdot \begin{bmatrix}A_{TT,m} & A_{T\phi,m}\\ A_{\phi T,m} & A_{\phi\phi,m}\end{bmatrix} \cdot \begin{Bmatrix}\varphi_{T,m}\\ \varphi_{\phi,m}\end{Bmatrix} \\
&- \frac{\omega^2}{c_0^2} \begin{Bmatrix}\varphi_{T,m}\\ \varphi_{\phi,m}\end{Bmatrix}^T \cdot \begin{bmatrix}B_{TT,m} & B_{T\phi,m}\\ B_{\phi T,m} & B_{\phi\phi,m}\end{bmatrix} \cdot \begin{Bmatrix}\varphi_{T,m}\\ \varphi_{\phi,m}\end{Bmatrix} \\
&- \begin{Bmatrix}\varphi_{T,m}\\ \varphi_{\phi,m}\end{Bmatrix}^T \cdot \begin{bmatrix}C_{TT,m} & C_{T\phi,m}\\ C_{\phi T,m} & C_{\phi\phi,m}\end{bmatrix} \cdot \begin{Bmatrix}\varsigma_{T,m}\\ \varsigma_{\phi,m}\end{Bmatrix}
\end{aligned} \tag{3.25}
$$

results. The variable φ^e_{Ti} determines the value of the DOF of edge i in element e and $\varphi^e_{\phi i}$ the value of the DOF of node i in element e. The constant source term $\underline{\boldsymbol{F}}_m(\rho, \phi, z\omega)$ is expanded accordingly using constants ς^e_{Ti} $\varsigma^e_{\phi i}$. Matrix A, B, and C can be identified as discretised versions of the three terms given in the variational functional (3.18).

In order to find the stationary point of the discretised variational functional, Eq. (3.25) is differentiated with respect to the components of

$$
\begin{Bmatrix}\varphi_{T,m}\\ \varphi_{\phi,m}\end{Bmatrix}^T \tag{3.26}
$$

and set to zero. Applying similar reasoning as in Eq. (3.15) this yields the sparse generalised complex symmetric non-Hermitian matrix equation

$$
\begin{aligned}
&\left(\begin{bmatrix}A_{TT,m} & A_{T\phi,m}\\ A_{\phi T,m} & A_{\phi\phi,m}\end{bmatrix} - \frac{\omega^2}{c_0^2}\begin{bmatrix}B_{TT,m} & B_{T\phi,m}\\ B_{\phi T,m} & B_{\phi\phi,m}\end{bmatrix}\right) \cdot \begin{Bmatrix}\varphi_{T,m}\\ \varphi_{\phi,m}\end{Bmatrix} \\
&= \begin{bmatrix}C_{TT,m} & C_{T\phi,m}\\ C_{\phi T,m} & C_{\phi\phi,m}\end{bmatrix} \cdot \begin{Bmatrix}\varsigma_{T,m}\\ \varsigma_{\phi,m}\end{Bmatrix}.
\end{aligned} \tag{3.27}
$$

If all $\varsigma_{T,m}$ and $\varsigma_{\phi,m}$ are set to zero the eigenproblem

$$
\begin{bmatrix}A_{TT,m} & A_{T\phi,m}\\ A_{\phi T,m} & A_{\phi\phi,m}\end{bmatrix} \cdot \begin{Bmatrix}\varphi_{T,m,k}\\ \varphi_{\phi,m,k}\end{Bmatrix} = \frac{\omega_k^2}{c_0^2}\begin{bmatrix}B_{TT,m} & B_{T\phi,m}\\ B_{\phi T,m} & B_{\phi\phi,m}\end{bmatrix} \cdot \begin{Bmatrix}\varphi_{T,m,k}\\ \varphi_{\phi,m,k}\end{Bmatrix} \tag{3.28}
$$

is obtained with the index $k = 1 \ldots N$ counting the modes.

The order of the sparse matrices is

- $n_{edge} + n_{node}$ for first order basis functions

- $n_{edge} + n_{node} + n_{edge} + n_{edge} + 2n_{tri} + 4n_{rect} + n_{rect}$
  $= 3n_{edge} + n_{node} + 2n_{tri} + 5n_{rect}$ for second order basis functions

where n_{tri} is the number of triangles in the mesh, n_{rect} the number of rectangles, n_{node} the number of nodes, and n_{edge} the number of edges.

The essential PEC boundary conditions are introduced by erasing rows and columns in matrices A, B and C corresponding to the DOF being set to zero [38].

The convergence behaviour of first and second order basis functions is assessed in Fig. 3.7 for the TE1m1 mode of the free dielectric sphere. A x/λ discretisation with $x = 3$, 7, 15, 30, 60 was chosen for air and the dielectric sphere with λ the wavelength in the respective material[4]. The cross-section of the sphere is approximated with a $20\,x$ segment polygon. In the PML $s' = 1$, and s'' evolves with a quadratic profile from $s'' = 0$ on Γ_I to $s'' = 5.0$ on Γ_O. The PML is 0.75λ thick and 2.0λ away from the surface of the sphere. The second order basis functions show a substantially higher exponential convergence rate than the first order functions.

3.1.4 Spurious Modes

Spurious modes are numerical solutions of the discretised Maxwell vectorial wave equation that have no correspondence to physical reality. In any case they should not be confused with unwanted but physically existing modes.

In the context of this work spurious modes are defined as inconsistent finite element approximations of static solutions of the *continuous* Maxwell vectorial wave equation

$$\nabla \times \mu_r(\boldsymbol{r})^{-1} \cdot (\nabla \times \underline{\boldsymbol{E}}(\boldsymbol{r})) = \frac{\omega^2}{c_0^2} \varepsilon_r(\boldsymbol{r}) \cdot \underline{\boldsymbol{E}}(\boldsymbol{r}) \tag{3.29}$$

given here in the homogeneous form. That is, spurious modes only appear in the *discretised* version of the Maxwell vectorial wave equation. The divergence of both sides of Eq. (3.29) is taken, and since

[4] That is, the dielectric sphere is discretised more densely than air according to its refractive index.

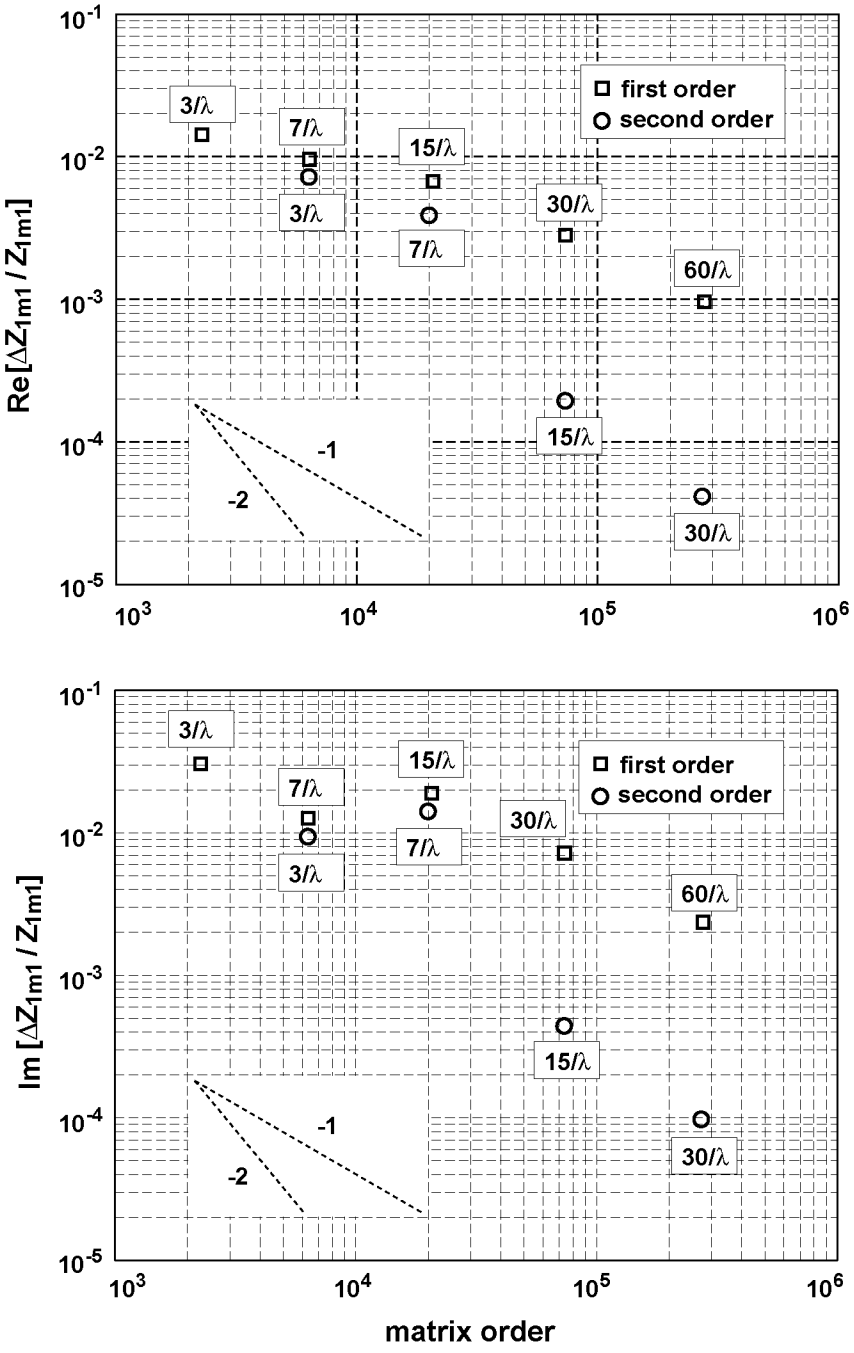

Figure 3.7: Convergence of first and second order basis functions for the TE1m1 mode of the free dielectric sphere with $\varepsilon = 12$.

the divergence of the curl of any vector is zero,

$$0 = \frac{\omega^2}{c_0^2} \nabla \cdot (\varepsilon_r(\boldsymbol{r}) \cdot \underline{\boldsymbol{E}}(\boldsymbol{r})) \tag{3.30}$$

is obtained. It follows that solutions of Eq. (3.29) are either divergence free $\nabla \cdot (\varepsilon_r(\boldsymbol{r}) \cdot \underline{\boldsymbol{E}}(\boldsymbol{r})) = 0$, $\omega \neq 0$ or static $\omega = 0$.

The *consistent* static solutions of the continuous Eq. (3.29) can be formed by taking the gradient of a certain scalar function $\phi(\boldsymbol{r})$

$$\underline{\boldsymbol{E}}(\boldsymbol{r}) = -\nabla\phi(\boldsymbol{r}). \tag{3.31}$$

These are the nontrivial solutions $\underline{\boldsymbol{E}}(\boldsymbol{r}) \neq \boldsymbol{0}$ with $\nabla \times \underline{\boldsymbol{E}}(\boldsymbol{r}) \equiv \boldsymbol{0}$, the nullspace of the curl, and $\omega = 0$, accordingly.

The *inconsistent* static solutions – that is the spurious solutions – of Eq. (3.29), which was discretised using a certain finite element basis, are solutions for which no scalar functions $\phi(\boldsymbol{r})$ in Eq. (3.31) exist. The function $\phi(\boldsymbol{r})$ is, of course, never computed. Nevertheless, assuming its non-existence, it can be concluded that Eq. (3.31) will only be poorly approximated during the process of finding the stationary point of the variational functional. The consequence is that eigenvalues of inconsistent static solutions will not lie at $\omega = 0$ (as they should) but at some finite value, because the eigenvectors of the inconsistent static solution do not fulfil Eq. (3.31) accurately. It turns out that the degree of inconsistency of the static solution is linked to the finite element basis and mesh employed.

This shall be illustrated with an example. A 2D triangular mesh is given in the ρ-z plane shown in Fig. 3.8 where the surface $f(\rho, z)$ is shown. It is formed by the scalar node basis functions $N_1^e(\rho, z)$ associated with node 1. Two cases are considered:

1. The surface $f(\rho, z)$ represents the ρ and z components of the 2D vector field $\underline{\boldsymbol{E}}_T(\rho, z)$. That is, the finite element basis functions are given by $f(\rho, z)$ and each component of the vector field is continuous. Which potential $\phi(\rho, z)$ would fulfil $\underline{\boldsymbol{E}}_T(\rho, z) = -\nabla_T\phi(\rho, z)$ in this case?

2. The surface $f(\rho, z)$ represents the potential function $\phi(\rho, z)$. It is continuous, but its derivative $\nabla_T\phi(\rho, z)$ is not. The potential

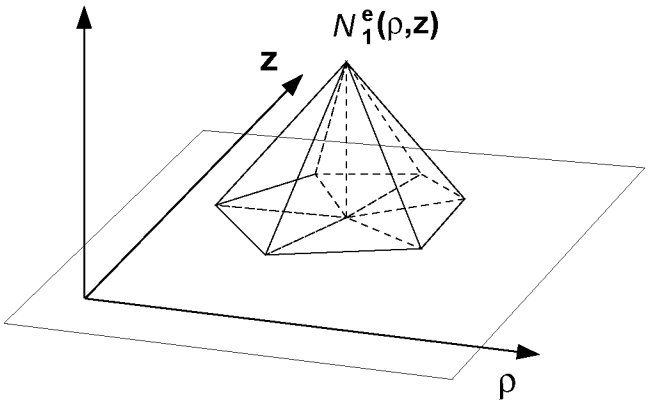

Figure 3.8: 2D mesh of triangles showing the surface generated by the scalar node basis functions $N_1^e(\rho, z)$ associated with node 1 for finite elements $e = 1 \ldots 6$.

function $\phi(\rho, z)$ is then said to have C^0 continuity. Which finite element basis functions could render the derivative $\nabla_T \phi(\rho, z)$ in this case?

For case 1 only quadratic functions $\phi(\rho, z)$ with $\nabla_T \phi(\rho, z)$ linear and continuous are possible. The potential function $\phi(\rho, z)$ is then said to have C^1 continuity. If a C^1 quadratic function can be found where $-\nabla_T \phi(\rho, z) = [f(\rho, z), 0, f(\rho, z)]^T$ is fulfilled on the vertices, equality is automatically guaranteed everywhere because $-\nabla_T \phi(\rho, z)$ and $[f(\rho, z), 0, f(\rho, z)]^T$ are linear inside each element. References [87, 88] show that such quadratic C^1 piecewise polynomials for the interpolation of functions prescribed by discrete values on mesh vertices only exist over special meshes. In [88] a procedure is given by which a quadratic C^1 mesh can be generated from an arbitrary mesh by subdividing each of the triangles of the original mesh into six triangles (Fig. 3.9). On such subdivided meshes a quadratic C^1 potential function $\phi(\rho, z)$ can always be defined. Consequently, on such special meshes the static solutions are approximated correctly, and all eigenvalues $\omega = 0$ are computed as exactly zero. However, the required special mesh properties will restrict the use of this approach.

For case 2 the question is reversed with respect to case 1. Since the potential function $\phi(\rho, z)$ is continuous along the element edge, the derivative parallel to each element edge is continuous. The derivative

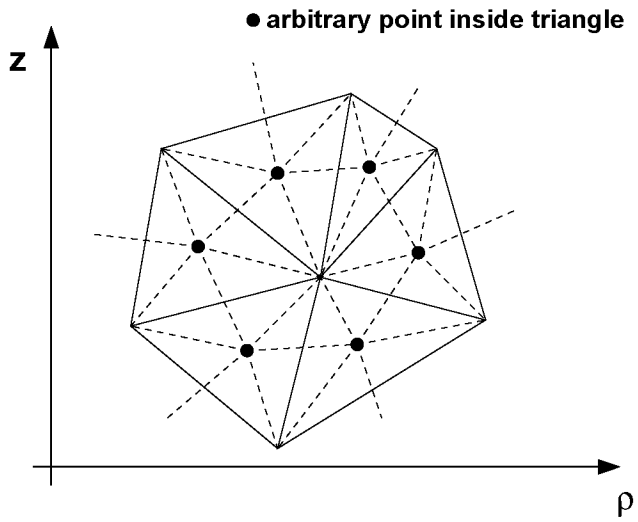

Figure 3.9: In an arbitrary triangular mesh each triangle has to be divided into six to ensure continuity of the derivative of the quadratic surface interpolating the vertices.

normal to each element edge is discontinuous. Consequently, if $\phi(\rho, z)$ is approximated by first order finite element basis functions, the approximation for $\underline{\boldsymbol{E}}_T(\rho, z)$ must be chosen in such a way that on the element edges its tangential components are continuous, but its normal components are discontinuous. This requirement is automatically fulfilled by the edge finite element basis employed here (Fig. 3.10): the trick is to make the tangential component of $\underline{\boldsymbol{E}}_T(\rho, z)$ on the element edge equivalent to the DOF shared by elements on the boundary. Note that the edge finite element basis shown in Fig. 3.10 is identical to the linear edge basis used in this work (Sec. 3.1.3 and Fig. C.1 in App C). The normal component of $\underline{\boldsymbol{E}}_T(\rho, z)$ is discontinuous on element edges and is minimised in the process of finding the stationary point in the least squares sense[5].

Moreover, it shall briefly be noted that pth order edge element bases with $p > 1$ can be constructed similarly, starting from potential functions $\phi(\rho, z)$ given by pth order piecewise polynomials.

This also applies to the combined node and edge finite element bases and the modified bases introduced in Eqs. (3.21) and (3.22), be-

[5]This edge basis is sometimes also called the linear normal, constant tangential (LNCT) edge basis.

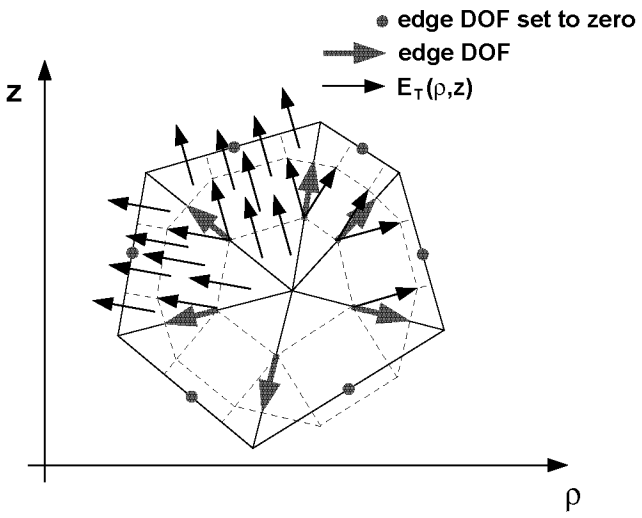

Figure 3.10: The edge finite element basis (also see Fig. C.1) ensures continuity of the tangential component of $\underline{\boldsymbol{E}}_T(\rho, z) = -\nabla_T \phi(\rho, z)$. The normal component is discontinuous on element edges.

cause they retain the continuity property of the tangential component of the 3D vector $\underline{\boldsymbol{E}}(\rho, z)$ on the circularly symmetric body shown in Fig. 3.5.

The issue of spurious modes has been a source of confusion in electromagnetics over years. It was originally thought that spurious modes appeared in the spectrum due to the fact that their divergence integrated over the computational domain was non-zero, which turned out to be wrong. Although edge finite element basis functions have zero divergence within each element, the solutions of the discretised Eq. (3.29) spanned by them do not, if the solution is static $\omega = 0$. In fact, for $\omega = 0$ the solution includes a non-zero divergence along the element edges. It is important to note that the success of edge elements in eliminating spurious modes derives from the fact that they approximate the null space of the curl operator correctly and not because they are divergence free. Also note that the presence of spurious modes has no connection to using PML ABC whatsoever.

Spurious solutions have to be discussed at this point because of their relation to the static solutions of Maxwell's vectorial wave equation. It was stated in Sec. 2.2 that the static solutions are unwanted solutions in the context of VCSEL simulation. It is essential that, by using the combined edge node finite element basis, they appear at

$\omega = 0$ in the spectrum of the eigenproblem Eq. (3.29), where they do not interfere with the wanted solutions.

3.2 Electro-Thermal Transport Equations

The numerical formulation as implemented in the DESSIS device simulator is used. The electro-thermal transport equations are discretised by application of the Box Method. Only a brief sketch of the numerical formulation of the equations in 2D is given here[6]. More details can be found in

- [89, 90, 91] for the electronic transport equations
- [48, 92] for the extension to the non-isothermal case (energy balance or thermodynamic model)
- [23, 29] in the context of laser simulation.

Consider the general non-linear partial differential equation of the form

$$\nabla_{\boldsymbol{x}} \cdot \boldsymbol{F}(\boldsymbol{x}, \boldsymbol{y}) + g(\boldsymbol{x}, \boldsymbol{y}) = 0 \tag{3.32}$$

where $\boldsymbol{F}(\boldsymbol{x}, \boldsymbol{y})$ is a vectorial and $g(\boldsymbol{x}, \boldsymbol{y})$ a scalar function of $\boldsymbol{x}$ and $\boldsymbol{y}$. Furthermore, consider Gauss' Divergence Theorem

$$\iint_A \nabla_{\boldsymbol{x}} \cdot \boldsymbol{F}(\boldsymbol{x}, \boldsymbol{y}) d^2\boldsymbol{x} = \oint_C \boldsymbol{F}(\boldsymbol{x}, \boldsymbol{y}) \boldsymbol{e}_n \tag{3.33}$$

with A the area bounded by contour C and $\boldsymbol{e}_n$ the unity normal vector on C pointing outward. The integral on the left gives the total flux leaving area A.

On a domain discretised by rectangular and triangular elements for each mesh vertex i a box with area A_i and contour C_i is defined by the mid-perpendiculars of the mesh edges as shown in Fig. 3.11.

The Box Method exploits the fact that the device equations of the thermodynamic model Eqs. (2.79–2.82) are given in the divergence

[6] The extension to 3D is straightforward [89, 90] using Gauss' Divergence Theorem in three dimensions.

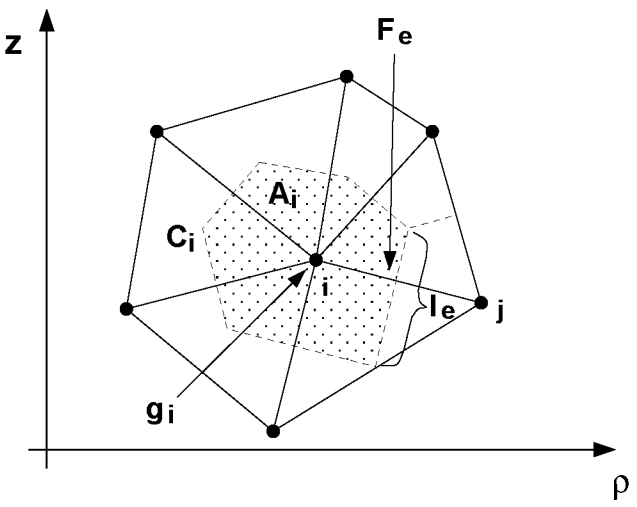

Figure 3.11: Box Method discretisation: box is defined by the mid-perpendiculars of the mesh edges.

form Eq. (3.32). The following approximation is made using Eq. (3.33)

$$\iint_{A_i} \nabla_{\boldsymbol{x}} \cdot \boldsymbol{F}(\boldsymbol{x},\boldsymbol{y}) + g(\boldsymbol{x},\boldsymbol{y}) d^2\boldsymbol{x} \approx \left(\sum_{edges(i)} l_e F_e \right) + g_i A_i. \qquad (3.34)$$

The flux through each one of the edges emerging from vertex i is approximated with $l_e F_e$ where l_e is the length of edge e and F_e is the mean flux of $\boldsymbol{F}(\boldsymbol{x},\boldsymbol{y})$ through edge e. Moreover, g_i is the average value of $g(\boldsymbol{x},\boldsymbol{y})$ inside A_i.

As a consequence the integration of the scaled (de Mari [93]) device equations (2.79–2.82) over the box area A_i can be approximated by

$$\sum_{edges(i)} l_e \left(\varepsilon \nabla \phi\right)_e = -A_i \left(p_i - n_i + N^+_{D,i} - N^-_{A,i}\right) \tag{3.35}$$

$$\sum_{edges(i)} l_e \left(\boldsymbol{j}_n\right)_e = A_i \left(R_i + \frac{\partial}{\partial t} n_i\right) \tag{3.36}$$

$$-\sum_{edges(i)} l_e \left(\boldsymbol{j}_p\right)_e = A_i \left(R_i + \frac{\partial}{\partial t} p_i\right) \tag{3.37}$$

$$-\sum_{edges(i)} l_e \left(\boldsymbol{S}\right)_e = A_i \left(H_i + c_{th,i} \frac{\partial}{\partial t} T_i\right). \tag{3.38}$$

for the Poisson equation and the continuity equations for the electrons, holes and the local heat, with $(\boldsymbol{F})_e$ denoting the mean flux of $\boldsymbol{F}$ through edge e. By discretising the current equations (2.97–2.99) along each edge and substituting the fluxes in Eqs. (3.35–3.38) a coupled non-linear system of device equations with the variables ϕ_i, n_i, p_i, T_i for each vertex i is obtained. It is completed by suitable boundary conditions on the outline of the computation domain [51, 90].

In the VCSEL simulator the integral in Eq. (3.34) is over a rotationally symmetric torus with cross-section A_i using Gauss' Divergence Theorem and approximated with a corresponding sum. At heterojunctions and at quantum well edges the appropriate current equations have to be used [17, 23, 53, 54]. In the quantum well Eqs. (3.36) and (3.37) are modified according to Eqs. (2.101) and (2.102).

Meshes fulfilling the Delaunay criterion are employed. Note that this ensures stable solutions if the above discretisation of the device equations is used [89].

Small Signal Modulation and Large Signal Transient Response

The analysis of the VCSEL small signal modulation response is introduced via the Impedance Field Method [94, 95], which was extended to comprise a photon rate equation Eq. (3.49) per optical mode considered. The method computes the response to a small signal sinu-

soidal excitation at frequency ω by evaluating the Jacobian of the electro-thermal system of equations (3.35–3.38) and the photon rate equations (3.49) in a certain bias point. The modulation response is obtained by performing this task for range of frequencies ω.

To obtain large signal transient responses the system of equations (3.35–3.38) and (3.49) is integrated in time using the trapezoidal rule / backward-differentiation formula (TR-BDF2) composite method [96].

3.3 Numerical Solution Methods

The non-linear electro-thermal matrix equations presented in Sec. 3.2, augmented with a photon rate equation per optical mode, are solved by Newton's Method [89, 97]. The numerical formulation of Maxwell's vectorial wave equation was discussed in detail in Sec. 3.1. The inhomogeneous form is solved by a LU factorisation with a direct linear solver and subsequent forward and back substitution for different right hand sides [98]. The eigenpairs of the homogeneous form are computed by the Jacobi-Davidson QZ algorithm with a preconditioner [73]. In a laser simulation the electro-thermal and the photon rate equations are coupled to Maxwell's wave equation employing a Gummel-type iteration scheme [99].

3.3.1 Newton-Raphson

The Newton-Raphson scheme available in the DESSIS device simulator is used. A conceptual summary shall be given here. Refer to [89, 97] for more details.

The discretised electro-thermal equations (3.35–3.38) together with the photon rate equations (3.49) and appropriate boundary conditions can be written as

$$\mathcal{F}(\boldsymbol{x}) = \boldsymbol{0} \tag{3.39}$$

where the vector function $\mathcal{F}(\boldsymbol{x})$ depends non-linearly on $\boldsymbol{x}$. The latter vector contains the variables of the system.

Starting from an initial guess $\boldsymbol{x}_i$ for a zero of $\mathcal{F}(\boldsymbol{x})$ a correction $\Delta\boldsymbol{x}_i$ is computed by finding the zero of a Taylor series expansion of $\mathcal{F}(\boldsymbol{x})$ with up to linear terms at the point $\boldsymbol{x} = \boldsymbol{x}_i$. The new guess is

then given by

$$\boldsymbol{x}_{i+1} = \boldsymbol{x}_i - \boldsymbol{J}_{\mathcal{F}}^{-1}(\boldsymbol{x}_i) \cdot \mathcal{F}(\boldsymbol{x}_i) \tag{3.40}$$

where

$$\{\boldsymbol{J}_{\mathcal{F}}(\boldsymbol{x})\}_{m,n} = \frac{\partial \mathcal{F}_m(\boldsymbol{x})}{\partial x_n} \tag{3.41}$$

is the Jacobian matrix of $\mathcal{F}(\boldsymbol{x})$ evaluated at $\boldsymbol{x}$. In practice, $\boldsymbol{J}_{\mathcal{F}}(\boldsymbol{x}_i)$ is not inverted directly as suggested by Eq. (3.40). Instead the linear system

$$\boldsymbol{J}_{\mathcal{F}}(\boldsymbol{x}_i) \cdot \Delta\boldsymbol{x}_i = -\mathcal{F}(\boldsymbol{x}_i) \tag{3.42}$$

is solved. In this work a LU factorisation is computed using a direct solver and the result obtained by forward and back substitution [98]. The update is then given by

$$\boldsymbol{x}_{i+1} = \boldsymbol{x}_i + \alpha_i \Delta\boldsymbol{x}_i \tag{3.43}$$

where the scalar parameter α_i, $0 < \alpha_i \leq 1$ is an additional damping factor that can be used to prevent overshoot effects if $\boldsymbol{x}_i$ is far away from the final solution [97].

The scheme is repeated until a convergence criterion is met. Common criteria are the norm of $\mathcal{F}(\boldsymbol{x})$ or the norm of the change $\Delta\boldsymbol{x}_i$ with respect to the norm of $\boldsymbol{x}_i$

$$\|\mathcal{F}(\boldsymbol{x}_i)\| < \epsilon_{abs} \qquad \frac{\|\Delta\boldsymbol{x}_i\|}{\|\boldsymbol{x}_i\|} < \epsilon_{rel}. \tag{3.44}$$

In this sense, Newton's Method replaces a system of non-linear equations with a sequence of linear equations. The convergence rate of Newton's method is normally quadratic [100], but the algorithm has to be started reasonably close to a solution in order to converge. Computational complexity in terms of operations and memory requirements is strongly dependent on how dense $\boldsymbol{J}_{\mathcal{F}}(\boldsymbol{x})$ is. Computation time and memory requirement for some selected practical examples are given in Ch. 4.

3.3.2 Jacobi-Davidson QZ Iteration Method

Solutions to Maxwell's wave equation (3.1) in the homogeneous form are obtained by searching for the stationary point of its discretised

variational functional, that is, by solving the sparse generalised complex symmetric[7] matrix eigenproblem (3.28). The order of the eigenproblem depends on the required accuracy of the solutions or equivalently on the number and the polynomial order of the finite elements in the mesh. For VCSEL cavities practical orders range from 500'000–2'000'000. Only a few (1–10) inner eigenpairs have to be computed. Eigenpairs are closely spaced in the part of the spectrum that is of interest. Hence, the matrix eigenproblem is solved using the Jacobi-Davidson QZ subspace iteration method with high spectral selectivity. The implementation that is used in this work and the presentation in this section follows reference [73].

The eigenproblem (3.28) can be rewritten in the general form

$$\boldsymbol{A}\boldsymbol{q} = \lambda \boldsymbol{B}\boldsymbol{q} \tag{3.45}$$

with eigenvalue $\lambda = \omega^2/c_0^2$ and eigenvector $\boldsymbol{q}$. Matrices $\boldsymbol{A}$ and $\boldsymbol{B}$ are in $C^{n\times n}$. Multiplying from the left by $\boldsymbol{Z}_k^H$ and substituting $\boldsymbol{q} = \boldsymbol{Q}_k\boldsymbol{x}$ the partial generalised Schur form [73] with dimension k

$$\underbrace{\boldsymbol{Z}_k^H \boldsymbol{A}\boldsymbol{Q}_k}_{\boldsymbol{S}_k}\boldsymbol{x} = \lambda \underbrace{\boldsymbol{Z}_k^H \boldsymbol{B}\boldsymbol{Q}_k}_{\boldsymbol{T}_k}\boldsymbol{x} \tag{3.46}$$

of the large eigenproblem can be obtained. Matrices $\boldsymbol{S}_k$ and $\boldsymbol{T}_k$ are upper triangular with dimension $k \times k$, $\boldsymbol{Q}_k$ and $\boldsymbol{Z}_k$ are unitary $n \times k$ matrices[8]. Furthermore, if $\boldsymbol{x}$ λ is an eigenpair of Eq. (3.46) then $\boldsymbol{q} = \boldsymbol{Q}_k\boldsymbol{x}$ λ is an eigenpair of Eq. (3.45).

The goal of the Jacobi-Davidson QZ algorithm is to construct continuously improving approximations of the matrices $\boldsymbol{Q}_k$ and $\boldsymbol{Z}_k$ that yield the partial generalised Schur form (3.46).

To this end a low-dimensional subspace is generated onto which the given eigenproblem is projected, which is the standard Rayleigh-Ritz method. The generalised Schur form of the small projected eigenproblem can be computed easily by the QZ algorithm. From this Schur form approximations for the wanted eigenpair, and the partial generalised Schur form of the given large eigenproblem can be obtained.

A correction equation of the order of the large eigenproblem is set up – the Jacobi correction equation – that attempts to correct

[7] The eigenproblem is complex symmetric and non-Hermitian.

[8] The superscript H denotes complex conjugate transposition.

the current eigenvector approximation in the space orthogonal to it. That is, the result of the correction equation is an optimal orthogonal extension of the low-dimensional subspace. The Jacobi correction equation may be solved by any method of choice. If the exact value for the eigenvalue was known, the correction equation, if solved exactly, would yield the exact eigenvector. Since the eigenvalue of an eigenproblem is usually only known approximately in advance, there is no point in solving the correction equation exactly. Also, for large problems it is more efficient to solve this equation only approximately using an iterative method. The convergence properties of such an iterative method can be improved by preconditioning.

In this work the solution of the Jacobi correction equation is determined using the biconjugate gradient stabilised (BiCGstab) method [101] with a preconditioner

$$\boldsymbol{M} = (\boldsymbol{A} - \lambda \boldsymbol{B})^{-1} \tag{3.47}$$

where λ is a guess for the eigenvalue ω^2/c_0^2. A method to determine a guess for λ for a problem with closely spaced eigenvalues is presented in Sec. 4.1.2.

At the beginning, the low-dimensional subspace is initialised with a random eigenvector. The algorithm is repeated until the following convergence criterion is met

$$\frac{\|\boldsymbol{A}\boldsymbol{q} - \lambda \boldsymbol{B}\boldsymbol{q}\|}{\|\lambda\|} < \epsilon. \tag{3.48}$$

The preconditioner is computed exactly and once per eigenproblem using a parallel direct LU factorisation [98]. Numerical experiments using cheaper preconditioners based on geometrical multigrid have been carried out. So far only the preconditioner given in Eq. (3.47) has provided reliable convergence properties for solving Eq. (3.28).

3.3.3 Coupling the Optical and Electro-Thermal Problems

It was shown in Sec. 2.1.2 that Maxwell's wave equation, by applying expansion (2.6), is transformed into a set of N decoupled photon rate

equations

$$\frac{d}{dt}\mathsf{S}_k(t) = -2\omega_k''(t)\,\mathsf{S}_k(t) + R_k^{sp}(t) \tag{3.49}$$

with $k = 1 \ldots N$ and the eigenproblem (2.9). The electric field which corresponds to the eigenvector of this problem is normalised according to Eq. (2.13).

The photon number $\mathsf{S}_k(t)$ changes by several orders of magnitude when the VCSEL drive current passes the lasing threshold. In contrast, the normalised electric field $\underline{\boldsymbol{E}}_k(\boldsymbol{r}, t)$ barely changes over the entire operation range of the VCSEL device, if the field is mainly index guided. Often, partial index guiding is sufficient for the approach to work, that is, if some sort of guiding is provided by the cold[9] optical cavity. Furthermore, the angular frequency $\omega_k'(t)$ of mode k changes only weakly.

It follows that the non-linear system of equations (3.39) is augmented by a photon rate equation (3.49) per optical mode. Accordingly, the photon numbers $\mathsf{S}_k(t)$ appear as new variables in the vector $\boldsymbol{x}$ of $\mathcal{F}(\boldsymbol{x})$. From a conceptual point of view, the new variable is treated as a virtual vertex in the mesh of the device. For the computation of static and stationary VCSEL characteristics an auxiliary variable and equation is introduced to ensure that $\omega_k'' \geq 0$ in Eq. (3.49) at all times [23]. In this way quadratic convergence of the Newton Method is maintained even around threshold.

In order to be able to apply Newton's Method to the new equations, their derivatives with respect to all variables in $\boldsymbol{x}$ have to be computed to construct the Jacobian $\boldsymbol{J}_{\mathcal{F}}(\boldsymbol{x})$. To this end derivatives of $2\omega_k''(t)$ and $R_k^{sp}(t)$ with respect to the variables $\boldsymbol{x}$ are needed. The variables are the local electron and hole density, electro-static potential, temperature, and the photon number of each mode. So far, $2\omega_k''(t)$ has been determined as the result of eigenproblem (2.9), which is unsuitable because the required derivatives cannot be calculated directly. Note that $2\omega_k''(t)$ has the significance of a relative rate of change of electromagnetic energy stored in mode k and can alternatively be expressed by evaluating the integral in Eq. (2.71) for the

[9]The term cold cavity refers to the optical cavity without any change induced by the electro-thermal equations: optical gain and loss in the active region, temperature induced change of refractive index.

entire mode volume. It turns out that this integral can be split into one that is coupled strongly to the variables $\boldsymbol{x}$ and one that is only weakly coupled

$$\begin{aligned} 2\omega_k'' &= 2\omega_{strong,k}'' + 2\omega_{weak,k}'' \\ &= -\frac{\iiint_{V_{\text{strong}}} \langle \nabla \cdot \boldsymbol{S}_k(\boldsymbol{r}) \rangle \, dV}{\iiint_O \langle w_k(\boldsymbol{r}) \rangle \, dV} - \frac{\iiint_{V_{\text{weak}}} \langle \nabla \cdot \boldsymbol{S}_k(\boldsymbol{r}) \rangle \, dV}{\iiint_O \langle w_k(\boldsymbol{r}) \rangle \, dV}. \end{aligned} \tag{3.50}$$

The two regions V_{strong} and V_{weak} are chosen in such a way that they are disjoint but that their union covers the volume O bounded by Γ_O shown in Fig. 2.11. Since the optical dissipation or generation rate changes by several orders of magnitude in the active region it is covered by V_{strong}. Region V_{weak} comprises the remainder of O. In this area optical dissipation changes only weakly because of small changes in the electric field $\underline{\boldsymbol{E}}_k(\boldsymbol{r})$ that are due to gain or absorption in the active region, temperature dependence of the refractive index and changing radiative losses.

It is evident from comparing Eqs. (2.66) and (2.69) to Eq. (3.11) that the rates given in Eq. (3.50) can be computed directly by summing expressions involving the discretised operators in Eq. (3.25) and the electric field over the respective volumes. Due to the linearity of the sum and by virtue of the chain rule, derivatives of $2\omega_{strong,k}''$ and $2\omega_{weak,k}''$ with respect to the variables $\boldsymbol{x}$ can be made to act on the dielectric function (3.10) and, hence, on the optical material loss / gain (2.14). For the latter, assuming the free carrier optical loss / gain model that was presented, analytical derivatives with respect to $\boldsymbol{x}$ are readily available. Derivatives are only computed for $2\omega_{strong,k}''$. They are neglected and set to zero for $2\omega_{weak,k}''$.

Similarly, derivatives of $R_k^{sp}(t)$ with respect to $\boldsymbol{x}$ are obtained using Eqs. (2.17) and (2.18).

In contrast to the photon number $S_k(t)$ the normalised electric field $\underline{\boldsymbol{E}}_k(\boldsymbol{r}, t)$ changes only little over the operation range of the VCSEL. That is, the eigenproblem (2.9) and the non-linear equations (3.39) are only weakly coupled, and a Gummel-type iteration scheme is therefore

employed [29]

$$\begin{aligned} \mathcal{F}(\underline{\boldsymbol{E}}_i(\boldsymbol{r}), \omega_i' \rightarrow \mathbf{x}_{i+1}) &= 0 \quad \text{Newton's Method} \\ \delta F(\mathbf{x}_{i+1} \rightarrow \underline{\boldsymbol{E}}_{i+1}(\boldsymbol{r}), \omega_{i+1}') &= 0 \quad \text{JDQZ} \end{aligned} \tag{3.51}$$

that is shown here for step $i \rightarrow i+1$. The mode index k is omitted for the sake of clarity. If a multi-mode problem is solved, $\underline{\boldsymbol{E}}_i(\boldsymbol{r})$ and ω_i' represent all eigenpairs $k = 0, \ldots, N$ at step i since they are obtained concurrently during a JDQZ solve step. The variables to the left of the arrow are held at fixed values whereas the ones on the right are computed in each step. The iteration is continued until the error criteria set out in Eqs. (3.44) and (3.48) are concurrently met. At this point the electro-thermo-optical equations are said to be self-consistently solved. Figure 3.12 shows a flow chart of the coupled iteration scheme and Fig. 3.13 a Gummel iteration history. The latter is for a simulation of the VCSEL device shown in Figs. 3.1 and 3.2, and is comparable to the ones carried out in Sec. 4.4. The increase in required Gummel iterations per bias point towards higher currents can be explained with the increased self-heating and, consequently, stronger coupling of the electric field via the temperature dependence of the refractive index.

Hence, a sequence of eigenproblems has to be solved, where each one can be seen as the perturbed version of the former in the sequence. This fact can be exploited by the JDQZ subspace iteration method. Firstly, the search subspace is constructed starting from the eigenvector of the former eigenproblem, instead of a random vector, and the guess λ in Eq. (3.47) is taken as the former eigenvalue. This continuation type approach results in less time required to find a solution as long as the eigenproblem changes only little [102]. Secondly, the preconditioner (3.47), that was obtained expensively by direct matrix LU factorisation, is re-cycled for several of the eigenproblems in the sequence [103].

The example shown in Fig. 3.13 takes approximately 24 hours (86'186 seconds) to compute 78 bias points and requires a total of 406 Gummel iterations for this. The preconditioner is recomputed only 38 times and re-cycled in the remaining iterations. The time to compute a Gummel iteration is about 220 seconds on average: 160 seconds are spent on the electro-thermal problem and 60 seconds on the opti-

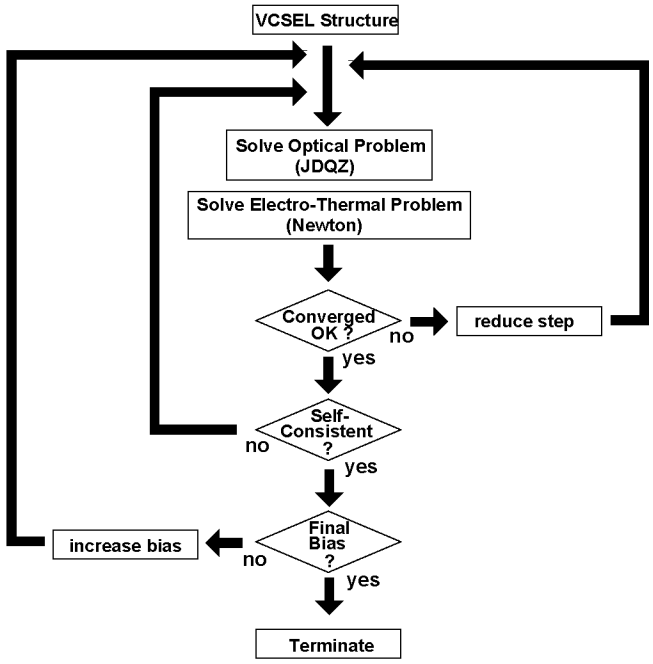

Figure 3.12: Flow chart describes procedure for self-consistent coupled electro-thermo-optical simulation as implemented in DESSIS.

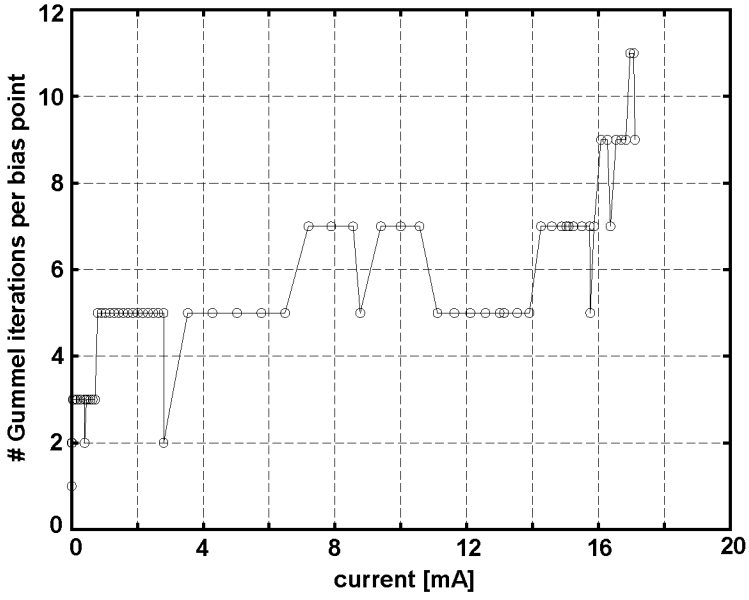

Figure 3.13: Gummel iteration history for self-consistent coupled electro-thermo-optical simulation.

cal problem. Computing the preconditioner once takes approximately 120 seconds, and solving the optical problem with a given preconditioner 50 seconds. Therefore, if the preconditioner was computed in every Gummel iteration an approximate run time of $406 \cdot (160 + 120 + 50) = 134'000$ seconds would result. This translates into a time saving of around 35% if the preconditioner is re-cycled.

It was already mentioned in the introduction of Ch. 3 that the complexity of the non-linear system of equations Eq. (3.39) does not permit resolving the VCSEL DBR stacks by a Scharfetter-Gummel discretisation, due to excessive requirements in memory and computation time. DBR stacks are, therefore, represented as homogeneous regions with effective material parameters. In contrast, the DBR stacks have to be resolved for the optical problem. Consequently, two separate meshes are used: a coarse one ($\approx$10'000 elements) for the electro-thermal problem and a finer one ($\approx$200'000 elements) for the optical problem (see Figs. 3.1 and 3.2). Linear interpolation translates variables between the two meshes [29]. It is beneficial for the convergence properties of the Gummel iteration (3.51) to evaluate the strongly coupled integral in Eq. (3.50) on the coarse electro-thermal mesh. Evaluating the weakly coupled integral on the finer optical mesh is unproblematic. Hence, the coarser electro-thermal mesh has to be capable of resolving the optical field in the active region, so that errors in $2\omega''_{strong,k}$ originating from grid interpolation can be kept low.

Chapter 4

Simulation Benchmarks and Examples

Practical aspects of optical mode calculation in cylindrical microcavities and coupled electro-thermo-optical VCSEL simulation are discussed and illustrated.

Results computed with the LUMI mode solver package are compared with other methods. The spontaneous emission enhancement for a microcavity device is calculated. It is shown how the latter result can be applied to reliably find a target value to initialise the JDQZ algorithm which is used to numerically compute optical modes (see Sec. 3.3.2).

Static characteristics and modulation response are computed with the electro-thermo-optical VCSEL simulator for various device types. The VCSEL simulator is calibrated and assessed with measured data of a commercial VCSEL device[1]. Finally, in order to demonstrate the practical use of the simulator as a design tool, the task of finding a device structure with maximum single mode emission power is performed[2]. All examples were computed on a HP/Compaq AlphaServer

[1]The VCSEL structure and measurements are provided by courtesy of Avalon Photonics AG, Switzerland.

[2]The evaluations of the second order bilinear forms given in App. C were developed by Oscar Chinellato (Institute of Computational Science, ETH Zürich) and kindly provided to produce some of the results [104].

ES45 1250 MHz / 32 GBytes, and computation times are given for this machine using one processor.

4.1 Optics Solver

4.1.1 COST268 Benchmark

The LUMI optical mode solver described in Sec. 3.1 is assessed using part of the COST268 VCSEL benchmark [35]. The VCSEL structure shown in Fig. 4.1 has an antinode oxide aperture with variable radius. It is discretised with approximately 84'000 finite elements, depending on the radius of the oxide, using a mesh approximately 70 elements wide and 1200 elements high. PML thickness is 0.5 μm and the PML layers are resolved using 16 finite elements in the direction perpendicular to the boundary. The mesh length in the VCSEL DBR mirrors is $\lambda/32$, where λ is the wavelength in the material.

For linear finite elements this discretisation results in an eigenproblem of order 240'000, for second order finite elements of order 960'000. Computation takes around 2 minutes and 2.0 GBytes for the linear finite elements and 6 minutes and 8.5 GBytes for the second order finite elements.

Figures 4.2 and 4.3 show how resonance wavelength and threshold gain for the fundamental and first order mode compare to other vectorial models *Green* [24], *CAMFR* [69] and the effective frequency *EF* [62, 105] scalar model. The results are computed with second order finite elements and are shown for the fundamental HE11 mode (vectorial models), LP01 (scalar models), and first order TE01 mode (vectorial models), LP11 (scalar models), versus a variation in the antinode oxide radius. For the first order vectorial mode TE01 was chosen. Alternatively, TM01 or HE21 could have been taken since, according to Sec. 2.2.6, all three modes degenerate to LP11 in the scalar limit.

The LUMI results agree well with data generated using the vectorial solvers *Green* and *CAMFR*. This is also confirmed by the convergence of second order elements for the $32/\lambda$ discretisation determined for the dielectric sphere in Fig. 3.7. As pointed out in [35], the scalar solver *EF* does not take into account diffraction losses, and therefore

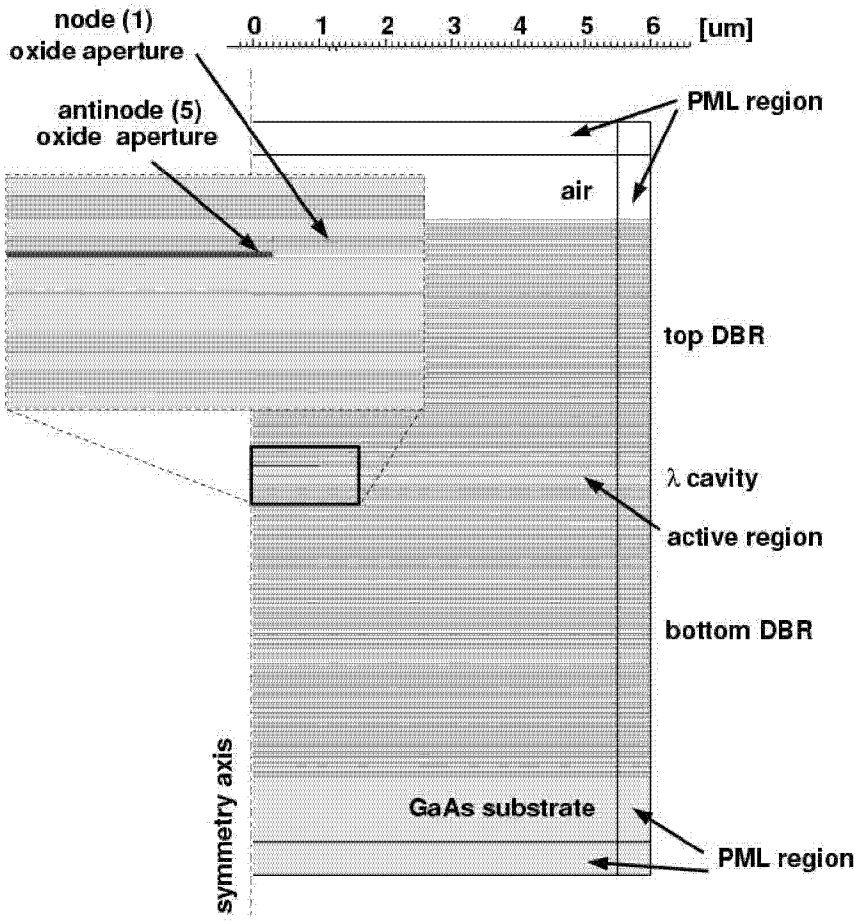

Figure 4.1: COST268 benchmark AlGaAs/GaAs VCSEL structure, 25 DBR pairs at top and 29.5 DBR pairs at bottom.

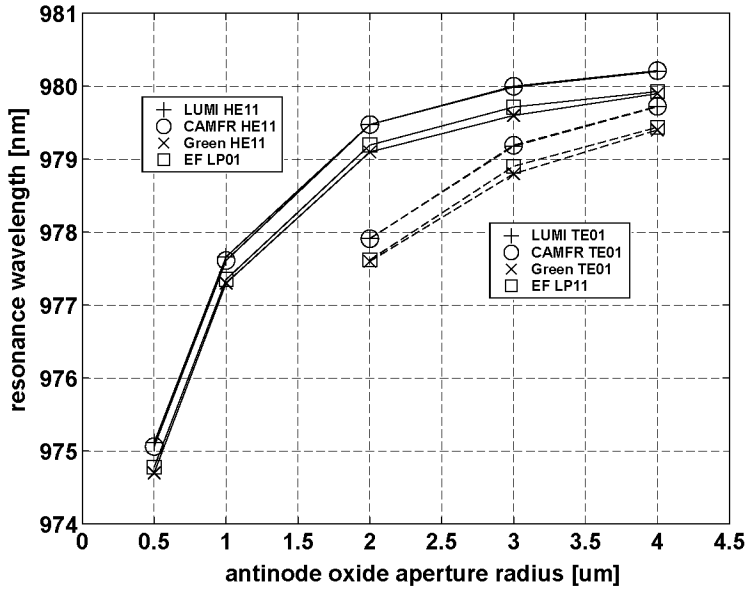

Figure 4.2: COST268 benchmark VCSEL structure. Resonance wavelength of the fundamental HE11 (vectorial models) / LP01 (scalar model) and first order mode TE01 (vectorial models) / LP11 (scalar model).

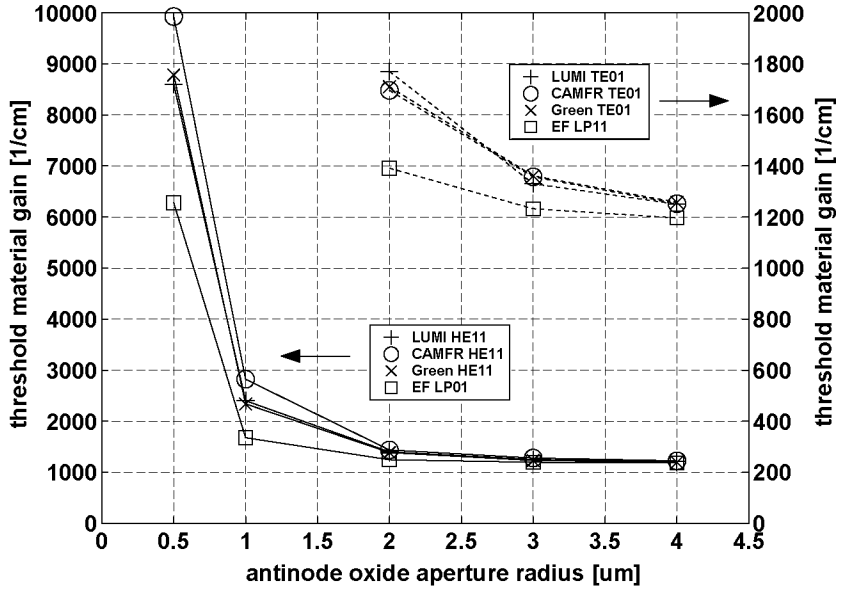

Figure 4.3: COST268 benchmark VCSEL structure. Threshold gain of the fundamental HE11 (vectorial models) / LP01 (scalar model) and first order mode TE01 (vectorial models) / LP11 (scalar model).

predicts too optimistic threshold gains for small oxide radii.

Note that computations with linear finite elements perform equally well for the threshold gain on the scale shown, but the resonance wavelength is offset to shorter wavelengths by approximately 2 nm. This corresponds to the 0.3% error predicted by Fig. 3.7 for the $30/\lambda$ discretisation with linear elements. Note that, in practice, this is not a severe limitation.

In the AlGaAs/GaAs material system, at a nominal wavelength of 980 nm, control within a monolayer corresponds to a layer thickness accuracy of ± 0.5 nm [3]. The refractive index n is 3.53 at this wavelength. Assuming no uncertainty in the Al content, this translates into a control over the optical length of ± 1.8 nm which corresponds to a relative accuracy of $\pm$ 0.2% with respect to the nominal wavelength. In reality, there is uncertainty in the Al content and the optical length can typically only be reproduced within $\pm 0.5\%$ at 980 nm. That is, the wavelength is expected to be accurate within ± 5 nm at 980 nm. Hence, linear elements or second order elements with a coarser mesh are sufficiently accurate for many applications.

It has to be emphasised at this point that the flexibility of the finite element method regarding the device structure comes at the price of a higher computational effort compared to the mode expansion method used in *CAMFR*. The latter is optimised to treat structures of the type shown in Fig. 4.1. In practice, it turns out that the additional flexibility is a requirement if different device types (Fig. 1.4) and device features have to be covered in a coupled electro-thermo-optical model.

4.1.2 Spontaneous Emission Enhancement in Microcavity

Spontaneous emission due to radiative recombination of an electron and a hole can be represented by the polarisation term $\boldsymbol{K}(\boldsymbol{r}, t)$ in Eq. (2.1), which is independent of the electric field. It enters the time domain Maxwell wave equation (2.4) on the right hand side and reappears as $\underline{\boldsymbol{F}}(\boldsymbol{r}, \omega)$ in the frequency domain Maxwell wave equation (2.20).

[3] The lattice constant of GaAs is 5.653 Å.

By applying an expansion similar to Eq. (2.6) to $\boldsymbol{K}(\boldsymbol{r},t)$

$$\underline{\boldsymbol{F}}(\boldsymbol{r},\omega) = \mu_0\omega^2\underline{\boldsymbol{K}}(\boldsymbol{r},\omega) \tag{4.1}$$

is obtained. Assume that the polarisation vector field is a point source with a certain direction. It turns out that for a given amplitude of $\underline{\boldsymbol{K}}(\boldsymbol{r},\omega)$ the optical power radiated by the point source is dependent on its environment. That is, the radiation power and, hence, the spontaneous emission rate can be enhanced or inhibited with respect to the situation in free space.

The matrix equation (3.27) is solved for a certain source distribution in order to simulate this effect. The LUMI result was verified for a point source between two PEC plates [106] in [107]. Here, the effect is demonstrated for the microcavity in Fig. 3.1 and a point source located on the symmetry axis in the active region. The modification of the power radiated relative to the situation without cavity is shown in Fig. 4.4 for part of the spectrum for vertical $g_v(\lambda)$ and horizontal polarisation $g_h(\lambda)$ of the point source. The refractive index for the space without the cavity is set to $n = 3.5$. The presence of the HE11 and HE12 modes have a noticeable effect on the radiation of the horizontally polarised source. The vertically polarised source remains almost unaffected. The radiated power is calculated by evaluating the expression for dissipated power Eq. (2.69) in the entire simulation domain.

The polarisation will normally be randomly oriented. Hence, due to the rotational symmetry of the device structure, a weighted average of the functions $g_v(\lambda)$ and $g_h(\lambda)$ [106]

$$g_{tot}(\lambda) = \frac{1}{3}g_v(\lambda) + \frac{2}{3}g_h(\lambda) \tag{4.2}$$

must be used.

It is evident from Fig. 4.4 that the procedure of sweeping the wavelength λ of a point source and recording the cavity response can be used to reliably find target values to initialise the JDQZ algorithm presented in Sec. 3.3.2. The target values can easily be identified as pronounced peaks in the modification of the radiated power. The separation into functions $g_h(\lambda)$ and $g_v(\lambda)$ is particularly useful since additional a priori knowledge on the direction of the radiation within the VCSEL cavity can be exploited.

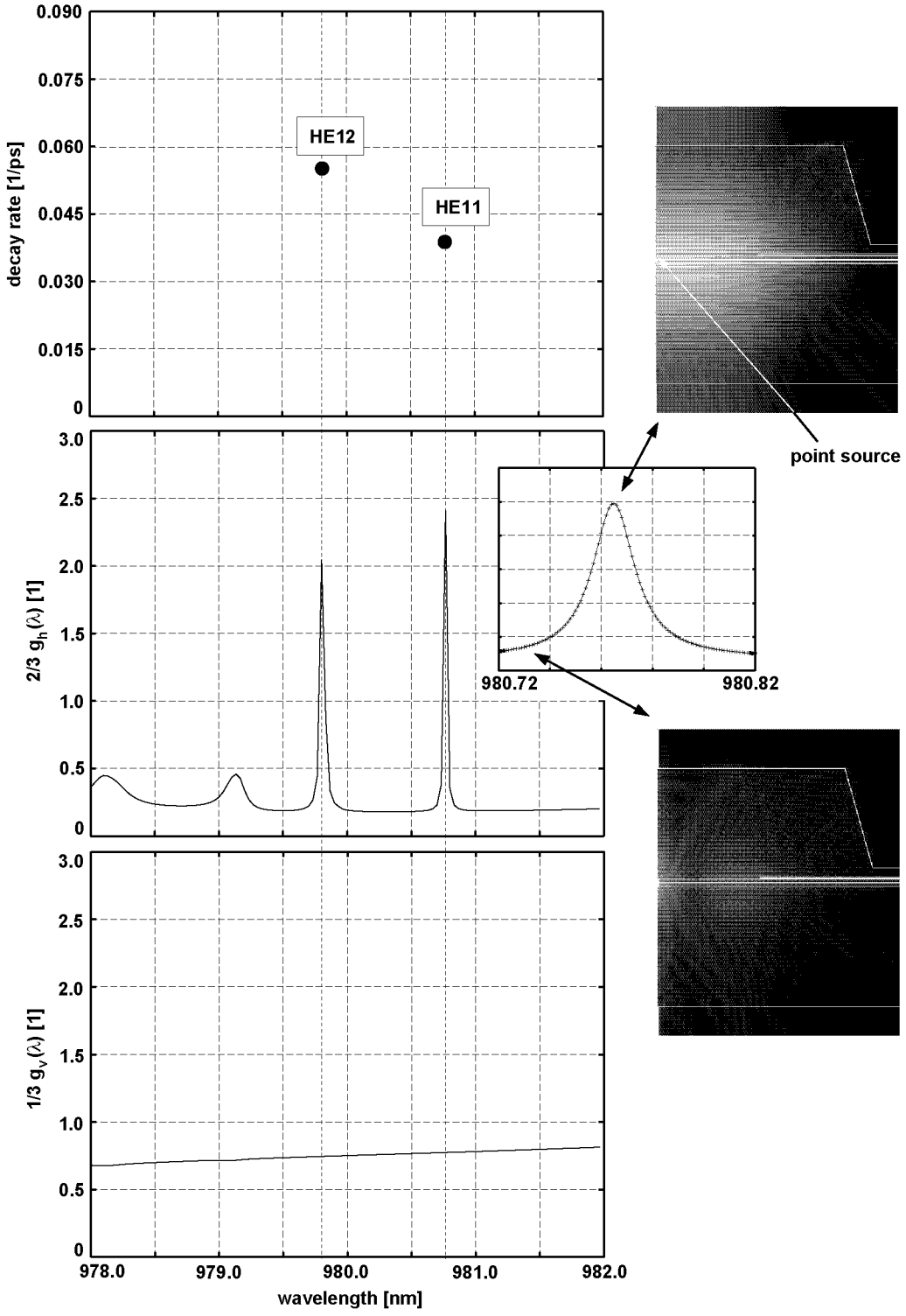

Figure 4.4: Relation between eigenvalues of modes and $g_h(\lambda)$, $g_v(\lambda)$. The reference refractive index is set to $n = 3.5$. Insets show magnification of $g_h(\lambda)$ close to the HE11 mode, and optical intensity on a logarithmic grey scale for enhanced and inhibited radiation from a horizontally polarised point source.

4.2 Calibrated VCSEL Simulation

The example is based on an AlGaAs/GaAs 840 nm narrow oxide-confined multi-quantum well (MQW) single mode VCSEL device structure. The top emitting VCSEL device has a λ cavity with an adjacent AlAs oxidation layer positioned in an optical field minimum. The oxide confinement has a diameter smaller than 4 μm. The top DBR stack is p doped and the bottom DBR stack n doped. At room temperature the MQW emission wavelength is 847.4 nm and the wavelength of the fundamental HE11 cavity mode is 840.7 nm. The two wavelengths coincide at a temperature of around 273 K. A device comparable to the one used here is given in [108] and [109].

The VCSEL achieves single mode operation by a narrow oxide aperture that causes additional diffractive losses. This effect is accurately rendered by the optical model employed in this work. The electro-thermal and optical equations are solved self-consistently and take into account the fundamental HE11 and first order TE01 mode. Figure 4.5 shows the evolution of the HE11 and TE01 modal gain and loss with respect to laser current. The modal loss of the TE01 mode decreases with increasing current because the evolving thermal lens pulls the mode towards the symmetry axis of the VCSEL and less power is absorbed in the annular top metal contact as a consequence. It follows that the correct threshold current for the first order mode can only be reproduced by a comprehensive self-consistently coupled model. In Figs. 4.6 and 4.7 excellent agreement between the simulated and measured DC terminal current, voltage, optical power, and wavelength characteristics is demonstrated over the specified operation range of the VCSEL. The simulation reproduces the threshold of the HE11 and TE01 modes at 0.40 mA and 1.75 mA that were determined from measurements of the emission spectrum versus drive current. The change in wavelength is due to the thermally induced change in the refractive index of the resonator material. The characteristic mode splitting is clearly visible and indicates valid thermal modeling of the VCSEL structure.

The electro-thermal model takes the first mirror pair of the DBR stacks on either side of the λ cavity into account in order to correctly model the carrier injection into the cladding region. The remaining portion of the DBR stacks is represented by a homogeneous region

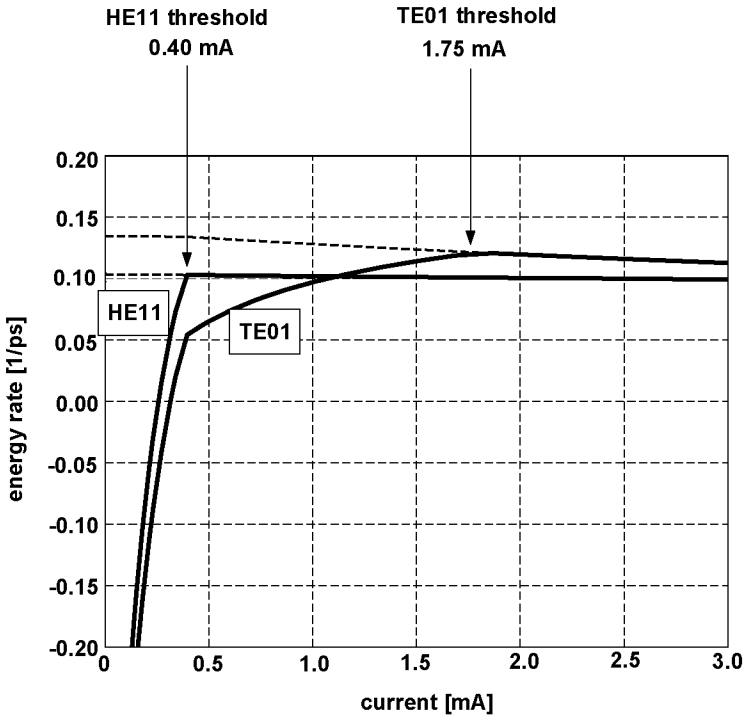

Figure 4.5: Simulation of modal gain (solid lines) and loss (dashed lines) of fundamental HE11 and first order TE01 optical modes versus terminal current

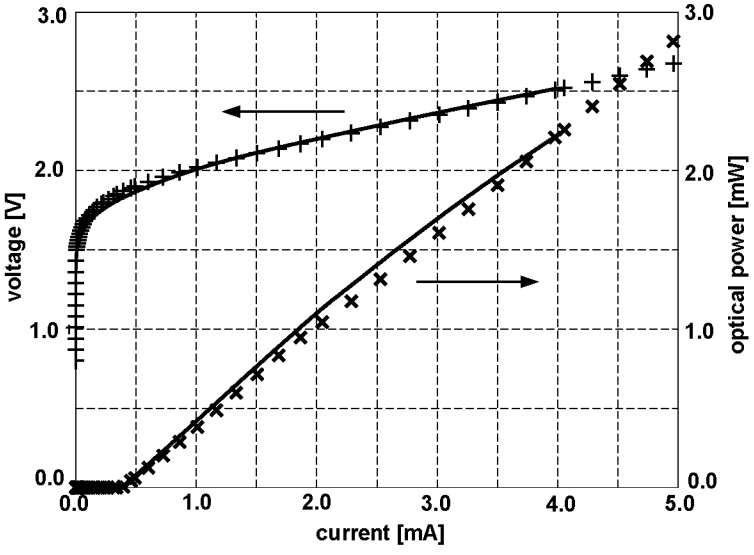

Figure 4.6: DC optical power and terminal voltage versus terminal current characteristics, measurements (solid lines), and simulation results (crosses).

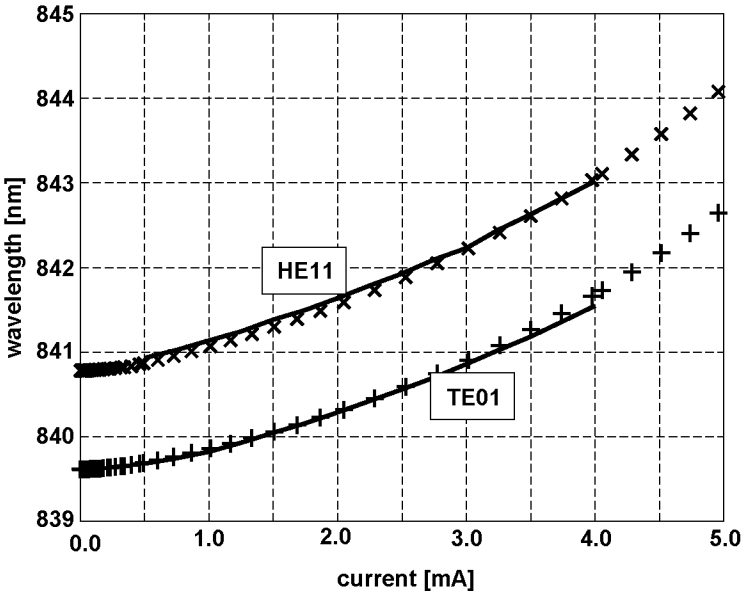

Figure 4.7: Wavelength tuning of fundamental HE11 first order and TE01 optical mode versus terminal current, measurements (solid lines), and simulation results (crosses).

using an effective carrier mobility. The simulator parameters that were used to perform the simulations in this example are listed in Tabs. 4.1, 4.2 and 4.3.

Table 4.1 summarizes the optical parameters. The real parts of the refractive indices n were obtained from the manufacturer of the device. The relative changes with temperature are taken from [110]. The imaginary part κ is a fitting parameter and is set to the given value only in the extrinsic regions of the DBR. It is set to zero in the intrinsic region.

In Tab. 4.2 the variable T is the local temperature in Kelvin, T_0 is 300 K, and N is the doping concentration in cm^{-3}. Bandgap shrinkage due to temperature is only accounted for in the QW regions. The QW electron and hole mobilities are set equal to the bulk carrier mobilities in GaAs [111].

The imaginary part of the complex refractive index in Tab. 4.1, the SRH, Auger recombination parameters and the DBR electron and hole mobilities in Tab. 4.2 were used to match simulated and measured results in Figs. 4.6 and 4.7.

The VCSEL structure is discretised with 14'526 finite elements

x	$n + i\kappa$ (extrinsic)	$n + i\kappa$ (intrinsic)	$\frac{1}{n}\frac{dn}{dT}$ K^{-1}
0.000	$3.644 + i \cdot 1.500 \cdot 10^{-5}$	$3.644 + i \cdot 0.000$	$2.000 \cdot 10^{-4}$
0.200	$3.477 + i \cdot 1.500 \cdot 10^{-5}$	$3.477 + i \cdot 0.000$	$1.900 \cdot 10^{-4}$
0.300	$3.405 + i \cdot 1.500 \cdot 10^{-5}$	$3.405 + i \cdot 0.000$	$1.700 \cdot 10^{-4}$
0.600	$3.214 + i \cdot 1.500 \cdot 10^{-5}$	$3.214 + i \cdot 0.000$	$1.600 \cdot 10^{-4}$
0.900	$3.044 + i \cdot 1.500 \cdot 10^{-5}$	$3.044 + i \cdot 0.000$	$1.400 \cdot 10^{-4}$
1.000	$2.990 + i \cdot 1.500 \cdot 10^{-5}$	$2.990 + i \cdot 0.000$	$1.250 \cdot 10^{-4}$

Table 4.1: Optical parameters for simulation of $Al_xGa_{1-x}As$ at 840 nm used in the simulation.

bandgap:			
$x < 0.45$ (dir.)	$1.424 + 1.247 \cdot x$	eV	[111]
$x \geq 0.45$ (ind.)	$1.900 + 1.250 \cdot x + 0.143 \cdot x^2$	eV	[111]
shrinkage ΔE_g	$-5.5 \cdot 10^{-4} \frac{1}{K} \frac{T^2}{225\text{K}+T}$	eV	[111]
eff. masses:			
electron	$\frac{m_{el}}{m_0} = 0.067 + 0.083 \cdot x$	1	[26]
heavy hole	$\frac{m_{hh}}{m_0} = 0.500 + 0.290 \cdot x$	1	[26]
light hole	$\frac{m_{lh}}{m_0} = 0.087 + 0.063 \cdot x$	1	[26]
mobility:			
electron (DBR)	740	$\text{cm}^2\text{V}^{-1}\text{s}^{-1}$	-
hole (DBR)	37	$\text{cm}^2\text{V}^{-1}\text{s}^{-1}$	-
electron (QW)	8000	$\text{cm}^2\text{V}^{-1}\text{s}^{-1}$	-
hole (QW)	400	$\text{cm}^2\text{V}^{-1}\text{s}^{-1}$	-
QW capture	$\tau_{qw,e} = \tau_{qw,h} = 1$	ps	[17]
SRH	$\tau_{srh,e} = \tau_{srh,h} = \frac{100}{1+\frac{N}{10^{16}cm^{-3}}}$	ns	-
Auger (electrons)	$\left(0.19 + 1000.0\frac{T}{T_0}\right) \cdot 10^{-30}$	cm^6s^{-1}	-
Auger (holes)	$\left(1.2 + 1000.0\frac{T}{T_0}\right) \cdot 10^{-30}$	cm^6s^{-1}	-
thermal:			
cond. (bulk)	$0.44 - 1.79 \cdot x + 2.26 \cdot x^2$	$\text{W K}^{-1}\text{cm}^{-1}$	[111]
cond. (DBR)	0.11	$\text{W K}^{-1}\text{cm}^{-1}$	[14]
capacity	1.6	$\text{W K}^{-1}\text{cm}^{-1}$	[111]

Table 4.2: Electro-thermal parameters of $Al_xGa_{1-x}As$ used in the simulation. Last column shows references.

ambient temperature	300	K	-
thermal contact surface resistances:			
top contact	$2.7 \cdot 10^{-6}$	$\text{K cm}^2\text{W}^{-1}$	-
bottom contact	$2.7 \cdot 10^{-6}$	$\text{K cm}^2\text{W}^{-1}$	-
electrical contact resistances:			
top contact	1	Ω	-
bottom contact	1	Ω	-

Table 4.3: Thermal and electrical terminal parameters.

for the electro-thermal mesh and 93'545 finite elements for the optical mesh. For the presented multi-mode computation 4.5 GBytes of memory are required. Calculating the 60 bias points shown in Fig. 4.6 self-consistently takes approximately 9 hours. In this case approximately 200 'Newton + optical mode solve steps' have to be performed. On average, a Newton step takes around 2 minutes and an optical solve step around 30 seconds. The latter takes less time than stated in Sec. 4.1.1 due to the continuation scheme and the preconditioner re-cycling employed (Sec. 3.3.3).

4.3 VCSEL Small Signal Modulation Response

Figure 4.8 shows the small signal modulation amplitude and phase response of the device shown in Figs. 3.1 and 3.2 at different bias currents. The modulation response is shown for the fundamental HE11 optical mode. The VCSEL structure has a thin oxide aperture with $r_{ox} = 2$ μm at a field node position. The AlGaAs/GaAs material system is employed with InGaAs quantum wells that emit at 980 nm. Section 4.4 provides a detailed discussion of the device structure[4]. Its current versus optical power characteristic is given in Fig 4.22.

All modulation responses show high damping behaviour even for currents as low as 1.3 mA due to the parasitic effect of the thin oxide aperture and damping effects caused by a decrease in differential gain. The general behaviour is essentially given by a second-order low-pass response with a 40 dB per decade roll-off at the resonance frequency. The 3dB cut off frequencies are at 3 GHz, 5 GHz, and 6 GHz, respectively.

[4]Note that the device structure is not optimised for high modulation bandwidth.

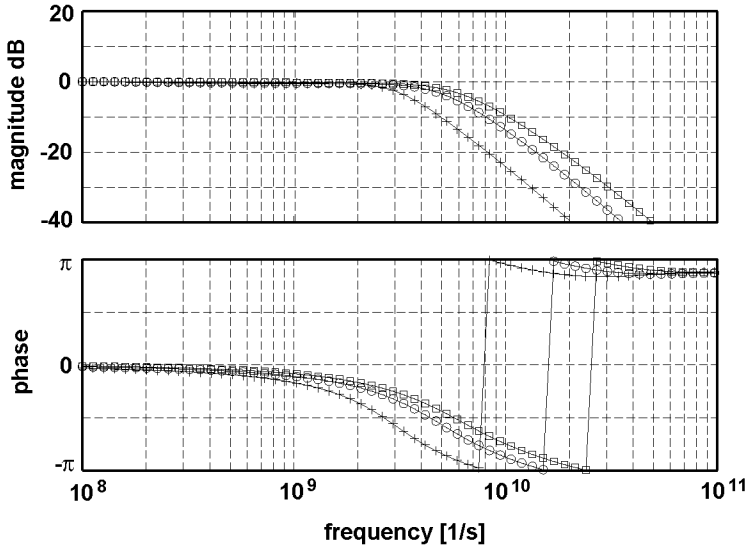

Figure 4.8: Small signal modulation amplitude and phase response at different bias currents: 1.3 mA +, 2.9 mA ∘, 5.7 mA □.

4.4 Optimising a VCSEL for Maximum Single Mode Power

Single mode control is an important aspect in VCSEL design for a wide range of applications. For instance, in order to minimise the pulse dispersion in a fibre optic link, it is desirable to keep the spectrum of the laser emission as narrow as possible and, therefore, to restrict the emission ideally to a single mode at a given optical power level. Sensing applications constitute an additional field where single mode control is essential. Pure single mode operation is needed in this case to achieve ultimate spectral detection resolution.

Section 4.4.1 gives a detailed description of the VCSEL structure and the design parameters in question. Two design concepts that are expected to enhance the single mode behaviour of the VCSEL are described: one of them uses a metallic absorber and the other employs an anti-resonant structure. The effectiveness of both metallic absorber and anti-resonant structure is significantly compromised by an intricate interplay of electronic, thermal and optical effects. In conclusion, the proposed design task can only be handled by a 2D model that takes these effects into account in a self-consistent manner.

	thickness [nm]	material	
air		air	
28 period DBR	69.49	GaAs	
	79.63	$Al_{0.8}Ga_{0.2}As$	
oxide aperture	69.49	GaAs	
	49.63-x	$Al_{0.8}Ga_{0.2}As$	
	30.00	AlAs	$r < r_{ox}$
	30.00	Al_2O_3	$r > r_{ox}$
	x	$Al_{0.8}Ga_{0.2}As$	
λ cavity	136.49	GaAs	
	8.00	$In_{0.20}Ga_{0.80}As$	
	136.49	GaAs	
31.5 period DBR	69.49	$Al_{0.8}Ga_{0.2}As$	
	79.63	GaAs	
substrate		GaAs	

position	x
1	49.63
2	33.09
3	16.54
4	0.00

Table 4.4: Material composition and thicknesses of epitaxial layers in basic VCSEL device structure.

The two device concepts are investigated and compared in Sec. 4.4.2.

4.4.1 VCSEL Device Structure

The device structure that will be investigated is based on the same VCSEL benchmark [35] that was already presented in Sec. 4.1.1. Since this is a purely optical benchmark it had to be augmented by additional electronic specifications.

The structure is detailed in Fig. 4.9 and Tab. 4.4. The VCSEL is designed in the AlGaAs/GaAs material system with an InGaAs active region that emits at 980 nm. It is an etched mesa structure with an Al_2O_3 aperture. The λ cavity at the centre of the device is enclosed with a bottom $\lambda/4$ DBR with 31.5 mirror pairs and a top DBR with 28 mirror pairs. A 30 nm thick AlAs layer can be placed in 4 different positions in the vertical direction inside the $\lambda/4$ layer in the top DBR closest to the cavity (see bottom inset in Fig. 4.9). This AlAs layer can be oxidized to an arbitrary lateral depth. In this way a low refractive index, insulating aperture for both the optical field and the electrical current is formed. The active region is given by

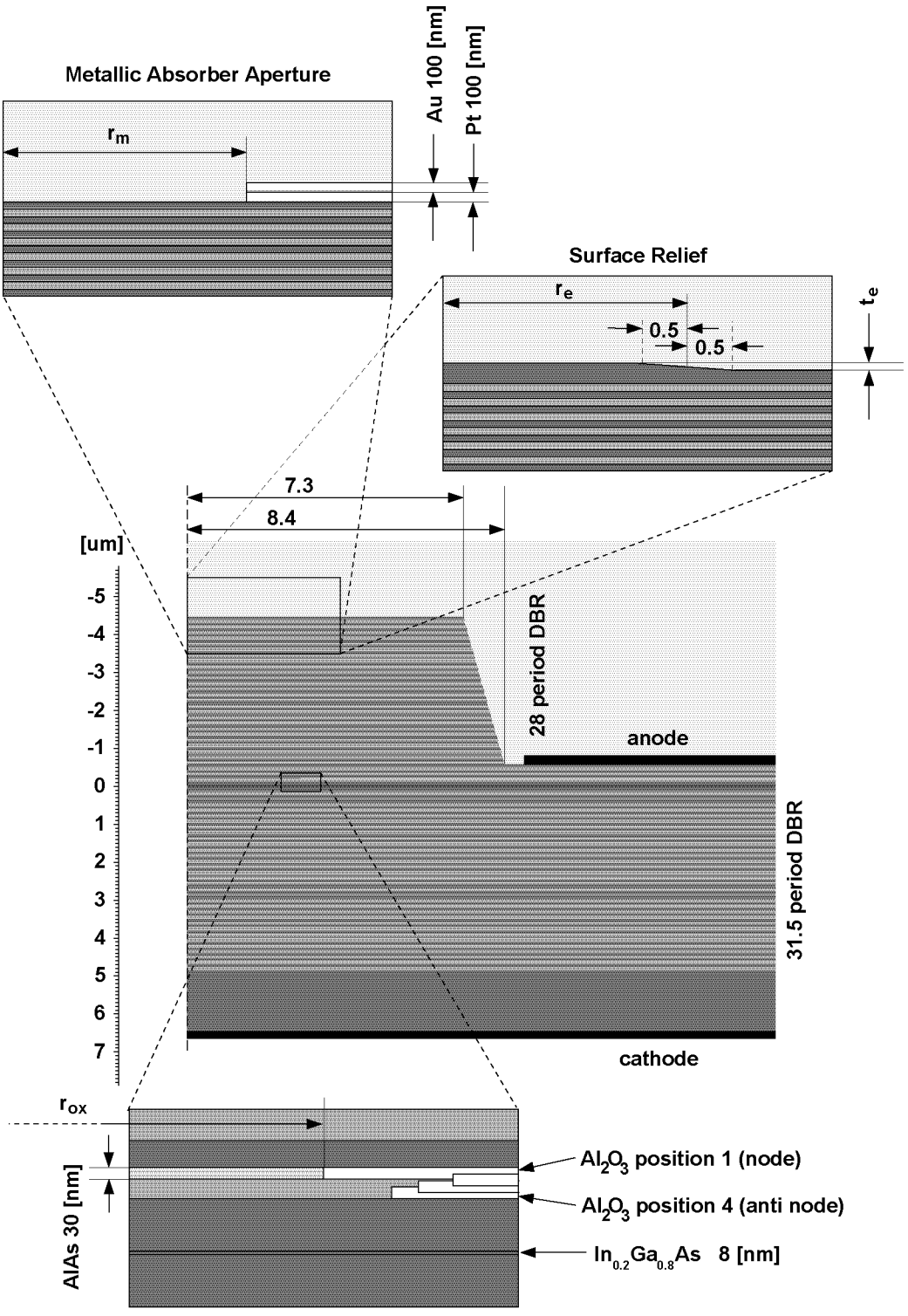

Figure 4.9: VCSEL device structure. Insets show Al_2O_3 aperture geometry, metallic absorber and surface relief option for optical resonator. Dimensions are in μm if not stated otherwise.

a single strained $In_{0.20}Ga_{0.80}As$ 8 nm thick quantum well embedded in GaAs barriers at the centre of the λ cavity. The anode side is connected with an intra-cavity contact. The top DBR can therefore be left undoped and the free carrier absorption kept to a minimum. The intrinsic region is assumed p-doped at 10^{17} cm^{-3}. The current spreading layer next to the anode is p-doped with $2 \cdot 10^{18}$ cm^{-3} and the cathode side n-doped with $2 \cdot 10^{18}$ cm^{-3}.

Two variants of the basic VCSEL structure described above will be investigated in Sec. 4.4.2. One variant has a metallic absorber composed of 100 nm Pt and 100 nm Au placed on top of the anode side DBR. The metallic absorber has an aperture with a given radius. In the other variant the top layer of the anode DBR stack is $3\lambda/4$ thick instead of the original $\lambda/4$. A surface relief is etched into the top layer. This forms an off-centre anti-resonant structure outside a given radius. The thicker top layer is used to accommodate the surface relief without exposing any aluminium containing layers to air. This would lead to the formation of an unwanted oxide layer and deteriorate the optical properties of the anti-resonant structure.

The following design parameters will be varied in the course of finding a device structure with maximum single mode power:

- vertical position and radius r_{ox} of Al_2O_3 aperture
- radius of aperture r_m in metallic absorber
- depth t_e and radius r_e of surface relief

4.4.2 Design Tutorial

Simulations of the device structure shown in Fig. 4.9 are performed using the VCSEL simulator and the results discussed. The tutorial is arranged step by step. First, the properties of the cold cavity optical resonator are investigated in detail. The effect of the position of the oxide aperture in the cavity is analysed. Building onto this basic structure, the effect of two different design concepts aiming at enhancing the single mode behaviour of the original device are assessed. The first concept uses a metallic absorber and the second one an integrated anti-resonant structure. Once some familiarity has been reached with the cold cavity problem, the performance of the different approaches

are compared in a self-consistently coupled electro-thermo-optical simulation.

Single Mode Control in VCSEL Devices

Two basic categories of single mode control strategies can be distinguished. The first category comprises methods that employ some sort of lateral optical guide to cut off higher order modes. Methods of the second category introduce mode-selective loss or gain by integrating filter structures in the resonant cavity.

Methods belonging to the first category are based on the fact that the existence of higher order modes depends critically on the lateral geometrical dimensions of the optical guide. For example, VCSEL devices with oxide apertures below a critical radius will operate in the fundamental HE11 mode and will no longer support higher order modes. Unfortunately, rather narrow oxide apertures are required for this, increasing the electrical resistance of the device. As a consequence, the maximum single mode output power is often limited by the increased heating. Additionally, narrow oxide apertures are a device reliability hazard and can cause significant optical scattering losses with respect to the total optical losses of the cavity.

The second category introduces some kind of integrated mode-selective filtering. Several approaches have been described early in, for instance, [112] and more recently in [113, 114, 115]. This approach relaxes the requirements with respect to the lateral mode confinement. That is, larger oxide apertures can be used and therefore higher laser currents without causing excessive heating. One idea is to tailor the current injection in such a way that the radial optical gain profile is restricted to a small region at the centre of the device where the fundamental mode sits. A method to direct current injection is proton implantation. The other approach is based on deliberately introducing losses to higher order modes. This can easily be done by using ring shaped metallic absorber apertures. As the fundamental mode is the only one with its optical intensity confined to the centre of the device, it will experience less absorption in the metal than all other higher order modes. Firstly, this leads to increased losses for the unwanted modes, and secondly to some screening of radiation coming from higher order modes once they turn on. An even more efficient

technique introduces a relief by etching the top surface of the optical resonator. By choosing the depth of this relief appropriately higher order modes can be made to reflect out-of-phase from the etched semiconductor air interface. In this way losses for higher order modes can be increased substantially.

VCSEL Optical Modes

The properties of the cold cavity optical resonator are investigated in detail. Numerical experiments comparing results for different mesh densities using second order finite elements and verification with other methods [103] suggest that the error in the results shown in Figs. 4.10-4.13 lies within ± 0.2 nm for the wavelength and ± 1% for the quality factor. The quality factor is defined as [44]

$$Q_k = \frac{\omega_k'}{2\omega_k''} \tag{4.3}$$

where ω_k' is the angular velocity and $2\omega_k''$ is the modal rate of change of the electromagnetic energy in mode k.

Figures 4.10 and 4.11 show an analysis of the effect of the vertical and lateral oxide aperture position on the wavelength and the quality factor of the fundamental HE11 and the first order TE01 optical mode. The optical simulation parameters assuming $T_0 = 300$ K, are summarized in Tab. 4.5 and will be used throughout the entire tutorial section. The intracavity contact design allows the anode side mirror to be left undoped. Negligible absorption is therefore assumed in the optical resonator material, except for the active and the metal absorber regions. Optical gain and absorption in the active region will be calculated and taken into account in the coupled electro-thermo-optical simulation and are not considered in this section.

If the oxide aperture is moved from the node position, where the electric field has an intensity minimum, to the antinode position, where it has a maximum, the quality factor decreases sharply for apertures with a small radius. For apertures with a large radius the quality factor remains almost the same and only the wavelength shifts to lower values. The strong decrease in the quality factor for apertures at or close to the antinode position is caused by the rapid increase of

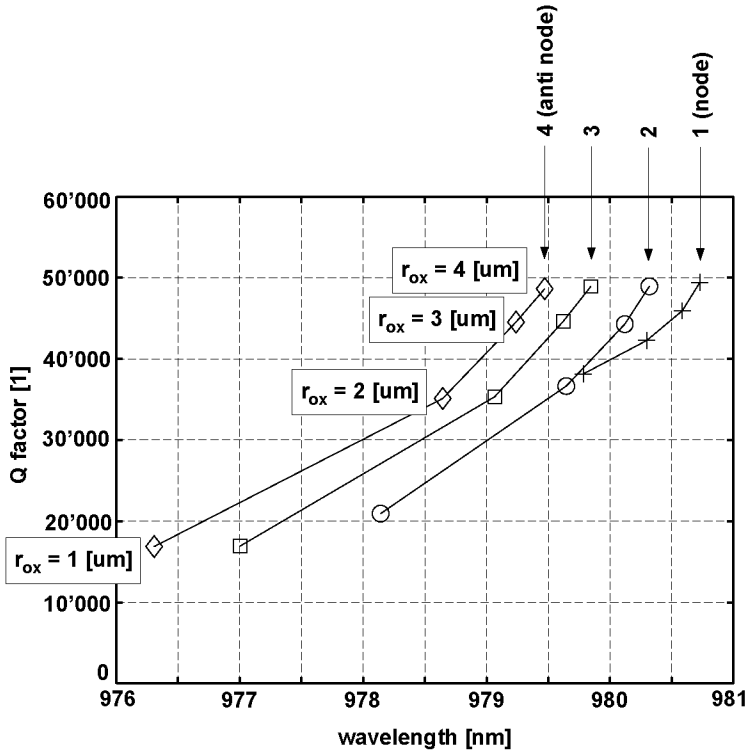

Figure 4.10: Wavelengths and quality factors for HE11 mode. Values are plotted for different oxide aperture radii r_{ox} and different oxide aperture positions: position 1 $+$, position 2 $\circ$, position 3 $\square$, position 4 $\diamond$.

material	$n + i\kappa$	α_n K^{-1}
air	1.0	0.0
Au	$0.20 + i5.50$	0.0
Pt	$2.99 + i5.17$	0.0
GaAs	3.53	$2.0 \cdot 10^{-4}$
$Al_{0.8}Ga_{0.2}As$	3.08	$2.0 \cdot 10^{-4}$
AlAs	2.95	$1.2 \cdot 10^{-4}$
Al_2O_3	1.60	0.0
$In_{0.20}Ga_{0.80}As$	3.82	$2.0 \cdot 10^{-4}$

Table 4.5: Complex refractive indices and temperature coefficients.

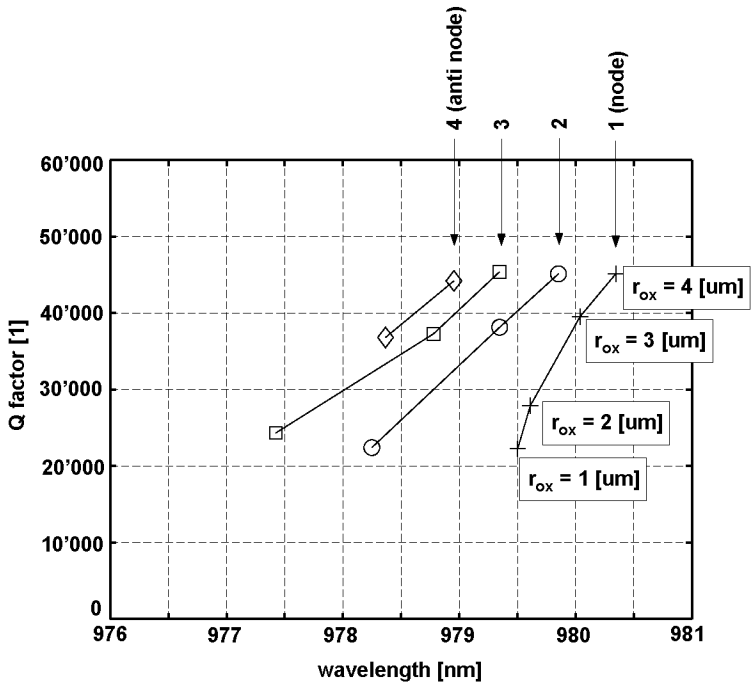

Figure 4.11: Wavelengths and quality factors for TE01 mode. Values are plotted for different oxide aperture radii r_{ox} and different oxide aperture positions: position 1 +, position 2 $\circ$, position 3 $\square$, position 4 $\diamond$. Please note that TE01 modes are cut off for oxide apertures with $r_{ox} = 1$ μm at positions 2 and 3, and furthermore for $r_{ox} = 1$ μm, 2 μm at position 4.

scattering losses that the optical field experiences for narrow aperture radii.

The strong confinement exerted by such an aperture even leads to cutting off the TE01 mode in some cases, as shown in Fig. 4.11. This effect can, in fact, be used to obtain single mode operation of a VCSEL device. However, this approach is usually compromised by excessive heating caused by current flow through a narrow aperture. Additionally, narrow antinode apertures cause excessive optical losses and hence results in VCSEL devices with high threshold currents and poor efficiency. The remainder of this tutorial will therefore focus on oxide apertures in the node position, which is the technologically relevant case.

Similarly, the properties of the enhancements to the original design are investigated. The geometry of the two variants, metallic absorber and integrated anti-resonant structure, is described in Fig. 4.9. Figures 4.12-4.15 show the effect of varying the radius of the oxide aperture versus either the radius of the metal aperture or the radius of the edge of the surface relief. For reference, data of the original structure with an oxide aperture at position 1 (node) is also shown.

The key feature is that the quality factor not only decreases for narrow oxide apertures, as was the case in the original structure, but also for larger apertures from a certain radius onwards. This is due to the additional loss caused by either increased absorption in the metal or out-of-phase reflection from the etched semiconductor air interface for part of the optical mode. The affected portion of the optical mode is determined by the lateral extent of the structure causing that loss. Therefore, as the radii r_m (metallic absorber) and r_e (anti-resonant structure) are decreased the effect becomes more pronounced. However, decreasing r_m and r_e causes the quality factor to decrease in general. Furthermore, the anti-resonant structure has the stronger effect than the metallic absorber.

For the cold cavity an interesting figure of merit is the relative difference between the quality factors of the HE11 and TE01 optical modes. Maximising this figure will yield a device structure that exhibits maximal discrimination between HE11 and TE01 optical modes.

Although investigating the cold cavity is a necessary initial design task to be carried out, it is by no means sufficient to optimise a VCSEL structure for maximum single mode power emission because it

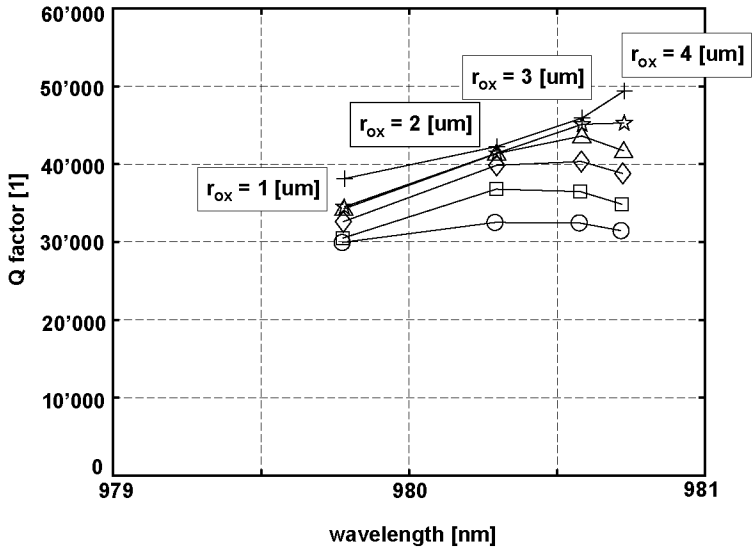

Figure 4.12: Wavelengths and quality factors for HE11 mode for an oxide aperture at position 1 (node). Values are plotted for different oxide aperture radii r_{ox} versus radii r_m of the metallic absorber: original structure + (no metallic absorber), $r_m = 1.5$ μm $\circ$, $r_m = 2.0$ μm $\square$, $r_m = 2.5$ μm $\diamond$, $r_m = 3.0$ μm $\triangle$, $r_m = 3.5$ μm $\star$.

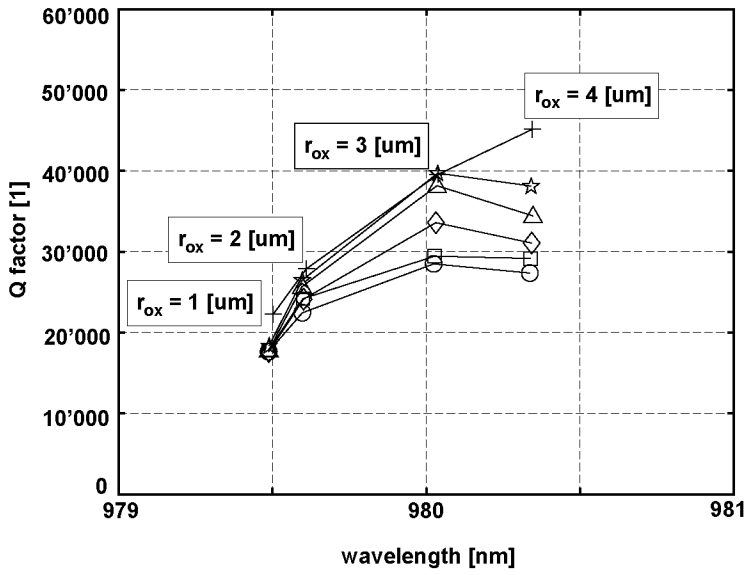

Figure 4.13: Wavelengths and quality factors for TE01 mode. Oxide aperture at position 1 (node). Values are plotted for different oxide aperture radii r_{ox} versus radii r_m of the metallic absorber: original structure + (no metallic absorber), $r_m = 1.5$ μm $\circ$, $r_m = 2.0$ μm $\square$, $r_m = 2.5$ μm $\diamond$, $r_m = 3.0$ μm $\triangle$, $r_m = 3.5$ μm $\star$.

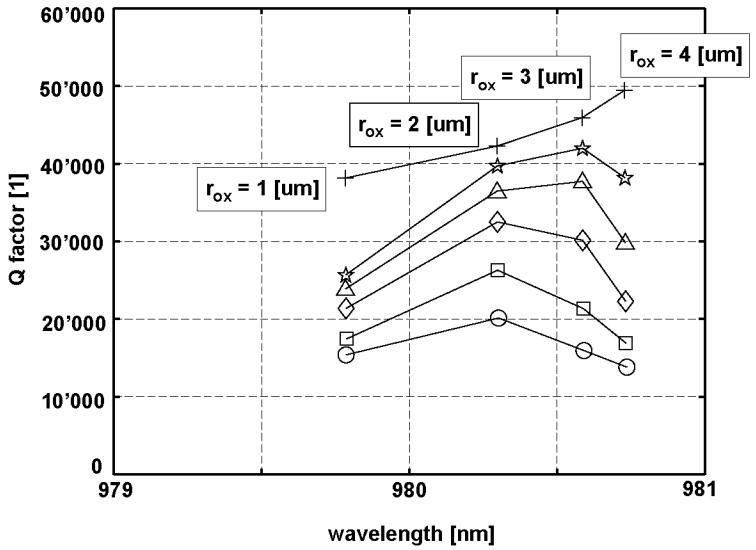

Figure 4.14: Wavelengths and quality factors for HE11 mode. Oxide aperture at position 1 (node). Values are plotted for different oxide aperture radii r_{ox} versus radii r_e of the surface relief: original structure $+$ (no surface relief), $r_e = 1.5$ μm $\circ$, $r_e = 2.0$ μm $\square$, $r_e = 2.5$ μm $\diamond$, $r_e = 3.0$ μm $\triangle$, $r_e = 3.5$ μm $\star$.

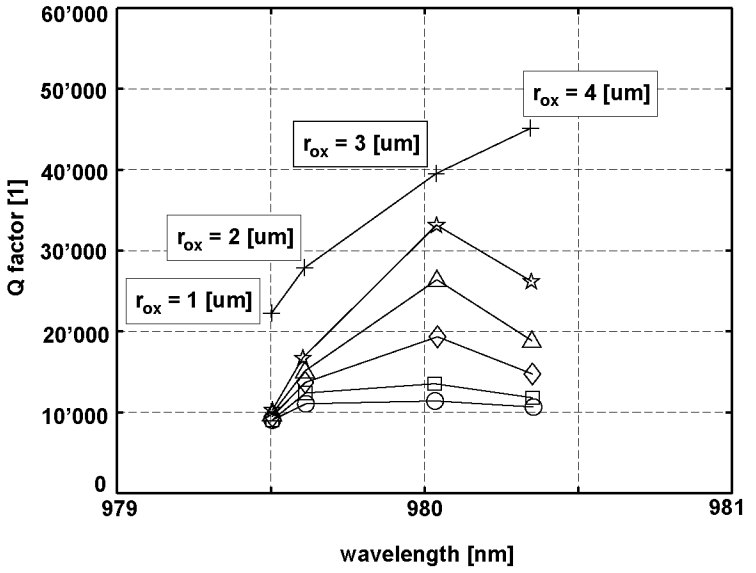

Figure 4.15: Wavelengths and quality factors for TE01 mode. Oxide aperture at position 1 (node). Values are plotted for different oxide aperture radii r_{ox} versus radii r_e of the surface relief: original structure $+$ (no surface relief), $r_e = 1.5$ μm $\circ$, $r_e = 2.0$ μm $\square$, $r_e = 2.5$ μm $\diamond$, $r_e = 3.0$ μm $\triangle$, $r_e = 3.5$ μm $\star$.

neglects the interplay between electronic, thermal, and optical effects. In principle, the entire parameter space would have to be scanned by coupled electro-thermo-optical simulations. However, in order to keep the problem manageable within the framework of this tutorial the design task will focus on finding an optimum radius r_{ox} of the oxide aperture for a given geometry of the anti-resonant structure and metallic absorber. This is an interesting exercise because, by changing the radius of the aperture, the temperature and optical gain profiles and therefore the interaction between electronic, thermal, and optical effects can be adjusted. The nominal radius of the oxide aperture is set at $r_{ox} = 4.0$ μm for additional cold cavity simulations that were performed to determine r_e and t_e for the surface relief and r_m for the metallic absorber. The relative difference between the quality factors of the HE11 and TE01 optical modes was maximised for r_m and r_e between 2.5 μm and 3.5 μm and a depth t_e of 72 nm. In the following, r_m of the metallic absorber will be set to 2.5 μm and $r_e = 2.5$ μm, $t_e = 72$ nm will be chosen for the surface relief. The values for r_e and r_m are deliberately set to values at the lower end of the range obtained from the cold cavity simulations since this is expected to approximately compensate the shift of the optical mode profiles towards the symmetry axis of the VCSEL device due to thermal lensing.

Figure 4.16 compares the discrimination between HE11 and TE01 optical modes for the basic VCSEL structure and the enhanced variants versus the radius r_{ox} of the oxide aperture. In Fig. 4.17 the HE11 output coupling efficiency is shown for the same parameter variation. The output coupling efficiency describes the optical power radiated through the top of the VCSEL structure with respect to the total optical loss of the resonator comprising material and radiation loss. An output coupling efficiency of 1.0 would correspond to the ideal case in which all optical power generated would be coupled through the top of the VCSEL device.

Figure 4.16 shows that the anti-resonant structure provides the stronger enhancement of the mode discrimination than the metallic absorber. The latter is only slightly superior to the enhancement the basic structure provides already. Moreover, in all cases a maximum mode discrimination is achieved for an r_{ox} between 1.0 μm and 2.0 μm. In Fig. 4.17 it can be seen that for the basic structure a larger radius r_{ox} leads to less scattering losses and, therefore, to a higher output

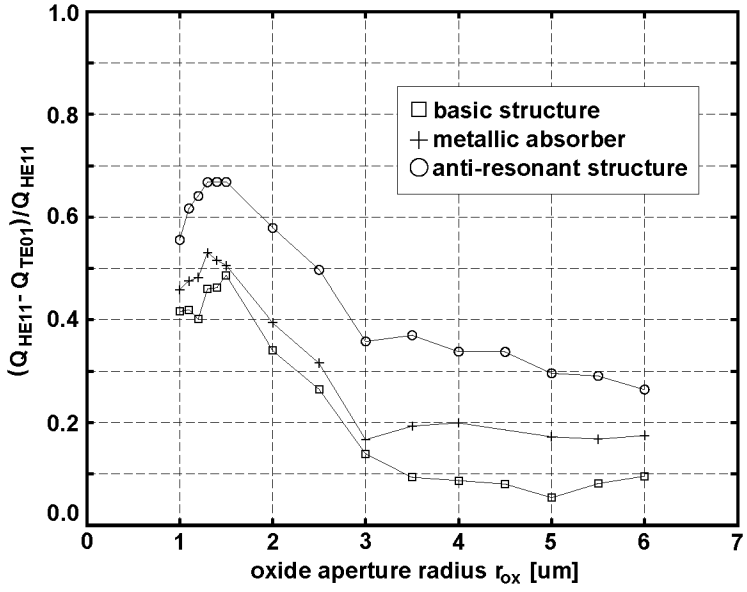

Figure 4.16: Relative difference between the quality factors of the HE11 and TE01 optical modes for the basic VCSEL structure and the enhanced structures with surface relief and metallic absorber.

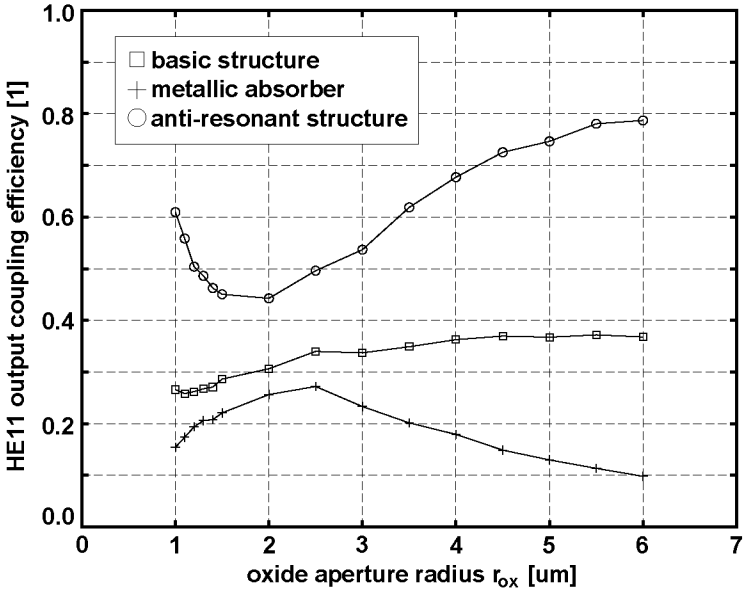

Figure 4.17: Output coupling efficiency for the basic VCSEL structure and the enhanced structures with surface relief and metallic absorber.

coupling efficiency. Figure 4.17 also reveals the main disadvantage of the metallic absorber: the output coupling efficiency is lower than in the other two variants due to the screening effect that the metal layer exhibits. The HE11 mode is increasingly affected for $r_{ox} > 2.5$ μm. Compared to the basic structure for narrow r_{ox} some scattered light that is normally radiated through the top is also absorbed by the metal layer. The anti-resonant structure shows the opposite behaviour. The larger r_{ox} the higher the output coupling efficiency. Furthermore, for narrow r_{ox} an increase in efficiency is observed.

In the subsequent coupled electro-thermo-optical simulations it is expected that device structures that offer the best compromise between mode discrimination and output coupling efficiency will be candidates for maximum single mode power emission.

Coupled Electro-Thermo-Optical Simulation

The parameters used for the coupled electro-thermo-optical simulations are summarized in Tabs. 4.5, 4.6, 4.7 and 4.8.

Figure 4.18 shows the simulation results for a VCSEL structure with surface relief and $r_{ox} = 3$ μm. The roll-over at high currents is mainly caused by increased Auger recombination as a consequence of self-heating. The curves marked with circles are from a self-consistent electro-thermo-optical simulation. The emission is single mode up to a current of 11.5 mA when the TE01 mode starts to lase. If the optical problem is not solved self-consistently, but is only computed once at the beginning of a simulation run, the curves marked with crosses are obtained. In this case the VCSEL device remains single mode over the entire operation range.

The reason for the difference in the two results can be gathered from Fig. 4.19. The modal optical gain contributed by the active region and the loss (radiation and material loss) contributed by the remaining optical resonator are plotted for the HE11 and the TE01 mode. The self-consistent result is shown at the top of Fig. 4.19 and the non-self-consistent one at the bottom.

For each mode the modal gain generated by the active region rises up to the point where it compensates the loss of the remaining optical resonator. At this point the corresponding mode starts to lase. Clearly, heating effects lead to a perturbation of the optical problem

$Al_xGa_{1-x}As$			
bandgap:			
E_g $x < 0.45$ (dir.)	$1.424 + 1.247 \cdot x$	eV	[111]
E_g $x \geq 0.45$ (ind.)	$1.900 + 1.250 \cdot x + 0.143 \cdot x^2$	eV	[111]
shrinkage ΔE_g	$-5.5 \cdot 10^{-4} \frac{1}{K} \frac{T^2}{204K+T}$	eV	[111]
eff. masses:			
electron	$\frac{m_{el}}{m_0} = 0.067 + 0.083 \cdot x$	1	[26]
heavy hole	$\frac{m_{hh}}{m_0} = 0.500 + 0.290 \cdot x$	1	[26]
light hole	$\frac{m_{lh}}{m_0} = 0.087 + 0.063 \cdot x$	1	[26]
mobility:			
electron (bulk)	$8500 - 6000 \cdot x$	$cm^2V^{-1}s^{-1}$	[111]
hole (bulk)	$400 - 250 \cdot x$	$cm^2V^{-1}s^{-1}$	[111]
electron (DBR)	3000	$cm^2V^{-1}s^{-1}$	-
hole (DBR)	140	$cm^2V^{-1}s^{-1}$	-
SRH	$\tau_{srh,e} = \tau_{srh,h} = \frac{10}{1+\frac{N}{10^{16}cm^{-3}}}$	ns	-
Auger (electrons)	$A_n = 1.0 \cdot 10^{-30}$,	cm^6s^{-1}	-
	$B_n^{(1)} = 0$, $B_n^{(2)} = 0$	cm^6s^{-1}	-
Auger (holes)	$A_p = 1.0 \cdot 10^{-30}$,	cm^6s^{-1}	-
	$B_p^{(1)} = 0$, $B_p^{(2)} = 0$	cm^6s^{-1}	-
thermal :			
conductivity (bulk)	$0.44 - 1.79 \cdot x + 2.26 \cdot x^2$	W $K^{-1}cm^{-1}$	[111]
conductivity (DBR)	0.11	W $K^{-1}cm^{-1}$	[14]

Table 4.6: Parameters for $Al_xGa_{1-x}As$. Last column shows reference.

$In_{0.2}Ga_{0.8}As$ (QW active region)			
bandgap:			
E_g	1.200	eV	[116]
shrinkage ΔE_g	$-5.0 \cdot 10^{-4} \frac{1}{K} \frac{T^2}{53K+T}$	eV	[116]
eff. masses:			
electron	$\frac{m_{el}}{m_0} = 0.063$	1	[117]
heavy hole	$\frac{m_{hh}}{m_0} = 0.500$	1	[117]
light hole	$\frac{m_{lh}}{m_0} = 0.074$	1	[117]
linewidth broadening	$\Gamma = 0.020$	eV	-
mobility:			
electron (QW)	7000	$cm^2V^{-1}s^{-1}$	-
hole (QW)	325	$cm^2V^{-1}s^{-1}$	-
carrier scattering:			
QW capture	$\tau_{qw,e} = \tau_{qw,h} = 1$	ps	[17]
SRH	$\tau_{srh,e} = \tau_{srh,h} = \frac{1000}{1+\frac{N}{10^{16}cm^{-3}}}$	ns	-
Auger (electrons)	$A_n = 3.0 \cdot 10^{-28}$,	cm^6s^{-1}	-
	$B_n^{(1)} = 0$, $B_n^{(2)} = 3.0 \cdot 10^{-28}$	cm^6s^{-1}	-
Auger (holes)	$A_p = 3.0 \cdot 10^{-28}$,	cm^6s^{-1}	-
	$B_p^{(1)} = 0$, $B_p^{(2)} = 3.0 \cdot 10^{-28}$	cm^6s^{-1}	-
thermal conductivity	0.4	W $K^{-1}cm^{-1}$	[111]

Table 4.7: Parameters for $In_{0.2}Ga_{0.8}As$. Last column shows reference.

ambient temperature	300	K	-
thermal contact surface resistances:			
top contact	0.1	K cm^2W^{-1}	-
bottom contact	0.01	K cm^2W^{-1}	-
electrical contact resistances:			
top contact	1	Ω	-
bottom contact	1	Ω	-

Table 4.8: Thermal and electrical terminal parameters.

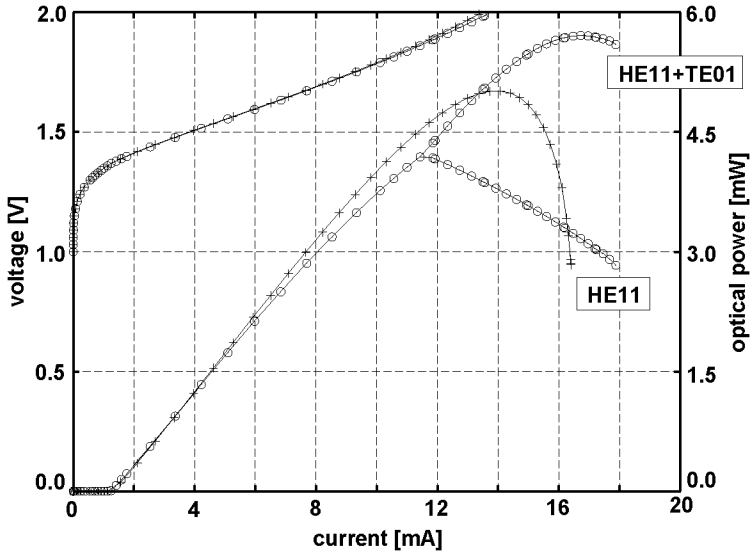

Figure 4.18: Current voltage and current optical power characterstics for VCSEL structure with surface relief and $r_{ox} = 3$ μm. Curves with + show result if optical problem is solved only once at the beginning of the simulation. Curves with $\circ$ show results for self-consistent electro-thermo-optical solution.

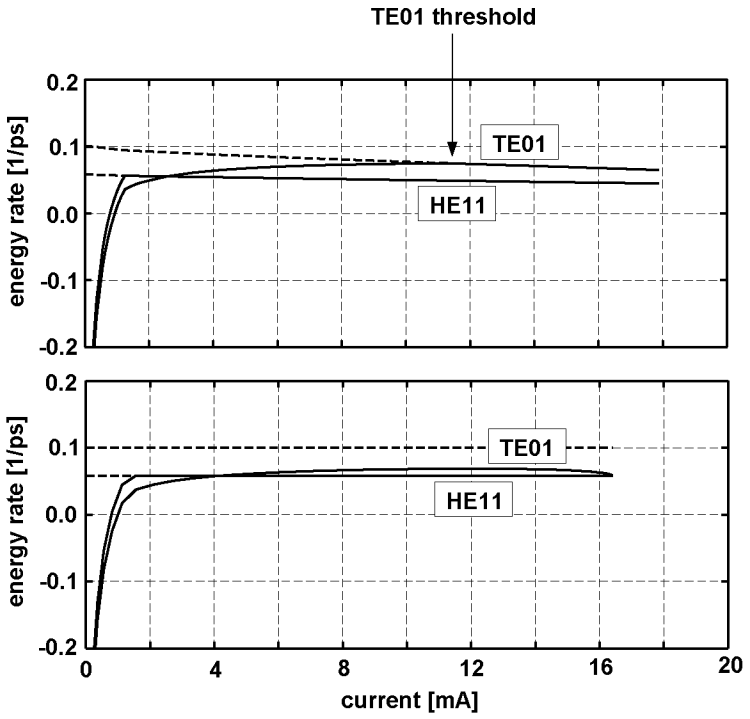

Figure 4.19: Modal optical gain given by the active region (solid lines) and optical loss given by the remaining device structure (dashed lines) for HE11 and TE01 optical modes versus terminal current. Top: self-consistent electro-thermo-optical solution. Bottom: optical problem is solved only once.

so that significant deviations, as shown in Figs. 4.18 and 4.19, arise. These deviations can be as severe as causing the complete absence of the threshold of a second order mode. It is therefore essential that a self-consistent electro-thermo-optical model is employed for the optimisation task that is envisaged in this tutorial. Most heating in the device can be attributed to Joule heating. Further contributions come from Thomson/Peltier heat and recombination heat in the λ cavity. Heating affects the refractive index according to Eq. (3.9) and reduces scattering losses. Via the effect of thermal lensing, which is dependent on the the design of the VCSEL structure, the material absorption and gain experienced by the optical mode is altered.

Further to the results in Fig. 4.18 hole current, total heat power, temperature, refractive index close to the active region, normalised intensity, hole density, optical material gain in the active region, and wavelength tuning of the HE11 and TE01 modes, and the maximum of the optical gain are given in Figs. 4.20 and 4.21, respectively. Current crowding at the oxide aperture $r_{ox} = 3$ μm is visible in Fig. 4.20. Strong thermal lensing and spatial hole burning can be observed in Fig. 4.21 respectively.

Single-Mode Optimisation Using Metallic Absorbers and Anti-Resonant Structures

In this section an optimum radius r_{ox} of the oxide aperture is determined using self-consistent simulations. The results are shown in Fig. 4.22 for the original structure, in Fig. 4.23 for the metallic absorber, and in Fig. 4.24[5] for the surface relief enhancement of the optical resonator.

It is obvious that the VCSEL with the anti-resonant structure beats the other candidates by far: 4.4 mW single mode power is achieved for an oxide aperture of 4 μm compared to 2.1 mW for the best original VCSEL structure with an aperture of 2 μm. The best VCSEL device structure with the metallic absorber reaches 2.3 mW with an aperture of 2 μm and performs only slightly better than the best original structure.

For $r_{ox} = 1$ μm all devices show pure single mode operation and

[5]Please note that the scale changes in Fig. 4.24.

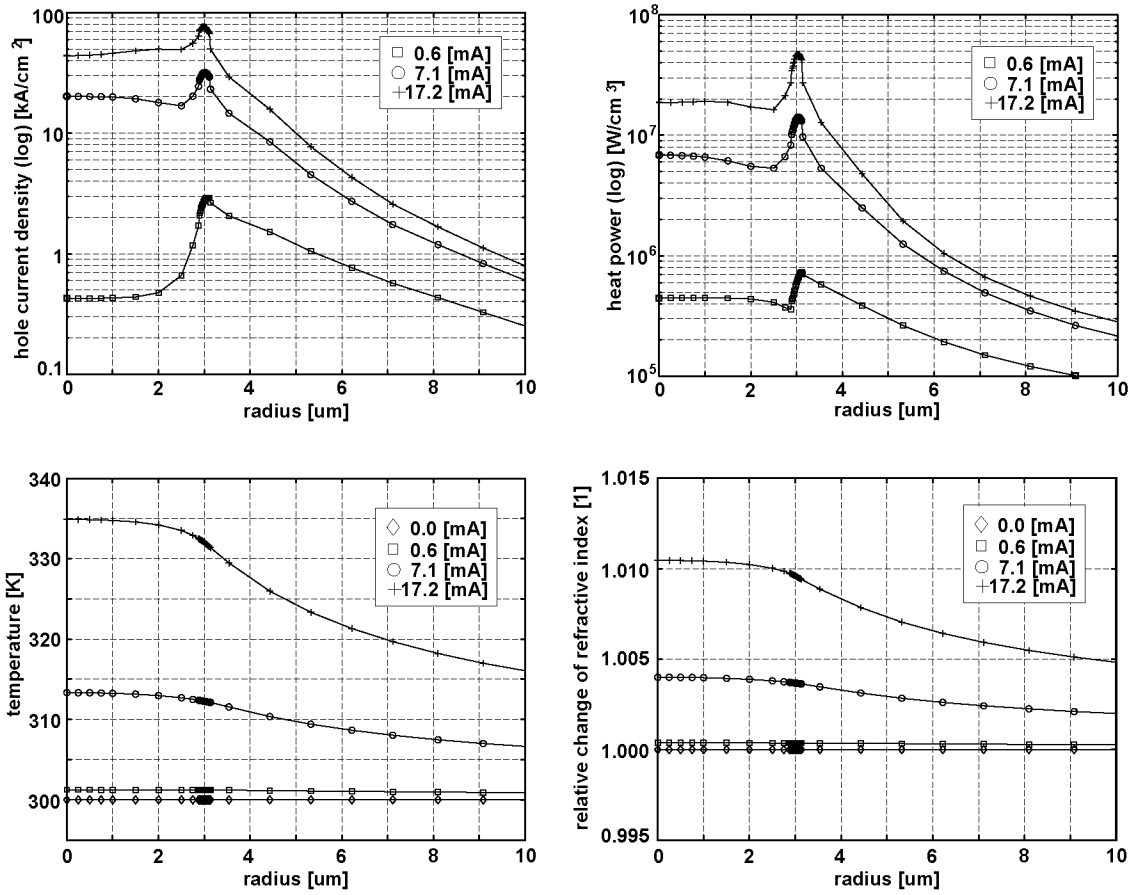

Figure 4.20: Hole current density, total heat power density, temperature, and relative refractive index distributions in a plane at 50 nm from the quantum well on the anode side. Distributions are shown at different terminal currents for a VCSEL structure with surface relief and $r_{ox} = 3$ μm

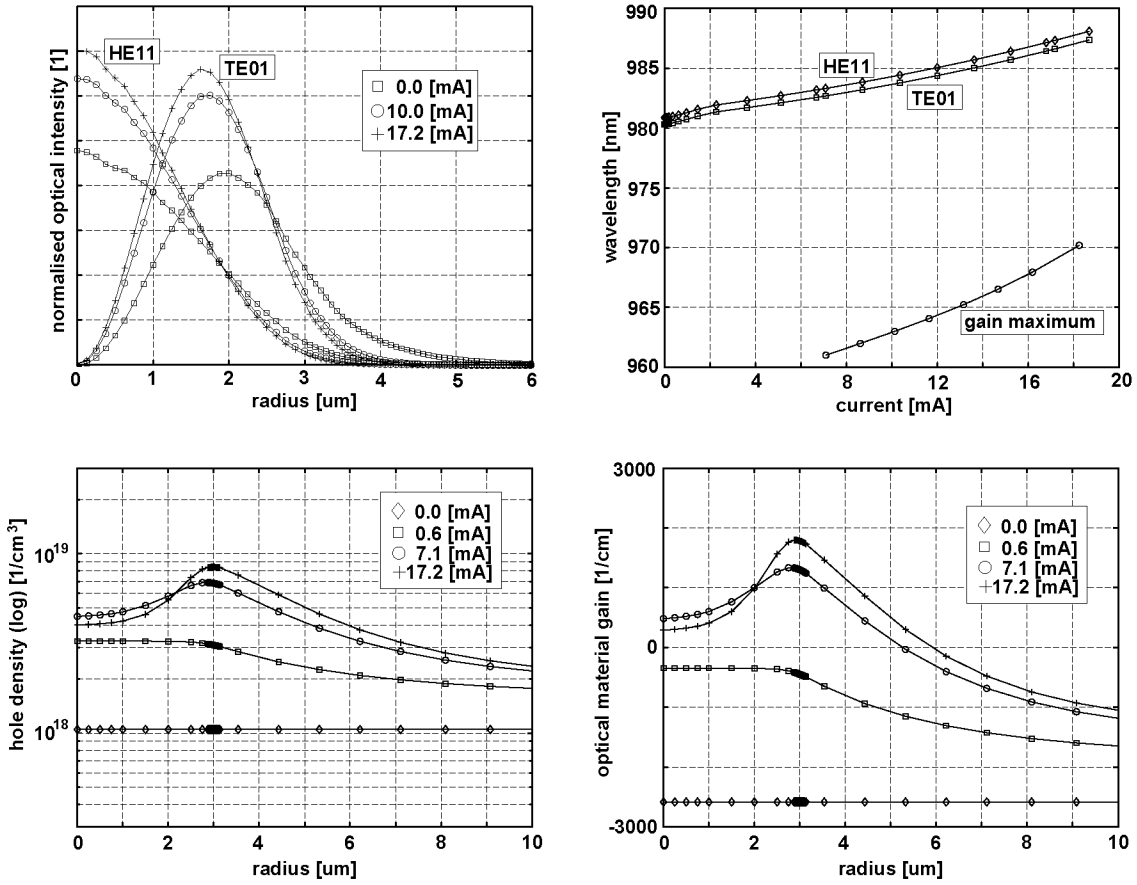

Figure 4.21: Thermal lensing and wavelength tuning due to heating in optical resonator, and spatial hole burning in active region for a VC-SEL structure with surface relief and $r_{ox} = 3$ μm. Normalised optical intensity distributions of HE11 and TE01 optical modes. Tuning of HE11 and TE01 mode resonances, and optical gain maximum versus current. Distribution of quantum well bound hole density and optical material gain.

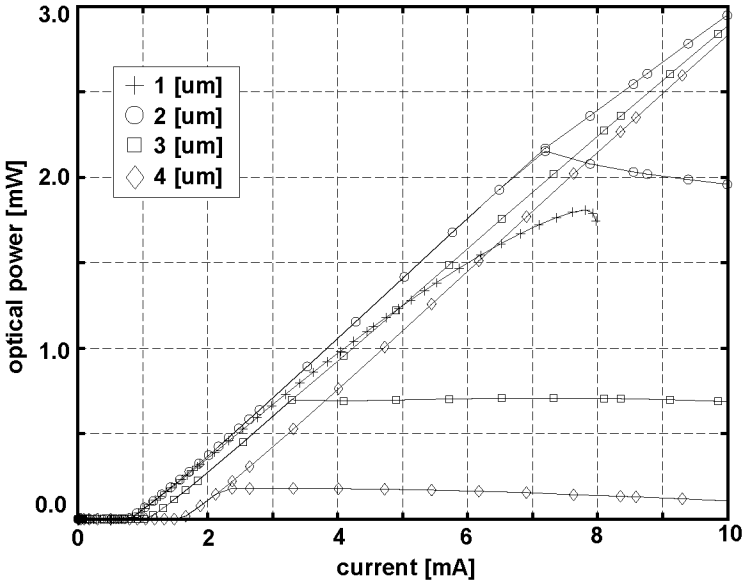

Figure 4.22: Optical power versus current for HE11 and TE01 modes. Values are plotted for different oxide aperture radii r_{ox}.

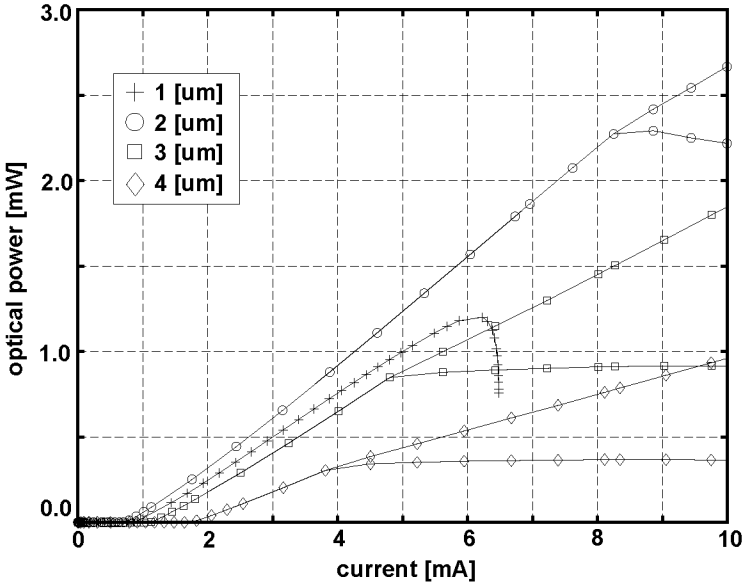

Figure 4.23: Optical power versus current for HE11 and TE01 modes, r_m of the metallic absorber is set to 2.5 μm. Values are plotted for different oxide aperture radii r_{ox}.

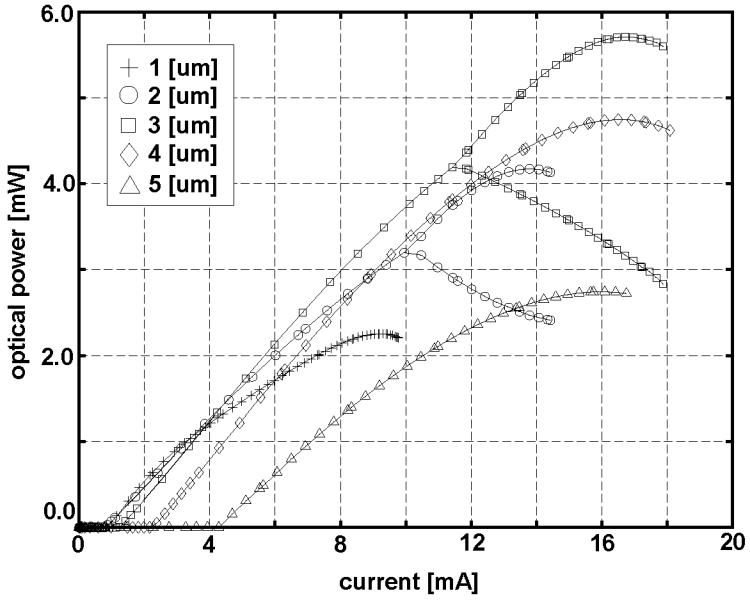

Figure 4.24: Optical power versus current for HE11 and TE01 modes, r_e of the surface relief is set to 2.5 μm and t_e = 72 nm. Values are plotted for different oxide aperture radii r_{ox}.

maximum single mode power is limited by self-heating. By increasing the aperture radius self-heating can be lowered and higher power levels can be reached before roll-over occurs. At the same time higher order modes are no longer cut off and consequently limit the maximum single mode power. The larger the aperture the lower the discrimination between the fundamental and higher order modes and the lower the maximum single mode power becomes.

The enhanced structures manage to push the TE01 threshold to higher values compared to the original structure, due to the higher discrimination between HE11 and TE01 modes. In the case of the metallic absorber with r_{ox} = 4 μm in Fig. 4.23, 4 mA are reached compared to 2.1 mA in Fig. 4.22. Unfortunately, this effect is not exploited effectively by the metallic absorber. Although TE01 thresholds are now higher, the absorber increasingly screens radiation as the oxide aperture is made larger. This has already been observed in Fig. 4.17 and is seen here to gradually lower the slope of the current versus optical power curve in Fig. 4.23 and compromise the maximum single mode power that can be reached.

The anti-resonant structure (Fig. 4.24) pushes the TE01 threshold

to even higher values because the optical resonator offers the highest discrimination between HE11 and TE01 modes of the three design variants. For oxide apertures with 4 μm and 5 μm TE01 thresholds are not present at all. Here, the roll-over has an additional contribution from lateral carrier leakage [33] that originates from the misalignment of the HE11 mode with the optical gain profile. Figure 4.21 reveals strong spatial hole burning in the optical gain profile at higher currents and the effect of thermal lensing on the optical modes. The overlap of the optical gain profile with the HE11 mode determines the spatial profile of the current sunk by stimulated emission in the HE11 mode. If that profile does not match the one given by the current injection, the optical mode will start to deplete carriers in the active region. In order to maintain the HE11 modal gain, additional current has to be provided to counterbalance the carrier depletion. This additional current cannot be turned into photons and is therefore lost as lateral leakage current. This leads to the roll-over observed in Fig. 4.24 for larger oxide apertures.

Conclusion

The task was to optimise a device structure to achieve maximum single mode emission. The exercise, although not carried out exhaustively, gives essential insights into designing a VCSEL device for the envisaged goal. Only marginal improvements are possible with the proposed metallic absorber structure. It only slightly improves mode discrimination over the original structure and is limited by its inherently low HE11 output coupling efficiency. In contrast, high mode discrimination and high HE11 output coupling efficiencies are possible using an anti-resonant structure. The necessity of an additional tightly controlled masking and etch step to fabricate a surface relief make this the more expensive solution. A further increase in single mode power would be expected if the current injection could be concentrated further to the symmetry axis of the device without affecting the optical field.

Chapter 5

Conclusion and Outlook

5.1 Major Results

A comprehensive VCSEL device model and its software implementation in a simulator was presented. The input parameters to the model equations are measurable physical material parameters and the topology of the device structure, as opposed to the effective parameters of a simple rate equation model. The spatially resolved electrical potential, electron and hole densities, local temperature, mean optical intensity, and derived secondary quantities provide the user with valuable insights required for device design and optimisation. Additionally, electrical, thermal and optical terminal quantities can be computed and compared to measured characteristics.

It was shown that the self-consistent solution of the electro-thermal and optical problem is mandatory for VCSEL simulation. It was recognised that the Gummel iteration procedure employed for this is only useful in practice if solutions to Maxwell's vectorial wave equation can be computed efficiently. For this purpose a method was devised based on a continuation scheme. This allows, for the first time, that Maxwell's vectorial wave equation – for VCSELs with realistic structures and optical sizes – subject to an open boundary imposed by PML, can be solved self-consistently with the electro-thermal device equations.

The accuracy of the method to compute the optical modes was assessed. Further to this, the practical relevance of the simulator software as a design tool for the analysis and optimisation of VCSEL device structures was demonstrated.

5.2 Further Work

Important future work is summarized. Some suggestions relate to improvements of the present model and others to extending the capabilities of the simulator.

- Improve optical gain model with $k \cdot p$ bandstructure calculation of varying order, and including many-body effects [20, 30, 29].
- Introduce electron and hole temperature different from the lattice temperature for carriers in the quantum well [18].
- Verify dynamic response (modulation and transient) of present model with measurements. In particular, verify quantum well capture and escape rate model.
- Devise relative intensity noise model based on small signal modulation response feature of present simulator.
- Introduce higher polynomial order (> second order) finite elements for expansion of Maxwell's vectorial wave equation.
- Optimise preconditioning of Jacobi-Davidson QZ algorithm used to compute eigenpairs of Maxwell's vectorial wave equation (multi-level preconditioning).

Investigations in this work indicate that a better trade-off between computational complexity and accuracy of the solution can be reached for higher or mixed element polynomial orders.

Higher order finite elements and optimisation of preconditioning are the preliminaries for a true 3D formulation and solution of the electro-thermo-optical problem using finite elements. Photonic crystal optical resonators and other circularly non-symmetric cavities could then be analysed.

Appendix A

Photon Rate Equation

In the following the important steps in deriving the photon rate equations and the accompanying eigenproblem that yields a useful expansion of the electromagnetic field into modes will be reviewed for the VCSEL case. The detailed development is in [21].

In a dielectric medium with negligible magnetic properties the constitutive equations are

$$\boldsymbol{D}(\boldsymbol{r},t) = \varepsilon_0 \boldsymbol{E}(\boldsymbol{r},t) + \boldsymbol{P}(\boldsymbol{r},t) + \boldsymbol{K}(\boldsymbol{r},t) \tag{A.1}$$

$$\boldsymbol{B}(\boldsymbol{r},t) = \mu_0 \boldsymbol{H}(\boldsymbol{r},t) \tag{A.2}$$

where $\boldsymbol{P}(\boldsymbol{r},t)$, $\boldsymbol{K}(\boldsymbol{r},t)$ are the polarisation terms, $\boldsymbol{E}(\boldsymbol{r},t)$ is the electric, $\boldsymbol{H}(\boldsymbol{r},t)$ the magnetic field, ε_0 and μ_0 are the vacuum permittivity and permeability, respectively.

The polarisation $\boldsymbol{P}(\boldsymbol{r},t)$ is the response of the active medium to the electric field. If a linear response is assumed it is obtained by convolution of the electric field with a response function

$$\boldsymbol{P}(\boldsymbol{r},t) = \varepsilon_0 \int_0^\infty \chi(\boldsymbol{r},t,\tau)\boldsymbol{E}(\boldsymbol{r},t-\tau)d\tau \tag{A.3}$$

where $\chi(\boldsymbol{r},t,\tau)$ is the first order polarisation impulse response of the medium and causal. It is assumed quasi time-translationally invariant. Therefore, $\chi(\boldsymbol{r},t,\tau)$ is time-translationally invariant on the time

scale of the polarisation τ but varies slowly on the time scale t. Furthermore, $\boldsymbol{K}(\boldsymbol{r},t)$ represents the contribution to $\boldsymbol{D}(\boldsymbol{r},t)$ due to spontaneous emission and is therefore independent of the electric field.

Using Maxwell's equations in the time-domain, with charge density and current set to zero[1], and making use of the constitutive equations (A.1 and A.2) yields the wave equation

$$\nabla \times [\nabla \times \boldsymbol{E}(\boldsymbol{r},t)] + \frac{1}{c_0^2}\frac{\partial^2}{\partial t^2}\left[\varepsilon_r(\boldsymbol{r},t,\tau) * \boldsymbol{E}(\boldsymbol{r},t-\tau)\right] = -\mu_0 \frac{\partial^2}{\partial t^2}\boldsymbol{K}(\boldsymbol{r},t) \tag{A.4}$$

where the star denotes convolution in τ and

$$\varepsilon_r(\boldsymbol{r},t,\tau) = \delta(\tau) + \chi(\boldsymbol{r},t,\tau). \tag{A.5}$$

The Fourier transform of Eq. (A.5)

$$\varepsilon_r(\boldsymbol{r},t,\omega) = \int_0^\infty \varepsilon_r(\boldsymbol{r},t,\tau)e^{i\omega\tau}d\tau \tag{A.6}$$

is the frequency dependent dielectric function in a medium dependent on time t due to the modulation of the density of electron hole pairs[2]

The electric field is expanded into modes as follows

$$\boldsymbol{E}(\boldsymbol{r},t) = \sum_{k=1}^{N} a_k(t)\underline{\boldsymbol{E}}_k(\boldsymbol{r},t)e^{-i\int_0^t \omega_k'(\tau)d\tau} + c.c. \tag{A.7}$$

with the complex-valued scalar coefficient $a_k(t)$, and the real-valued scalar function $\omega_k'(t)$ given by

$$\omega_k'(t) = \omega_{k,nom}' + \Delta\omega_k'(t) \tag{A.8}$$

where $\omega_{k,nom}'$ is the nominal optical frequency and $\Delta\omega_k'(t)$ the frequency shift or chirp of term k in the expansion (A.7). A useful choice for $\omega_k'(t)$ and $\underline{\boldsymbol{E}}_k(\boldsymbol{r},t)$ will be made in due course. Equation (A.7) is

[1] Current flow and formation of space charge are negligible at optical frequencies; there is only local polarisation of the dielectric medium.

[2] Using this definition of the Fourier transform, a local gain or loss results in a local negative or positive imaginary part of $\varepsilon_r(\boldsymbol{r},t,\omega)$, respectively.

inserted into Eq. (A.4) and only first order terms of the time derivative on the left hand side of Eq. (A.4) are taken into account[3]

$$\begin{aligned}
&\sum_k e^{-i\int_0^t \omega_k'(\tau)d\tau} \quad . \\
&\left\{\left[\nabla\times\nabla\times\underline{\boldsymbol{E}}_k(\boldsymbol{r},t)+\frac{\omega_k'^{\,2}(t)}{c_0^2}\varepsilon_r(\boldsymbol{r},t,\omega_k')\underline{\boldsymbol{E}}_k(\boldsymbol{r},t)\right]a_k(t)\right. \\
&\left.+\frac{2i\omega_k'(t)}{c_0^2}\left[\frac{\omega_k'(t)}{2}\frac{\partial}{\partial\omega_k'}\varepsilon_r(\boldsymbol{r},t,\omega_k')+\varepsilon_r(\boldsymbol{r},t,\omega_k')\right]\underline{\boldsymbol{E}}_k(\boldsymbol{r},t)\dot{a}_k(t)\right\} \\
&=\boldsymbol{F}(\boldsymbol{r},t)
\end{aligned} \tag{A.9}$$

where $\boldsymbol{F}(\boldsymbol{r},t)$ is equal to the right hand side of the wave equation (A.4).

Furthermore, $\underline{\boldsymbol{E}}_k(\boldsymbol{r},t)$ are chosen to satisfy the following eigenproblem

$$\begin{aligned}
&\left[\nabla\times(\nabla\times)+\frac{\omega_k'^{\,2}(t)}{c_0^2}\varepsilon_r(\boldsymbol{r},t,\omega_k')\right]\underline{\boldsymbol{E}}_k(\boldsymbol{r},t) \\
&=\omega_k''(t)\,\tilde{\varepsilon}_r(\boldsymbol{r},t,\omega_k')\underline{\boldsymbol{E}}_k(\boldsymbol{r},t)
\end{aligned} \tag{A.10}$$

at each point in time t with

$$\tilde{\varepsilon}_r(\boldsymbol{r},t,\omega_k')=\frac{2i\omega_k'(t)}{c_0^2}\left[\frac{\omega_k'(t)}{2}\frac{\partial}{\partial\omega_k'}\varepsilon_r(\boldsymbol{r},t,\omega_k')+\varepsilon_r(\boldsymbol{r},t,\omega_k')\right] \tag{A.11}$$

where $\omega_k''(t)$ is the eigenvalue which has the unit of a rate. Because optical gain and loss are present in the dielectric function, Eq. (A.10) is a generalised, non-Hermitian, complex symmetric eigenproblem. For the eigenpairs of Eq. (A.10) the orthogonality relation

$$(\underline{\boldsymbol{E}}_k(\boldsymbol{r},t),\underline{\boldsymbol{E}}_l(\boldsymbol{r},t))_{\tilde{\varepsilon},\omega_0}=\iiint_V \underline{\boldsymbol{E}}_k(\boldsymbol{r},t)\cdot\tilde{\varepsilon}_r(\boldsymbol{r},t,\omega_0)\underline{\boldsymbol{E}}_l(\boldsymbol{r},t)\,dV=\delta_{ij} \tag{A.12}$$

holds. The frequency $\omega_k'(t)$ can be determined by solving Eq. (A.10) and requiring $\omega_k''(t)$ to be real-valued for every t.

[3]If higher order terms are included at this point one arrives at a coupled set of photon rate equations for the non-adiabatic regime [21] which will not be discussed here.

Replacing the expression in the first round bracket of Eq. (A.9) with Eq. (A.10) multiplying from the left by

$$e^{i\int_0^t \omega_l'(\tau)d\tau}\,\underline{\boldsymbol{E}}_l(\boldsymbol{r},t) \tag{A.13}$$

and integrating transforms Eq. (A.9), due to the orthogonality property Eq. (A.12), into a set of decoupled scalar rate equations

$$\omega_l''(t)\cdot a_l(t)+\frac{d}{dt}a_l(t)=f_l(t) \tag{A.14}$$

that describe the time evolution of the electric field. A rate equation is obtained for each term of the expansion (A.7), with

$$f_l(t)=\iiint_V \underline{\boldsymbol{E}}_l(\boldsymbol{r},t)\cdot\underline{\boldsymbol{F}}(\boldsymbol{r},t)dV\cdot e^{i\int_0^t \omega_l'(\tau)d\tau}. \tag{A.15}$$

Accounting for the stochastic nature of the spontaneous emission source term $\underline{\boldsymbol{F}}(\boldsymbol{r},t)$ the photon rate equations for the time evolution of electro-magnetic energy $S_l(t)$ in mode l

$$\frac{d}{dt}S_l(t)=-2\omega_l''(t)\cdot S_l(t)+R_l^{sp}(t) \tag{A.16}$$

can be derived from Eqs. (A.14), using field-field correlation functions and the Wiener-Khinchine theorem. The latter relates correlation functions of fields to energy spectrum densities [21] via the Fourier transform. The term R_l^{sp} is given by Eq. 2.17.

It follows that in the adiabatic approximation Eq. (A.4) can be transformed into a set of decoupled scalar differential equations (A.16). The variables of these equations are co-ordinates on a basis given by the eigenvectors of eigenproblem (A.10).

Appendix B

Perfectly Matched Layers

The diagonal tensor Λ for cylindrical coordinates is given in [118].

$$\Lambda = \begin{bmatrix} \Lambda_\rho & 0 & 0 \\ 0 & \Lambda_\phi & 0 \\ 0 & 0 & \Lambda_z \end{bmatrix} = \begin{bmatrix} \frac{\tilde{\rho}}{\rho}\frac{s_z}{s_\rho} & 0 & 0 \\ 0 & \frac{\rho}{\tilde{\rho}} s_z\, s_\rho & 0 \\ 0 & 0 & \frac{\tilde{\rho}}{\rho}\frac{s_\rho}{s_z} \end{bmatrix}. \tag{B.1}$$

The complex spatial variable $\tilde{\rho}$ is defined as

$$\tilde{\rho} = \rho_0 + \int_{\rho_0}^{\rho} s_\rho\left(\rho'\right) d\rho'. \tag{B.2}$$

A quadratic profile is used

$$s_\rho\left(\rho\right) = \begin{cases} 1 & 0 \le \rho \le \rho_I \\ 1 + i s_0 \left(\frac{\rho - \rho_I}{d_R}\right)^2 & \rho > \rho_I \end{cases} \tag{B.3}$$

$$s_z\left(z\right) = \begin{cases} 1 + i s_0 \left(\frac{z_{I,b} - z}{d_B}\right)^2 & z < z_{I,b} \\ 1 & z_{I,b} \le z \le \rho_{I,t} \\ 1 + i s_0 \left(\frac{z - z_{I,t}}{d_T}\right)^2 & z > z_{I,t} \end{cases} \tag{B.4}$$

with ρ_I, $z_{I,b}$, $z_{I,t}$ the coordinates of the side, bottom, and top boundary Γ_I of region I. Moreover, d_R, d_B, and d_T are the thicknesses of the respective PML layers, and s_0 the PML absorption parameter. The complex spatial variable $\tilde{\rho}$ is then given by

$$\tilde{\rho} = \begin{cases} \rho & 0 \leq \rho \leq \rho_I \\ \rho + i s_0 \frac{(\rho - \rho_I)^3}{3\, d_R^2} & \rho > \rho_I. \end{cases} \tag{B.5}$$

Appendix C

Hybrid Edge-Node Finite Element Expansion Functions

The element basis functions are illustrated in Figs. C.1 – C.4. For the triangles the simplex coordinates $\zeta_1 = 1-\rho-z$, $\zeta_2 = \rho$, and $\zeta_3 = z$ are introduced. The first order triangular node and edge element basis functions are defined as [84]

$$N_i^T(\rho, z) = \zeta_i \tag{C.1}$$

$$\mathbf{N}_i^T(\rho, z) = \zeta_i \nabla_T \zeta_{i+1} - \zeta_{i+1} \nabla_T \zeta_i \tag{C.2}$$

and for second order as

$$N_{i+3}^T(\rho, z) = 4\zeta_{i+1}\zeta_i \tag{C.3}$$

$$\mathbf{N}_{i+3}^T(\rho, z) = \zeta_i \nabla_T \zeta_{i+1} + \zeta_{i+1} \nabla_T \zeta_i \tag{C.4}$$

$$\mathbf{N}_{i+6}^T(\rho, z) = \zeta_{i+2}\left(\zeta_i \nabla_T \zeta_{i+1} - \zeta_{i+1} \nabla_T \zeta_i\right) \tag{C.5}$$

$$\tag{C.6}$$

with index i in ζ_i wrapping modulo 3. Note $\mathbf{N}_9^T$ can be formed as a linear combination of $\mathbf{N}_7^T$ and $\mathbf{N}_8^T$. It may therefore be discarded.

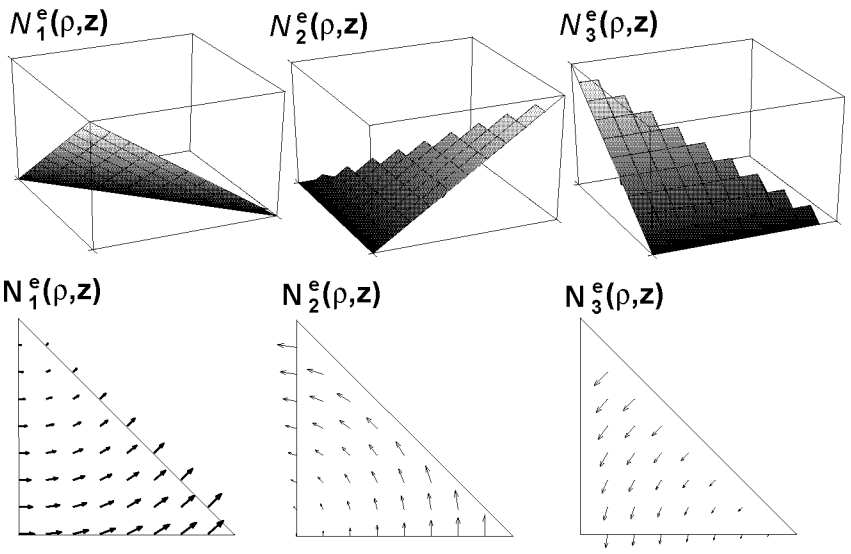

Figure C.1: First order node and edge finite element basis functions for triangle.

The simplex coordinates are redefined $\zeta_1 = 1 - \rho$, $\zeta_2 = 1 - z$, $\zeta_3 = \rho$, and $\zeta_4 = z$ for rectangles. The rectangular node and edge element basis functions read

$$N_i^R(\rho, z) = \zeta_i \zeta_{i+1} \tag{C.7}$$

$$\mathbf{N}_i^R(\rho, z) = -\zeta_{i+1} \nabla_T \zeta_i \tag{C.8}$$

for first order and

$$N_{i+4}^R(\rho, z) = 4\zeta_i \zeta_{i+1} \zeta_{i+2} \tag{C.9}$$

$$N_9^R(\rho, z) = 16\zeta_1 \zeta_2 \zeta_3 \zeta_4 \tag{C.10}$$

$$\mathbf{N}_{i+4}^R(\rho, z) = (1 - 2\zeta_i)\, \zeta_{i+1} \nabla_T \zeta_i \tag{C.11}$$

$$\mathbf{N}_{i+8}^R(\rho, z) = \zeta_i \zeta_{i+1} \zeta_{i+2} \nabla_T \zeta_{i+1} \tag{C.12}$$

for second order. The index i in ζ_i is assumed to wrap modulo 4.

The integrals in Eqs. (3.16–3.18) over triangular and rectangular domains in ρ, ϕ, z are transformed to ζ_i coordinates with $i = 1 \ldots 3$ for triangles and $i = 1 \ldots 4$ for rectangles. The transformed integrals are evaluated numerically using Gauss quadrature [84].

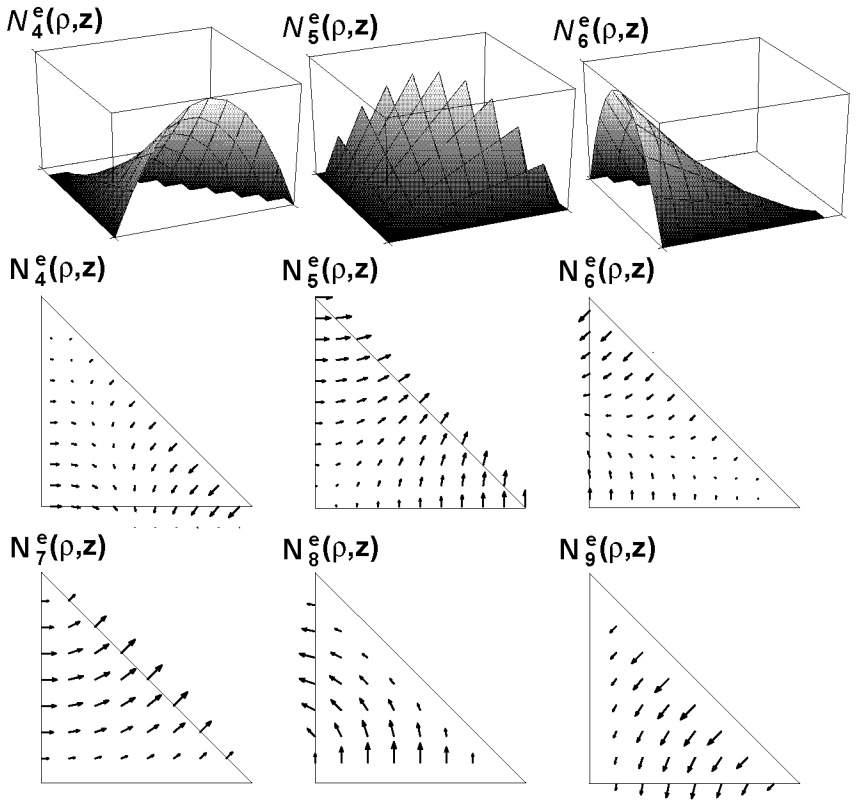

Figure C.2: Second order node and edge finite element basis functions for triangle.

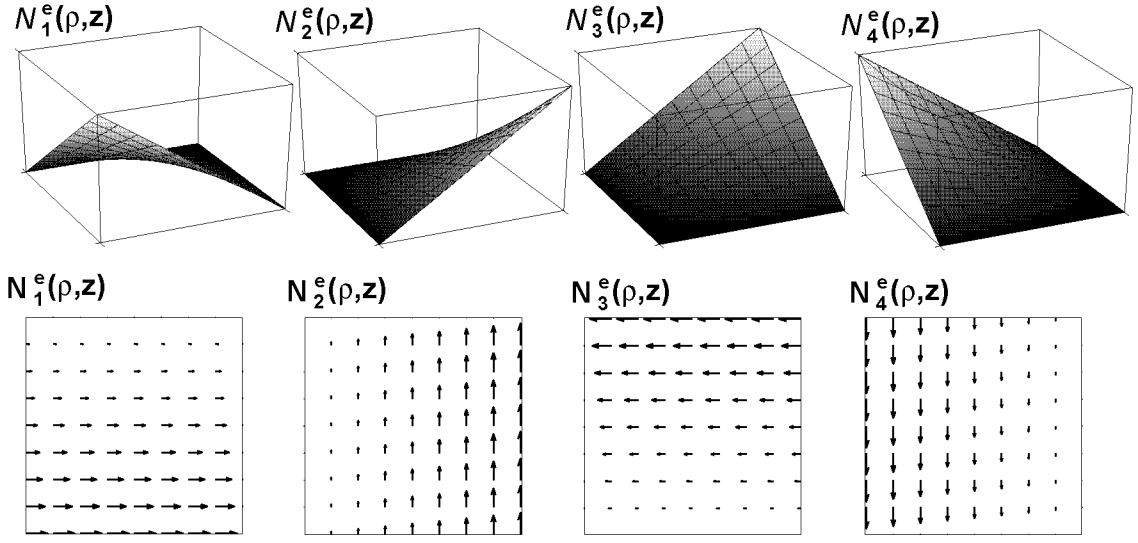

Figure C.3: First order node and edge finite element basis functions for rectangle.

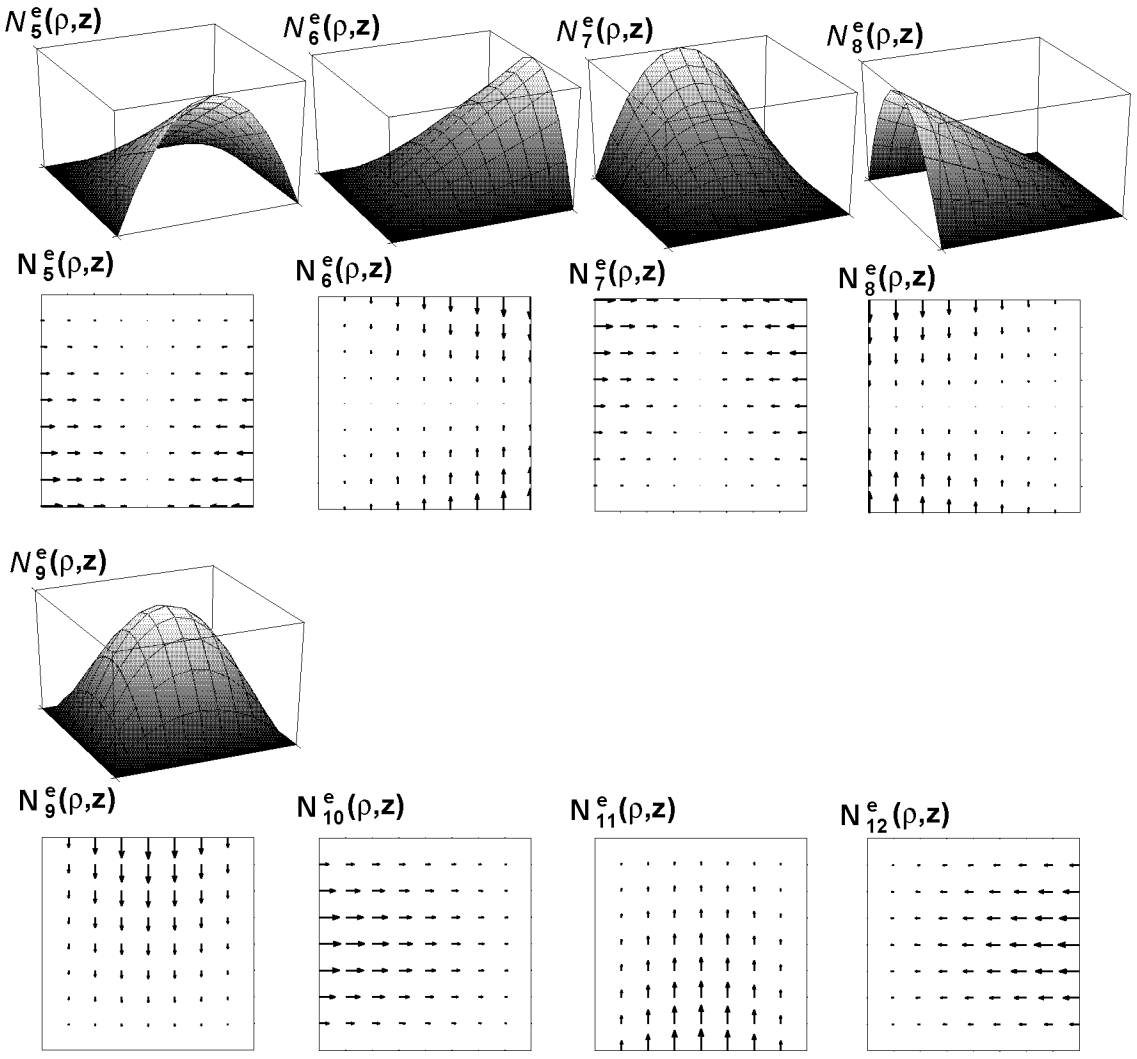

Figure C.4: Second order node and edge finite element basis functions for rectangle.

Appendix D

List of Symbols

$\boldsymbol{B}$	Magnetic flux density
$\underline{\boldsymbol{B}}$	Pattern of magnetic flux density, frequency domain (complex)
c_0	Vacuum speed of light
$c_t h$	Total heat capacity
C^{cap}	Carrier capture rate
$\boldsymbol{D}$	Electric displacement flux density
$\underline{\boldsymbol{D}}$	Pattern of electric displacement, frequency domain (complex)
e	Elementary charge
E	Energy
E_g	Band gap
E_c, E_v	Conduction and valence band edge
$E_{F,n}, E_{F,p}$	Quasi Fermi energies
$\boldsymbol{E}$	Electric field
$\underline{\boldsymbol{E}}$	Electric field pattern, frequency domain (complex)
f^C, f^V	Distribution function for electrons and holes
f	Frequency
G	Modal optical gain
$\underline{\boldsymbol{G}}$	Green's function, frequency domain (complex)
$\boldsymbol{H}$	Magnetic field
$\underline{\boldsymbol{H}}$	Magnetic field pattern, frequency domain (complex)
$\hbar$	Reduced Planck constant
i	Imaginary unit, $i^2 = -1$
$\mathrm{Im}\,[\ldots]$	Imaginary part of a complex number
$\boldsymbol{j}$	Current density

$\boldsymbol{K}$	Constant polarisation
$\boldsymbol{k}$	Wave vector
k	Wave number, $k = \lvert\boldsymbol{k}\rvert$
k_B	Boltzmann constant
L	Modal optical loss
m_e, m_h	Electron and hole effective mass
m_0	Free electron mass
n	Electron density
n	Refractive index
N_D^+, N_A^-	Activated donor and acceptor concentrations
N_c, N_v	effective density of states for conduction and valence band
$\boldsymbol{P}$	Polarisation in response to electric field
P_n, P_p	Absolute thermoelectric power for electrons and holes
P_{out}	Optical output power
p	Hole density
Q	Resonator quality factor
$\boldsymbol{r}$	Location in space
r^{sp}	Local spontaneous emission
R_k^{sp}	Spontaneous emission rate into optical mode k
R	Carrier recombination rate
$\mathrm{Re}\,[\ldots]$	Real part of a complex number
S_k	Photon number in optical mode k
$\boldsymbol{S}$	Poynting vector
$\boldsymbol{S}$	Heat flux
T	Temperature
t	Time
v	Phase velocity
v_g	Group velocity
w	Electromagnetic energy density
α	Material absorption or gain
α_n	Temperature coefficient of refractive index
δ	Dirac function
ε_r	Relative permittivity
ε_0	Vacuum permittivity
κ_{th}	Thermal conductivity
κ	Absorption coefficient
λ	Wavelength
μ_0	Vacuum permeability
μ_r	Relative permeability
μ_n, μ_p	Electron and hole mobility
ρ^{opt}	Optical mode density

ρ^{el}	Reduced density of states for electrons and holes
τ	Characteristic time constant
ϕ_e, ϕ_h	Quasi-Fermi potentials for electrons and holes
ϕ	Electric potential
χ	Electric susceptibility
χ	Electron affinity
ω	Angular frequency
$\omega' - i\omega''$	Complex angular frequency

Bibliography

[1] H. Soda, K. Iga, C. Kithara, and Y. Suematsu. GaInAsP/InP surface emitting injection-lasers. *Japanese Journal of Applied Physics*, 18(12):2329–2330, 1979.

[2] K. Iga, F. Koyama, and S. Kinoshita. Surface emitting semiconductor lasers. *IEEE Journal of Quantum Electronics*, 24(9):1845–1855, 1988.

[3] J. L. Jewell, A. Scherer, S. L. McCall, Y. H. Lee, S. Walker, J. P. Harbison, and L. T. Florez. Low-threshold electrically pumped vertical-cavity surface-emitting microlasers. *Electronics Letters*, 25(17):1123–1124, 1989.

[4] J. L. Jewell, J. P. Harbison, A. Scherer, Y. H. Lee, and L. T. Florez. Vertical-cavity surface-emitting lasers: Design, growth, fabrication, characterisation. *IEEE Journal of Quantum Electronics*, 27(6):1332–1346, 1991.

[5] A. E. Bond, P. D. Dapkus, and J. D. O'Brien. Design of low-loss single-mode VCSELs. *IEEE Journal of Selected Topics in Quantum Electronics*, 5(3):574–581, 1999.

[6] R. Jäger, M. Grabherr, C. Jung, R. Michalzik, G. Reiner, B. Weigl, and K. J. Ebeling. Low-threshold electrically pumped vertical-cavity surface-emitting microlasers. *Electronics Letters*, 33(4):330–331, 1997.

[7] K. L. Lear, V. M. Hietala, H. Q. Hou, M. Ochiai, J. J. Banas, B. E. Hammons, Zolper J. C., and S. P. Kilcoyne. Small and large signal modulation of 850 nm oxide-confined vertical-cavity surface-emitting lasers. *OSA Trends in Optics and Photonics*, 15:69–74, 1997.

[8] J. Boucart, C. Starck, F. Gaborit, A. Plais, N. Bouché, E. Derouin, J. C. Remy, J. Bonnet-Gamard, L. Goldstein, C. Fortin, D. Carpentier, P. Salet, F. Brillouet, and J. Jacquet. Metamorphic DBR

and tunnel-junction injection: A CW RT monolithic long-wavelength VCSEL. *IEEE Journal of Selected Topics in Quantum Electronics*, 5(3):520–529, 1999.

[9] K. Streubel, M. Hammar, F. Salomonsson, J. Bentell, S. Mogg, S. Rapp, J. Jacquet, J. Boucart, C. Stark, A. Plais, F. Gaborit, E. Derouin, N. Bouche, A. Rudra, A. V. Syrbu, Iakovlev V. P., C. A. Berseth, O. Dehaese, E. Kapon, H. Moussa, and I. Sagnes. Novel technologies for 1.55 μm vertical cavity lasers. *SPIE Optical Engineering*, 39(2):488–497, 2000.

[10] M. Ortsiefer, R. Shau, G. Böhm, F. Köhler, and M.-C. Amann. Low-threshold index-guided $1.5\mu m$ long-wavelength vertical-cavity surface-emitting laser with high efficiency. *Applied Physics Letters*, 76(16):2179–2181, April 2000.

[11] S. R. Bank, M. A. Wistey, H. B. Yuen, L. L. Goddard, and J. S. Harris. Low-threshold CW GaInNAsSb/GaAs laser at 1.49 μm. *Electronics Letters*, 39(20):1445–1446, 2003.

[12] D. G. Deppe, D. L. Huffaker, J. Shin, and Q. Deng. Very-low-threshold index-confined planar microcavity lasers. *IEEE Photonics Technology Letters*, 7(9):965–966, 1995.

[13] G. S. Li, R. F. Nabiev, W. Yuen, M. Jansen, D. Davis, and C. J. Chang-Hasnain. Electrically-pumped directly-modulated tunable VCSEL for metro DWDM applications. In *Proceedings of the 27th European Conference on Optical Communication ECOC*, 2001.

[14] L. A. Coldren and S. W. Corzine. *Diode Lasers and Photonic Integrated Circuits*. John Wiley & Sons, Inc., New York, 1995.

[15] M. Jungo, D. Erni, and W. Bächtold. VISTAS: A comprehensive system-oriented spatiotemporal VCSEL model. *IEEE Journal on Selected Topics in Quantum Electronics*, 9(3):939–948, 2003.

[16] W.-C. Ng. *Thermal and Optical Simulations of Vertical-Cavity Surface-Emitting Lasers*. Ph.D. dissertation, University of Illinois at Urbana-Champaign, Urbana, United States, 2002.

[17] M. Grupen and K. Hess. Simulation of carrier transport and nonlinearities in quantum-well laser diodes. *IEEE Journal of Quantum Electronics*, 34(1):120–140, 1998.

[18] W. W. Chow, H. C. Schneider, S. W. Koch, C.-H. Chang, L. Chrostowski, and C. J. Chang-Hasnain. Nonequilibrium model for semiconductor laser modulation response. *IEEE Journal of Quantum Electronics*, 38(4):402–409, 2002.

[19] R. Binder, D. Scott, A. E. Paul, Lindberg M., Henneberger K., and S. W. Koch. Carrier-carrier scattering and optical dephasing in highly excited semiconductors. *Physical Review B*, 45(3):1107–1115, 1992.

[20] W. W. Chow and S. W. Koch. *Semiconductor-Laser Fundamentals, Physics of the Gain Materials.* Springer, Berlin, 1999.

[21] G. A. Baraff and R. K. Smith. Nonadiabatic semiconductor laser rate equations for the large-signal, rapid-modulation regime. *Physical Review A*, 61(4), 2000.

[22] C. H. Henry and R. F. Kazarinov. Quantum noise in photonics. *Reviews of Modern Physics*, 68(3):801–853, July 1996.

[23] B. Witzigmann. *Design and Implementation of a Three-Dimensional Edge Emitting Quantum Well Laser Simulator.* Ph.D. dissertation, Eidgenössische Technische Hochschule Zürich, Zurich, Switzerland, 2000.

[24] B. Klein, L. F. Register, M. Grupen, and K. Hess. Numerical simulation of vertical cavity surface emitting lasers. *OSA Optics Express*, 2(4):163–168, February 1998.

[25] Y. Liu, W.-C. Ng, F. Oyafuso, B. Klein, and K. Hess. Simulating the modulation response of VCSELs the effects of diffusion capacitance and spatial hole-burning. *IEE Proceedings Optoelectronics*, 149(4):182–188, August 2002.

[26] S. L. Chuang. *Physics of Optoelectronic Devices.* John Wiley & Sons, Inc., New York, 1995.

[27] O. Hess and T. Kuhn. Spatio-temporal dynamics of semiconductor lasers: Theory, modeling, and analysis. *Progress in Quantum Electronics*, 20(2):85–179, 1996.

[28] M. Luisier. Numerische Berechnung der optischen Verstärkung für verschiedene Halbleiter. Term project, Institut für Integrierte Systeme, ETH Zürich, Juni 2002.

[29] M. Pfeiffer. *Industrial-Strength Optoelectronics Device Simulation.* Ph.D. dissertation, Eidgenössische Technische Hochschule Zürich, Zurich, Switzerland, 2004.

[30] M. Luisier and S. Odermatt. Many-body effects in semiconductor lasers and carrier transport in quantum structures. Diploma project, Institut für Integrierte Systeme, ETH Zürich, March 2003.

[31] B. Witzigmann, A. Witzig, and W. Fichtner. Nonlinear gain saturation for 2-dimensional laser simulation. In *Proceedings of LEOS*, volume 2, pages 659–660, 1999.

[32] R. Loudon. *The Quantum Theory of Light.* Oxford University Press, New York, third edition, 2000.

[33] C. Wilmsen, H. Temkin, and L. A. Coldren, editors. *Vertical-Cavity Surface-Emitting Lasers.* Cambridge University Press, Cambridge, 1999.

[34] P. Royo. *Light Extraction from Microcavity Light Emitting Diodes: Optimization and Characterization of High-Brightness AlGaInP-Based Devices.* Ph.D. dissertation, Ecole Polytechnique Fédérale Lausanne, Lausanne, Switzerland, 2000.

[35] P. Bienstman, R. Baets, J. Vukusic, A. Larsson, M. J. Noble, M. Brunner, K. Gulden, P. Debernardi, L. Fratta, G. P. Bava, H. Wenzel, B. Klein, O. Conradi, R. Pregla, S. A. Riyopoulos, J. F. P. Seurin, and S. L. Chuang. Comparison of optical VCSEL models on the simulation of oxide-confined devices. *IEEE Journal of Quantum Electronics*, 37(12):1618–1631, December 2001.

[36] W. C. Chew. *Waves and Fields in Inhomogeneous Media.* IEEE Press, Piscataway, United States, first. edition, 1995.

[37] T. G. Moore, J. G. Blaschak, A. Taflove, and G. A. Kriegsmann. Theory and application of radiation boundary operators. *IEEE Transactions on Antennas and Propagation*, 36(12):1797–1812, 1988.

[38] J. Jin. *The Finite Element Method in Electromagnetics.* John Wiley & Sons, Inc., New York, second edition, 2002.

[39] M. Gastine, L. Courtois, and J. L. Dormann. Electromagnetic resonances of free dielectric spheres. *IEEE Transactions on Microwave Theory and Techniques*, MTT-15(12):694–700, 1967.

[40] P. Debye. Der Lichtdruck auf Kugeln von beliebigem Material. *Annalen der Physik*, 30(4):57–136, 1909.

[41] J.-P. Berenger. A perfectly matched layer for the absorption of electromagnetic waves. *Journal of Computational Physics*, 114(2):185–200, 1995.

[42] W. C. Chew and W. H. Weedon. A 3D perfectly matched medium from modified Maxwell's equations with stretched coordinates. *Microwave and Optical Technology Letters*, 7(13):599–604, 1994.

[43] F. L. Teixeira. *Novel Concepts for Differential Equation Based Electromagnetic Field Simulations.* Ph.D. dissertation, University of Illinois at Urbana-Champaign, Urbana, United States, 1999.

[44] J. D. Jackson. *Classical Electrodynamics.* John Wiley & Sons, Inc., New York, second. edition, 1975.

[45] M. J. Adams. *An Introduction to Optical Waveguides.* John Wiley & Sons, Inc., New York, 1981.

[46] M. Brunner. *Design and Characterization of Single and Dual Cavity Oxide Apertured VCSELs.* Ph.D. dissertation, Ecole Polytechnique Fédérale Lausanne, Lausanne, Switzerland, 2000.

[47] A. K. Jansen van Doorn, M. P. van Exter, and J. P. Woerdman. Elasto-optic anisotropy and polarization orientation of vertical-cavity surface-emitting semiconductor lasers. *Applied Physics Letters*, 69(8):1041–1043, 1996.

[48] K. Kells. *General Electrothermal Semiconductor Device Simulation.* Ph.D. dissertation, Eidgenössische Technische Hochschule Zürich, Zurich, Switzerland, 1994.

[49] ISE Integrated Systems Engineering AG, Zurich, Switzerland. *ISE TCAD 9.0 Manuals*, 1995-2003.

[50] G. K. Wachutka. Rigorous thermodynamic treatment of heat generation and conduction in semiconductor device modeling. *IEEE Transactions on Computer-Aided Design*, 9(11):1141–1149, 1990.

[51] S. Selberherr. *Analysis and Simulation of Semiconductor Devices.* Springer, Vienna, 1984.

[52] N. A. Gun'ko, A. S. Polkovnikov, and G. G. Zegrya. A numerical calculation of auger recombination coefficients for InGaAsP/InP quantum well heterostructures. *Semiconductors*, 34(4):462–466, 2000.

[53] D. Schroeder. *Modelling of Interface Carrier Transport for Device Simulation.* Springer, Vienna, 1994.

[54] G. A. Baraff. Semiclassical description of electron transport in semiconductor quantum-well devices. *Physical Review B*, 55(16), 1997.

[55] M. S. Hybertsen, M. A. Alam, G. E Shtengel, G. L. Belenky, C. L. Reynolds, D. V. Donetsky, R. K. Smith, R. F. Baraff, R. F. Kazarinov, J. D. Wynn, and L. E. Smith. Role of p-doping profile in InGaAsP multi-quantum well lasers: Comparison of simulation and experiment. In *Proceedings SPIE*, volume 3625, pages 524–534, 1999.

[56] A. Witzig. *Modeling the Optical Processes in Semiconductor Lasers.* Ph.D. dissertation, Eidgenössische Technische Hochschule Zürich, Zurich, Switzerland, 2002.

[57] J. K. Ousterhout. *Tcl and the Tk Toolkit.* Addison-Wesley Publishing Company, Reading, United States, 1994.

[58] L. E. Thode, G. Csanak, L. L. So, T. J. Kwan, and M. M. Campbell. Time-dependent numerical simulation of vertical cavity lasers. In *Proceedings SPIE*, volume 2146, pages 174–184, 1994.

[59] J.-P. Zhang and K. Petermann. Numerical analysis of transverse mode in gain-guided vertical cavity surface emitting lasers. *IEE Proceedings in Optoelectronics*, 142(1):29–35, February 1995.

[60] B. Demeulenaere, D. De Zutter, and R. Baets. Rigorous electromagnetic study of diffraction loss in VCSEL mirrors. *IEE Proceedings in Optoelectronics*, 143(4):221–227, August 1996.

[61] D. Burak and R. Binder. Cold-cavity vectorial eigenmodes of VCSELs. *IEEE Journal of Quantum Electronics*, 33(7):1205–1215, July 1997.

[62] H. Wenzel and H.-J. Wünsche. The effective frequency method in the analysis of vertical-cavity surface-emitting lasers. *IEEE Journal of Quantum Electronics*, 33(7):1205–1215, July 1997.

[63] J. F. P. Seurin and S. L. Chuang. Discrete Bessel transform and beam propagation method for modeling of vertical cavity surface-emitting lasers. *Journal of Applied Physics*, 82(5):2007–2016, September 1997.

[64] G. R. Hadley. Low-truncation-error finite difference equations for photonics simulation II: Vertical-cavity surface-emitting lasers. *IEEE Journal of Lightwave Technology*, 16(1):142–151, January 1998.

[65] N. Mahmood, B. M. A. Rahman, and K. T. V. Grattan. Accurate three-dimensional modal solutions for optical resonators with periodic layered structure by using the finite element method. *Journal of Lightwave Technology*, 16(1):156–161, January 1998.

[66] J. F. P. Seurin, G. Liu, D. C. Barnes, D. I. Babic, S. W. Corzine, and M. R. T. Tan. A finite-difference time-domain electromagnetic field solver for vertical-cavity lasers. *Microwave and Optical Technology Letters*, 18(6):385–387, January 1998.

[67] M. J. Noble, J. A. Lott, and J. P. Loehr. Quasi-exact optical analysis of oxide-apertured microcavity VCSEL's using vector finite elements. *IEEE Journal of Quantum Electronics*, 34(12):2327–2339, December 1998.

[68] M. J. Noble, J. P. Loehr, and J. A. Lott. Analysis of microcavity VCSEL lasing modes using a full-vector weighted index method. *IEEE Journal of Quantum Electronics*, 34(10):1890–1903, October 1998.

[69] P. Bienstman, H. Derudder, R. Baets, F. Olyslager, and D. De Zutter. Analysis of cylindrical waveguide discontinuities using vectorial

eigenmodes and perfectly matched layers. *IEEE Transactions on Microwave Theory and Techniques*, 49(2):349–354, February 2001.

[70] O. Conradi, S. Helfert, and R. Pregla. Comprehensive modeling of vertical-cavity laser-diodes by the method of lines. *IEEE Journal of Quantum Electronics*, 37(7):928–935, July 2001.

[71] S. Riyopoulos, D. Dialetis, J. Inman, and A. Phillips. Active-cavity vertical-cavity surface-emitting laser eigenmodes with simple analytic representation. *Journal of the Optical Society of America B*, 18(9):1268–1284, September 2001.

[72] A. Christ, N. Kuster, M. Streiff, A. Witzig, and W. Fichtner. Correction of the numerical reflection coefficient of the finite-difference time-domain method for efficient simulation of vertical-cavity surface-emitting lasers. *JOSA B*, 20(7):1401–1408, 2003.

[73] D. R. Fokkema, G. L. Sleijpen, and H. A. van der Vorst. Jacobi-Davidson style QR and QZ algorithms for the reduction of matrix pencils. *SIAM Journal of Scientific Computing*, 20(1):94–125, 1998.

[74] P. Arbenz and R. Geus. A comparison of solvers for large eigenvalue problems occuring in the design of resonant cavities. *Numerical Linear Algebra With Applications*, 6(1):3–16, February 1999.

[75] Z. S. Sacks, D. M. Kingsland, R. Lee, and J.-F. Lee. A perfectly matched anisotropic absorber for use as an absorbing boundary condition. *IEEE Transactions on Antennas and Propagation*, 43(12):1460–1463, 1995.

[76] S. Adachi. *Optical Constants of Crystalline and Amorphous Semiconductors: Numerical Data and Graphical Information.* Kluwer, Boston, 1999.

[77] S. Adachi. *Optical Properties of Crystalline and Amorphous Semiconductors: Materials and Fundamental Principles.* Kluwer, Boston, 1999.

[78] J.-F. Lee, G. M. Wilkins, and R. Mittra. Finite-element analysis of axisymmetric cavity resonator using a hybrid edge element technique. *IEEE Transactions on Microwave Theory and Techniques*, 41(11):1981–1987, 1993.

[79] A. D. Greenwood and J.-M. Jin. A novel efficient algorithm for scattering from a complex BOR using mixed finite elements and cylindrical PML. *IEEE Transactions on Antennas and Propagation*, 47(4):620–629, April 1999.

[80] P. Lacoste. Solution of Maxwell equation in axisymmetric geometry by fourier series decomposition and by use of $h\,(\mathrm{rot})$ conforming finite element. *Numerische Mathematik*, 84:577–609, 2000.

[81] R. Hiptmair and P. D. Ledger. Computation of resonant modes for axisymmetric cavities using hp-version finite elements. Technical report, ETH Zurich, 2003.

[82] J. C. Nédélec. A new family of mixed elements in R^3. *Numerische Mathematik*, 50:57–81, 1986.

[83] H. Whitney. *Geometric Integration Theory.* Princeton University Press, Princeton, 1957.

[84] O. Chinellato, P. Arbenz, M. Streiff, and A. Witzig. Computation of optical modes inside axisymmetric open cavity resonators. *paper accepted for publication in Future Generation Computing Systems.*

[85] M. Ainsworth and J. Coyle. Hierarchic hp-edge element families for maxwell's equations on hybrid quadrilateral / triangular meshes. *Computer Methods in Applied Mechanics and Engineering*, 190:6709–6733, 2001.

[86] R. D. Graglia, D. R. Wilton, and A. F. Peterson. Higher order interpolatory vector bases for computational electromagnetics. *IEEE Transactions on Antennas and Propagation*, 45(3):329–342, 1997.

[87] D. Sun, J. Manges, X. Yuan, and Z. Cendes. Spurious modes in finite-element methods. *IEEE Antennas and Propagation Magazine*, 37(5):12–24, 1995.

[88] Z. J. Cendes and S. H. Wong. C^1 quadratic interpolation over arbitrary point sets. *IEEE Computer Graphics and Applications*, 7(11):8–16, 1987.

[89] R. E. Bank, D. J. Rose, and W. Fichtner. Numerical methods for semiconductor device simulation. *IEEE Transactions on Electron Devices*, ED-30(9):1031–1041, 1983.

[90] W. Fichtner, R. E. Bank, and D. J. Rose. Semiconductor device simulation. *IEEE Transactions on Electron Devices*, ED-30(9):1018–1030, 1983.

[91] D. L. Scharfetter and H. K. Gummel. Large-signal analysis of a silicon Read diode oscillator. *IEEE Transactions on Electron Devices*, ED-16:64–77, 1969.

[92] T.-W. Tang. Extension of the Scharfetter-Gummel algorithm to the energy-balance equation. *IEEE Transactions on Electron Devices*, ED-31(12):1912–1914, 1984.

[93] A. de Mari. An accurate numerical one-dimensional solution of the pn-junction under arbitrary transient conditions. *Solid State Electronics*, 11:1021–1053, 1968.

[94] F. Bonani, G. Ghione, M. R. Pinto, and R. K. Smith. An efficient approach to noise analysis through multidimensional physics-based models. *IEEE Transactions on Electron Devices*, 45(1):261–269, 1998.

[95] B. Schmithüsen, A. Schenk, and W. Fichtner. Simulation of noise in semiconductor devices with DESSIS using the direct impedance field method. Technical report, ETH Zurich, 2000.

[96] R. E. Bank, W. M. Coughran Jr., W. Fichtner, E. H. Grosse, D. J. Rose, and R. K. Smith. Transient simulation of silicon devices and circuits. *IEEE Transactions on Computer-Aided Design*, CAD-4(4):436–449, 1983.

[97] R. E. Bank and D. J. Rose. Global approximate Newton Methods. *Numerische Mathematik*, 37:279–295, 1981.

[98] O. Schenk. *Scalable Parallel Sparse LU Factorization Methods on Shared Memory Multiprocessors.* Ph.D. dissertation, Eidgenössische Technische Hochschule Zürich, Zurich, Switzerland, 2000.

[99] H. K. Gummel. A self-consistent iterative scheme for one-dimensional steady state transistor calculations. *IEEE Transactions on Electron Devices*, ED-11:455–465, 1964.

[100] M. T. Heath. *Scientific Computing: An Introductory Survey.* The McGraw-Hill Companies, Inc., New York, 1997.

[101] G. H. Golub and C. F. Van Loan. *Matrix Computations.* The John Hopkins University Press, Baltimore and London, third edition, 1996.

[102] M. Streiff, A. Witzig, and W. Fichtner. Computing optical modes for VCSEL device simulation. *IEE Proceedings Optoelectronics*, 149(4):166–173, 2002.

[103] M. Streiff, A. Witzig, M. Pfeiffer, P. Royo, and W. Fichtner. A comprehensive VCSEL device simulator. *IEEE Journal of Selected Topics in Quantum Electronics*, 9(3):879–891, 2003.

[104] O. Chinellato. *in preparation.* Ph.D. dissertation, Eidgenössische Technische Hochschule Zürich, Zurich, Switzerland.

[105] G. R. Hadley. Effective index model for vertical-cavity surface-emitting lasers. *Optics Letters*, 20(13):1483–1485, July 1995.

[106] S. D. Brorson, H. Yokoyama, and E. P. Ippen. Spontaneous emission rate alteration in optical waveguide structures. *IEEE Journal of Quantum Electronics*, 26(5):1492–1499, 1990.

[107] S. Scheerlinck. Simulation of spontaneous emission in resonant cavity light-emitting diodes. Diploma project, Institut für Integrierte Systeme IIS, ETH Zürich, August 2003.

[108] M. Jungo, F. Monti di Sopra, D. Erni, and W. Bächtold. Scaling effects on vertical-cavity surface-emitting lasers static and dynamic behavior. *Journal of Applied Physics*, 91(9):5550–5557, 2002.

[109] F. Monti di Sopra. *Optical Properties of VCSELs and Phase-Coupled Arrays*. Ph.D. dissertation, Ecole Polytechnique Fédérale Lausanne, Lausanne, Switzerland, 2002.

[110] S. Gehrsitz, F. K. Reinhart, C. Gourgon, N. Herres, A. Vonlanthen, and H. Sigg. The refractive index of $Al_xGa_{1-x}As$ below the band gap: Accurate determination and empirical modeling. *Journal of Applied Physics*, 87(11):7825–7837, June 2000.

[111] S. Adachi, editor. *Properties of Aluminium Gallium Arsenide*. INSPEC, London, 1993.

[112] R. A. Morgan, G. D. Guth, M. W. Focht, M. T. Asom, K. Kojima, L. E. Rogers, and S. E. Callis. Transverse mode control of vertical-cavity top-surface-emitting lasers. *IEEE Photonics Technology Letters*, 4(4):374–376, 1993.

[113] N. Ueki, A. Sakamoto, T. Nakamura, H. Nakayama, J. Sakurai, H. Otoma, Y. Miyamoto, M. Yoshikawa, and M. Fuse. Single-transverse-mode 3.4 *mw* emission of oxide-confined 780 *nm* VCSEL. *IEEE Photonics Technology Letters*, 11(12):1539–1541, December 1999.

[114] H. Martinsson, J. A. Vukusic, and A. Larsson. Single-mode power dependence on surface relief size for mode-stabilized oxide-confined vertical-cavity surface-emitting lasers. *IEEE Photonics Technology Letters*, 12(9):1129–1131, 2000.

[115] H. J. Unold, S. W. Z. Mahmoud, M. Grabherr, R. Michalzik, and K. J. Ebeling. Large-area single-mode VCSELs and the self-aligned surface relief. *IEEE Journal on Selected Topics in Quantum Electronics*, 7(2):386–392, March/April 2001.

[116] P. Bhattacharya, editor. *Properties of Lattice-Matched and Strained Indium Gallium Arsenide*. INSPEC, London, 1993.

[117] M. Levinshtein, S. Rumyantsev, and M. Shur, editors. *Handbook Series on Semiconductor Parameters*, volume 2. World Scientific, Singapore, 1999.

[118] F. L. Teixeira and W. C. Chew. Systematic derivation of anisotropic PML absorbing media in cylindrical and spherical coordinates. *IEEE Microwave and Guided Wave Letters*, 7(11):371–373, 1997.

Curriculum Vitae

Matthias Streiff was born in London in 1971. He received the Dipl. Ing. degree in Electrical Engineering from the Swiss Federal Institute of Technology (ETH), Zurich in 1997 and the M. Sc. degree in Semiconductor Science and Technology from Imperial College London (ICL) in 1998. The stay at ICL was funded by an ETH-ICL exchange scholarship which was awarded to him in 1997. He worked in 1995 at CSEM SA, Neuchâtel (Switzerland) on digital ASIC design and in 1997 at ABB Semiconductor AG, Lenzburg (Switzerland) on the design of high power semiconductor devices. From 1998 to 1999 he was employed as an integrated circuit design engineer at Sony Semiconductor and Devices Europe Ltd., Basingstoke (United Kingdom) in the wireless business department. Since 2000 he has been with the Integrated Systems Laboratory in the department of Information Technology and Electrical Engineering at ETH Zurich. His current research interests relate to numerical modeling, design, and characterisation of optoelectronic devices for applications in telecommunications and biotechnology.